This Page Is Inserted by IFW Operations
and is not a part of the Official Record

BEST AVAILABLE IMAGES

Defective images within this document are accurate representations of the original documents submitted by the applicant.

Defects in the images may include (but are not limited to):

- BLACK BORDERS

- TEXT CUT OFF AT TOP, BOTTOM OR SIDES

- FADED TEXT

- ILLEGIBLE TEXT

- SKEWED/SLANTED IMAGES

- COLORED PHOTOS

- BLACK OR VERY BLACK AND WHITE DARK PHOTOS

- GRAY SCALE DOCUMENTS

IMAGES ARE BEST AVAILABLE COPY.

As rescanning documents *will not* correct images, please do not report the images to the Image Problem Mailbox.

TECHNICAL NOTES

Optimal short scan convolution reconstruction for fanbeam CT

Dennis L. Parker

Department of Radiation Oncology, University of California at San Francisco, San Francisco, California 94143

The problem of using a divergent fan beam convolution reconstruction algorithm in conjunction with a minimal complete (180° plus the fan angle) data set is reviewed. It is shown that by proper weighting of the initial data set, image quality essentially equivalent to the quality of reconstructions from 360° data sets is obtained. The constraints on the weights are that the sum of the two weights corresponding to the same line-integral must equal one, in regions of no data the weights must equal zero, and the weights themselves as well as the gradient of the weights must be continuous over the full 360°. After weighting the initial data with weights that satisfy these constraints, image reconstruction can be conveniently achieved by using the standard (hardwired if available) convolver and backprojector of the specific scanner.

I. INTRODUCTION

In the development of fast, special purpose CT scanners, a reduction in scanning time is also obtained by collecting only
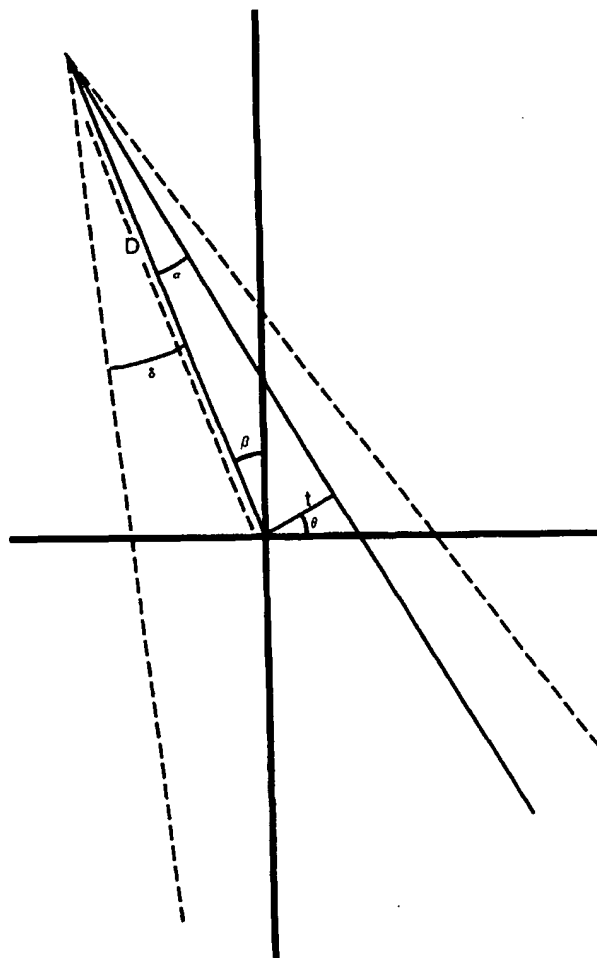

FIG. 1. Scanning geometry utilized in conventional fanbeam scanners.

the minimum number of projections (views) required for image reconstruction. It is known, for example, that a scanner with a parallel beam geometry (such as a translate/rotate scanner) requires projections for 180°.[1] It has also been shown that data collected from fanbeam geometries can be rebinned or reorganized into parallel ray data sets for reconstruction with parallel geometry algorithms.[2] It is easy to show that a complete parallel ray equivalent data set can be obtained from a set of divergent ray projections taken over 180° plus the angle of the divergent fan beam. It is logical to refer to this set of divergent projections which covers 180° plus the fan angle as the "minimal complete data set". It is the minimum set of equally spaced projection measurements which can be used in conventional convolution type reconstruction algorithms. In this note we show that with proper weighting of the input data set it is possible to reconstruct the minimal complete data set using conventional divergent convolution reconstruction algorithms (i.e., with no rebinning into parallel ray data sets). It is therefore possible to utilize conventional array processors and standard hardwired backprojectors in performing the reconstruction of data from short scans.

In a paper by Naparstek,[3] several methods of short scan fan beam reconstruction techniques were derived and assessed. However, those algorithms which generated images of reasonable quality also required more projections than a minimal complete set. The more successful algorithms utilized a smooth weighting of the extra projections in a manner similar to that used in standard CT overscanning for artifact reduction.[4] In this note, we show that by a simple modification of one of the techniques of Naparstek, good quality images can be generated from a minimal complete short scan data set.

II. ALGORITHM DEVELOPMENT

Figure 1 illustrates the geometry of fan beam data collection where β is the angle of rotation of the source to axis
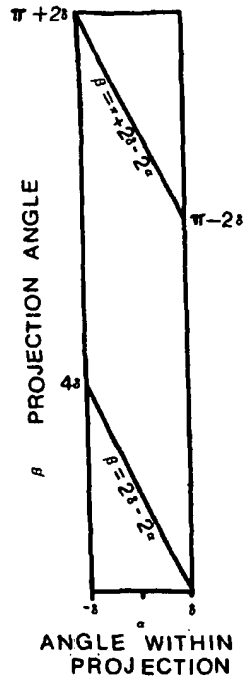
EXHIBIT

A

tabbies

FIG. 2. Outline of sampling region as a function of α (the horizontal coordinate) and β (the vertical coordinate). The upper triangle is geometrically the same (i.e., it samples the same set of line integrals) as the lower triangle.

segment and α is the relative angular position of an individual line integral from the source to a detector element. If $g(\alpha,\beta)$ is the projection measurement (line integral) along the segment specified by (α,β) and if $p(t,\vartheta)$ is the corresponding parallel ray projection measurement where (t,ϑ) are defined in the figure, it is evident that

$$p(t,\vartheta) = g(\alpha,\beta), \tag{1}$$

when

$$\vartheta = \beta + \alpha$$

and

$$t = D \sin \alpha.$$

The symmetry over rotation requires that

$$p(t,\vartheta) = p(-t,\vartheta + \pi), \tag{2}$$

which is equivalent to

$$g(\alpha,\beta) = g(-\alpha, \pi + \beta + 2\alpha). \tag{3}$$

Thus, if data is collected in the rectangle,

$$-\delta < \alpha < \delta,$$

$$0 < \beta < \pi + 2\delta, \tag{4}$$

where 2δ is the fan angle defined in Fig. 1, then the data in the triangle,

$$0 < \beta < 2\delta - 2\alpha,$$

will be positionally redundant with the data in the region:

$$\pi - 2\alpha < \beta < \pi + 2\delta.$$

This is illustrated in Fig. 2. The set of line integrals specified by the upper triangle is resampled in the lower triangle as required by Eq. (3). In contrast, the set of line integrals specified by the parallelogram region bounded by the two triangles is only sampled once.

Because only part of the region in the (α,β) diagram is doubly scanned, it is expected that direct application of any direct divergent fanbeam reconstruction algorithm which itself is based on total double scanning (360°) would yield a distorted image. That this is true is illustrated using the simulated data of Fig. 3. The mathematical phantom of Fig. 3(a) yields the divergent sinogram of Fig. 3(b) for a third generation (rotate–rotate) scanner with 121 detectors at 1/3-degree angular increments for a fan angle of 40° and 360 views taken at one-degree projection increments. The data has been convolved with a simple divergent algorithm kernel[5]:

$$q_i = \frac{-1}{\pi^2 \sin^2(i\Delta\alpha)}, i,\text{odd} ,$$

$$q_i = 0, i,\text{even } i \neq 0 ,$$

$$q_0 = \frac{1}{4\Delta\alpha^2}. i = 0 \tag{5}$$

When the entire (360°) data set is reconstructed using a standard backprojection algorithm, the image of Fig. 3(c) is obtained. If, however, the case of a minimal complete data set is imitated by considering only the first 220 projections in the standard backprojection algorithm, the image of Fig. 3(d) is obtained. The variation in intensity over the image is surprisingly smooth and the image itself is very recognizable.

It might be expected that the smooth variation could be removed by setting the data from one of the redundant triangles to zero. It was shown by Naparstek[3] that the streak artifacts which resulted from the zeroed boundary of the triangle were sufficient to completely mask the image. Of the other algorithms proposed by Naparstek, the most successful ones required additional data (beyond the minimal complete short scan data set). This additional data was then used to feather smoothly to zero the abrupt discontinuity at the parallelogram boundary. In addition to requiring data beyond that of a minimal complete data set, the algorithms also generally required a more complicated convolution kernel.

The logical extension, which was not formally proposed or attempted by Naparstek, is to weight the data of the minimal complete data set in such a manner that the discontinuity is as uniformly distributed as possible. The constraints on the set of weights can be developed as follows: The weighted data set is defined as $g'(\alpha,\beta)$ and is given by

$$g'(\alpha,\beta) = \omega(\alpha,\beta)g(\alpha,\beta), \tag{6}$$

where

$$\omega(\alpha,\beta) + \omega(-\alpha,\pi + \beta + 2\alpha) = 1. \tag{7}$$

The minimization of the discontinuities at the various borders of the triangles is accomplished by the requirements

$$\omega(\alpha,0) = \omega(\alpha,\pi + 2\delta) = 0, \tag{8}$$

$$\omega(\alpha,2\delta - 2\alpha) = \omega(\alpha,\pi - 2\alpha) = 1, \tag{9}$$

$$\left.\frac{\partial\omega(\alpha,\beta)}{\partial\beta}\right|_{\beta = 2\delta - 2\alpha} = \left.\frac{\partial\omega(\alpha,\beta)}{\partial\beta}\right|_{\beta = \pi - 2\alpha} = 0, \tag{10}$$

$$\left.\frac{\partial\omega(\alpha,\beta)}{\partial\alpha}\right|_{\beta = 2\delta - 2\alpha} = \left.\frac{\partial\omega(\alpha,\beta)}{\partial\alpha}\right|_{\beta = \pi - 2\alpha} = 0. \tag{11}$$

One set of weights which satisfies all of the above constraints is given by
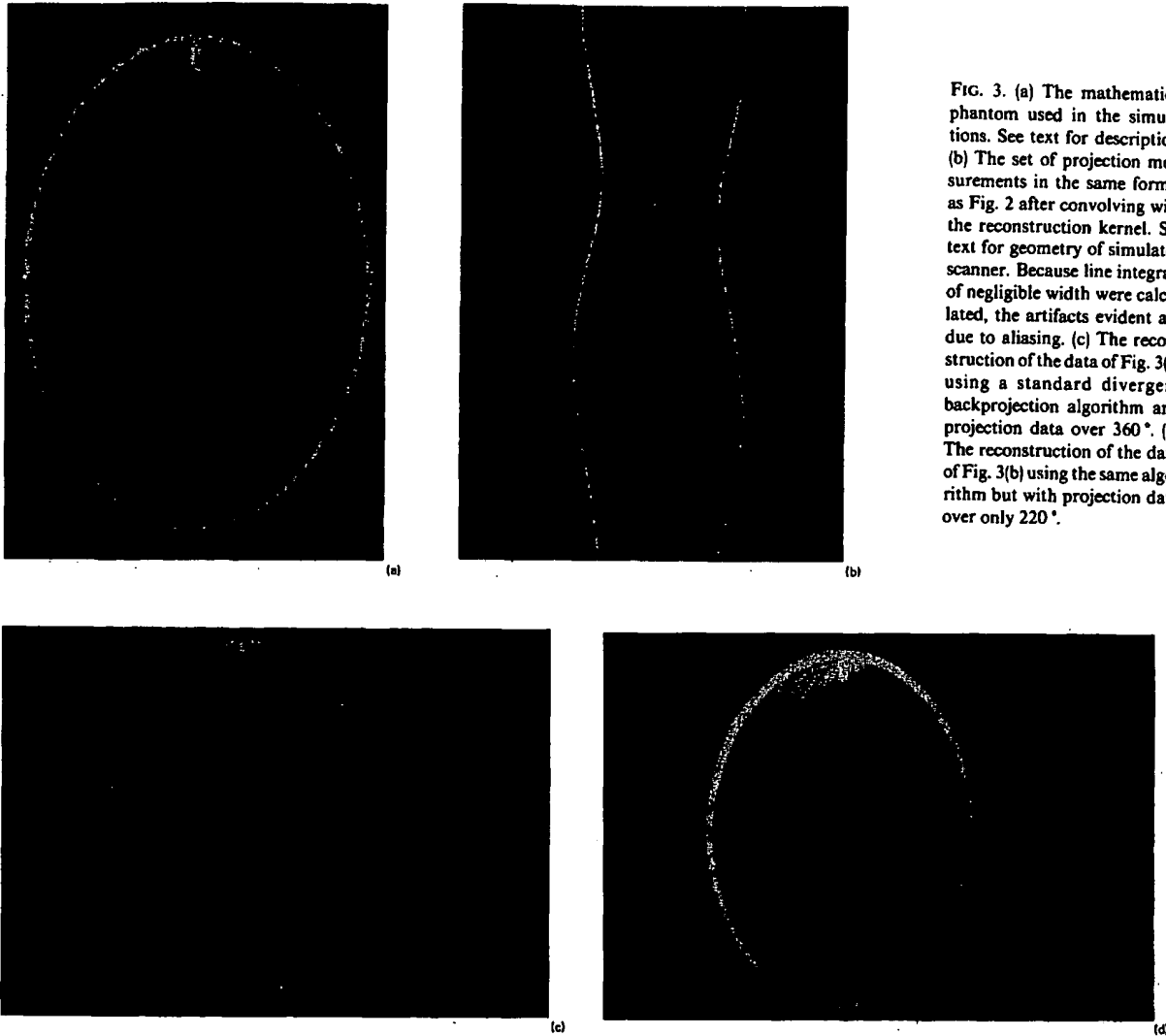
FIG. 3. (a) The mathematical phantom used in the simulations. See text for description. (b) The set of projection measurements in the same format as Fig. 2 after convolving with the reconstruction kernel. See text for geometry of simulated scanner. Because line integrals of negligible width were calculated, the artifacts evident are due to aliasing. (c) The reconstruction of the data of Fig. 3(b) using a standard divergent backprojection algorithm and projection data over 360°. (d) The reconstruction of the data of Fig. 3(b) using the same algorithm but with projection data over only 220°.

$$\omega(\alpha,\beta) = \sin^2\left(\frac{\pi}{4}\frac{\beta}{\delta-\alpha}\right), \quad 0<\beta<2\delta - 2\alpha \ ,$$

$$\omega(\alpha,\beta) = 1, \quad 2\delta - 2\alpha<\beta<\pi - 2\alpha \ ,$$

$$\omega(\alpha,\beta) = \sin^2\left(\frac{\pi}{4}\frac{\pi+2\delta-\beta}{\alpha}\right), \quad \pi - 2\alpha<\beta<\pi + 2\delta \ . \quad (12)$$

III. RESULTS

In Fig. 4(a) we show the sinogram from Fig. 3(b) weighted by the functions of Eq. (12). Figure 4(b) is the reconstruction of the data from 4(a) using a standard divergent fanbeam backprojection algorithm. [This is the same algorithm as used in Figs. 3(c) and (d).] It is evident in comparing Figs. 3(c) and 4(b) that there is no appreciable difference in image quality between the full 360° reconstruction and the 220°, weighted reconstruction.

IV. CONCLUSION

The technique which has been presented has demonstrated the ability to reconstruct images from a minimal complete data set (180° plus the fan angle) with no evident loss in image quality over that obtained from reconstruction of the full 360° scan data. The technique requires the smooth weighting of data in double-scanned regions while the weights and their derivatives are required to be continuous at the boundaries. After the weighting is performed, standard divergent convolution/backprojection algorithms are used to reconstruct the image. It is therefore possible to maintain the hardware-related reconstruction speed of standard convolvers and backprojectors while significantly reducing the required number of scanned projections, thereby decreasing the associated scan time. In this manner artifacts related to the duration of the scan, such as motion artifacts or electronic drifts in the data acquisition system, etc., can be minimized.
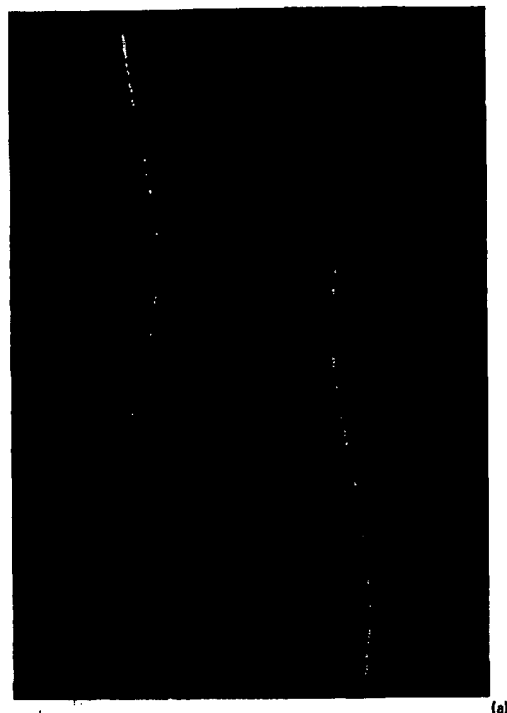
(a)
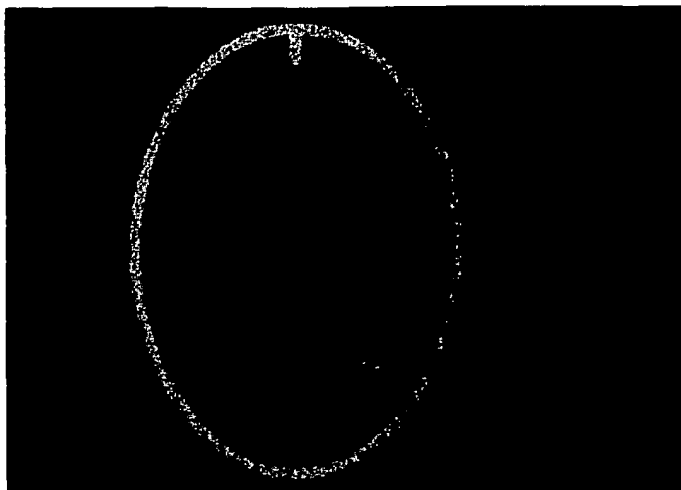
(b)

FIG. 4. (a) The projection data over 220° where the input data has been weighted by the weights given in the text and then convolved with the same algorithm as that of Fig. 3(b). (b) The reconstruction of the data of Fig. 4(a) using the same algorithm as Figs. 3(c) and (d).

ACKNOWLEDGMENTS

[1]L. A. Shepp and B. F. Logan, IEEE Trans. Nucl. Sci. NS-21, 21 (1974).
[2]P. Dreike and D. P. Boyd, Comput. Graph. Image Proc. 5, 459 (1976).
[3]A. Naparstek, IEEE Trans. Nucl. Sci. NS-27, 1112 (1980).
[4]D. L. Parker, V. Smith, and J. H. Stanley, Med. Phys. 8, 706 (1981).
[5]G. T. Herman, A. V. Lakshminarayanan, and A. Naparstek, Comput. Biol. Med. 6, 259 (1976).

3 Algorithms for Reconstruction with Nondiffracting Sources

In this chapter we will deal with the mathematical basis of tomography with nondiffracting sources. We will show how one can go about recovering the image of the cross section of an object from the projection data. In ideal situations, projections are a set of measurements of the integrated values of some parameter of the object—integrations being along straight lines through the object and being referred to as line integrals. We will show that the key to tomographic imaging is the Fourier Slice Theorem which relates the measured projection data to the two-dimensional Fourier transform of the object cross section.

This chapter will start with the definition of line integrals and how they are combined to form projections of an object. By finding the Fourier transform of a projection taken along parallel lines, we will then derive the Fourier Slice Theorem. The reconstruction algorithm used depends on the type of projection data measured; we will discuss algorithms based on parallel beam projection data and two types of fan beam data.
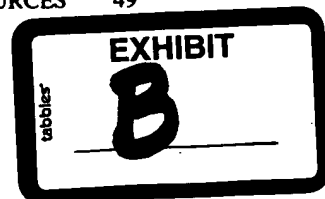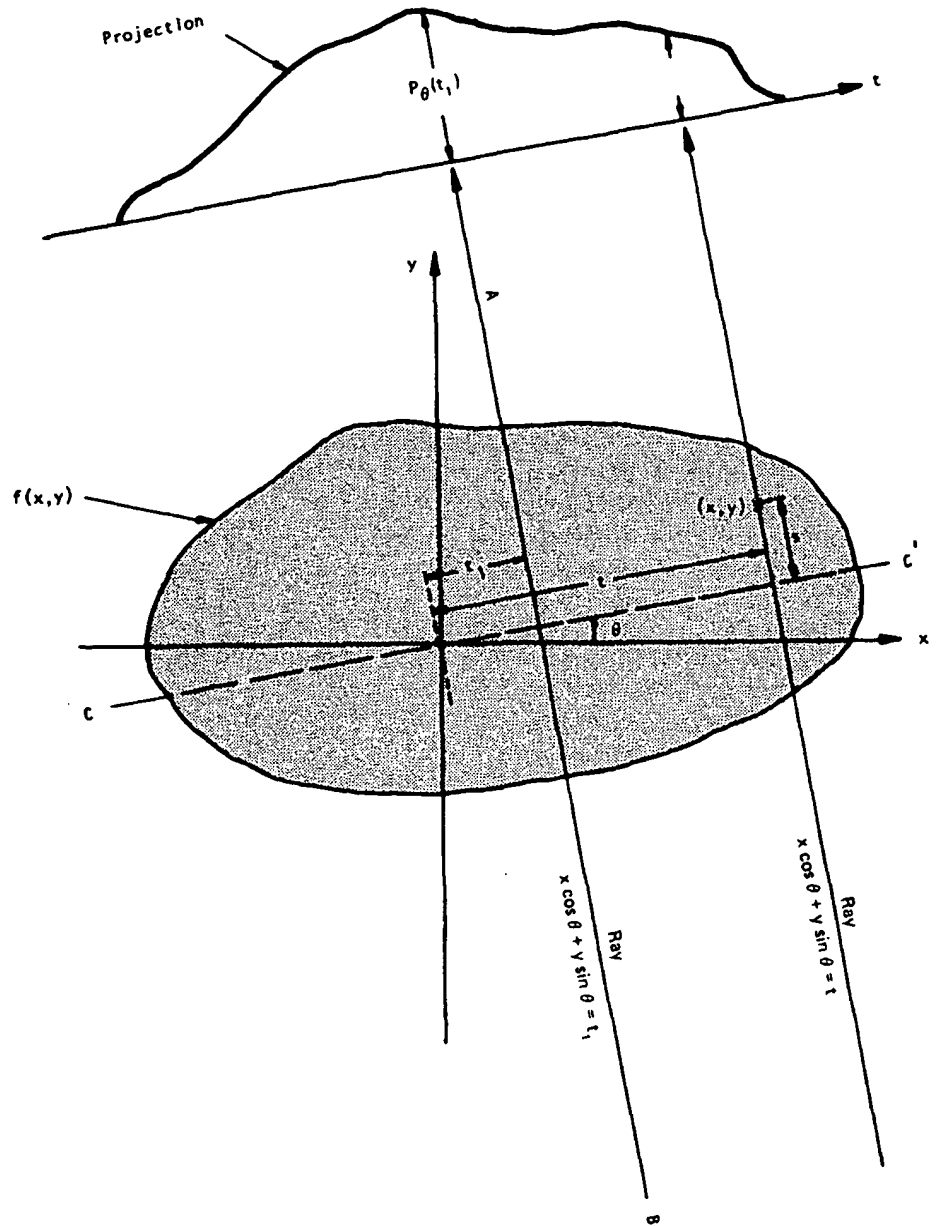
3.1 Line Integrals and Projections

A line integral, as the name implies, represents the integral of some parameter of the object along a line. In this chapter we will not concern ourselves with the physical phenomena that generate line integrals, but a typical example is the attenuation of x-rays as they propagate through biological tissue. In this case the object is modeled as a two-dimensional (or three-dimensional) distribution of the x-ray attenuation constant and a line integral represents the total attenuation suffered by a beam of x-rays as it travels in a straight line through the object. More details of this process and other examples will be presented in Chapter 4.

We will use the coordinate system defined in Fig. 3.1 to describe line integrals and projections. In this example the object is represented by a two-dimensional function $f(x, y)$ and each line integral by the (θ, t) parameters.

The equation of line AB in Fig. 3.1 is

$$x \cos \theta + y \sin \theta = t \tag{1}$$

EXHIBIT

B

Fig. 3.1: *An object, $f(x, y)$, and its projection, $P_\theta(t_1)$, are shown for an angle of θ. (From [Kak79].)*

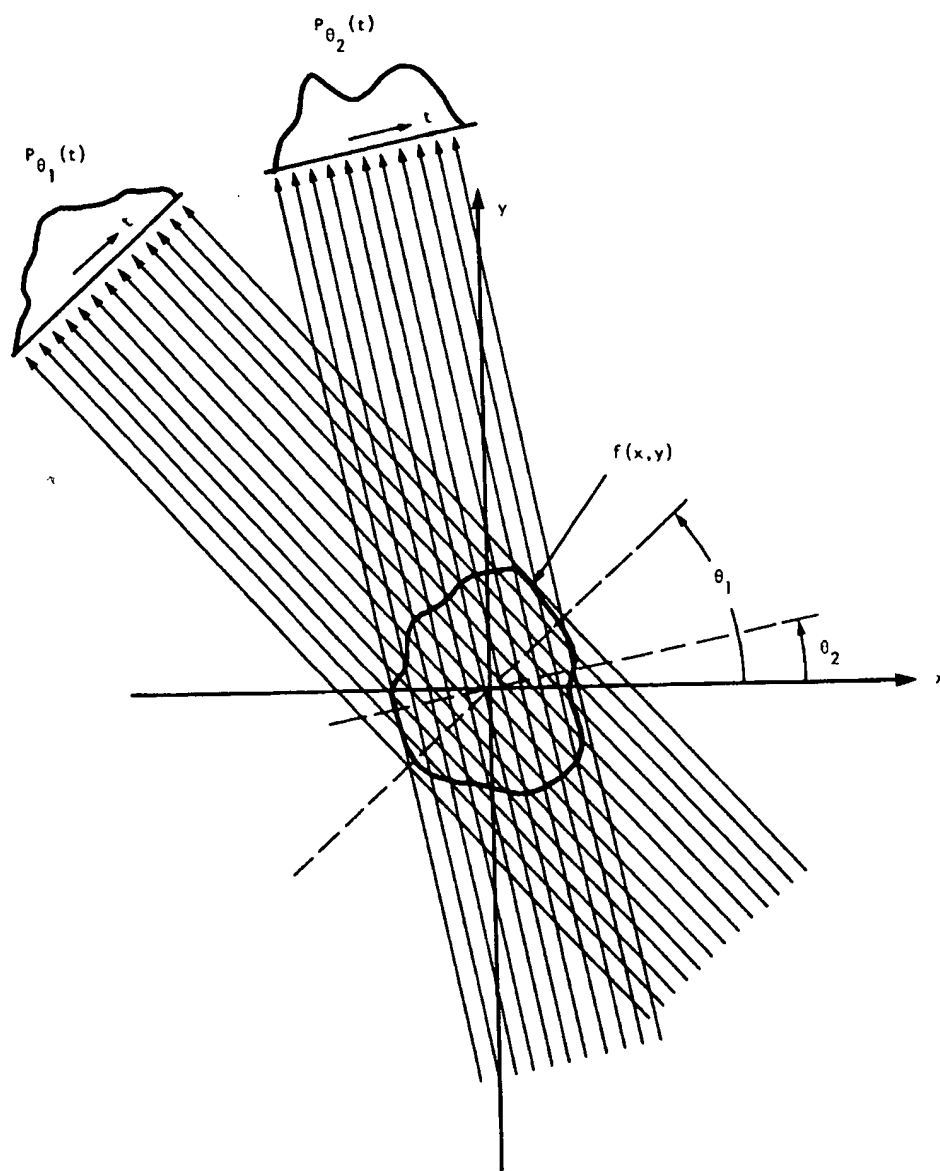and we will use this relationship to define line integral $P_\theta(t)$ as

$$P_\theta(t) = \int_{(\theta,t)\,\text{line}} f(x, y)\, ds. \tag{2}$$

Using a delta function, this can be rewritten as

$$P_\theta(t) = \int_{-\infty}^{\infty} \int_{-\infty}^{\infty} f(x, y)\delta(x \cos \theta + y \sin \theta - t)\, dx\, dy. \tag{3}$$

The function $P_\theta(t)$ is known as the Radon transform of the function $f(x, y)$.

Fig. 3.2: *Parallel projections are taken by measuring a set of parallel rays for a number of different angles. (From [Ros82].)*

A projection is formed by combining a set of line integrals. The simplest projection is a collection of parallel ray integrals as is given by $P_\theta(t)$ for a constant θ. This is known as a parallel projection and is shown in Fig. 3.2. It could be measured, for example, by moving an x-ray source and detector along parallel lines on opposite sides of an object.

Another type of projection is possible if a single source is placed in a fixed position relative to a line of detectors. This is shown in Fig. 3.3 and is known as a fan beam projection because the line integrals are measured along fans.

Most of the computer simulation results in this chapter will be shown for the image in Fig. 3.4. This is the well-known Shepp and Logan [She74]
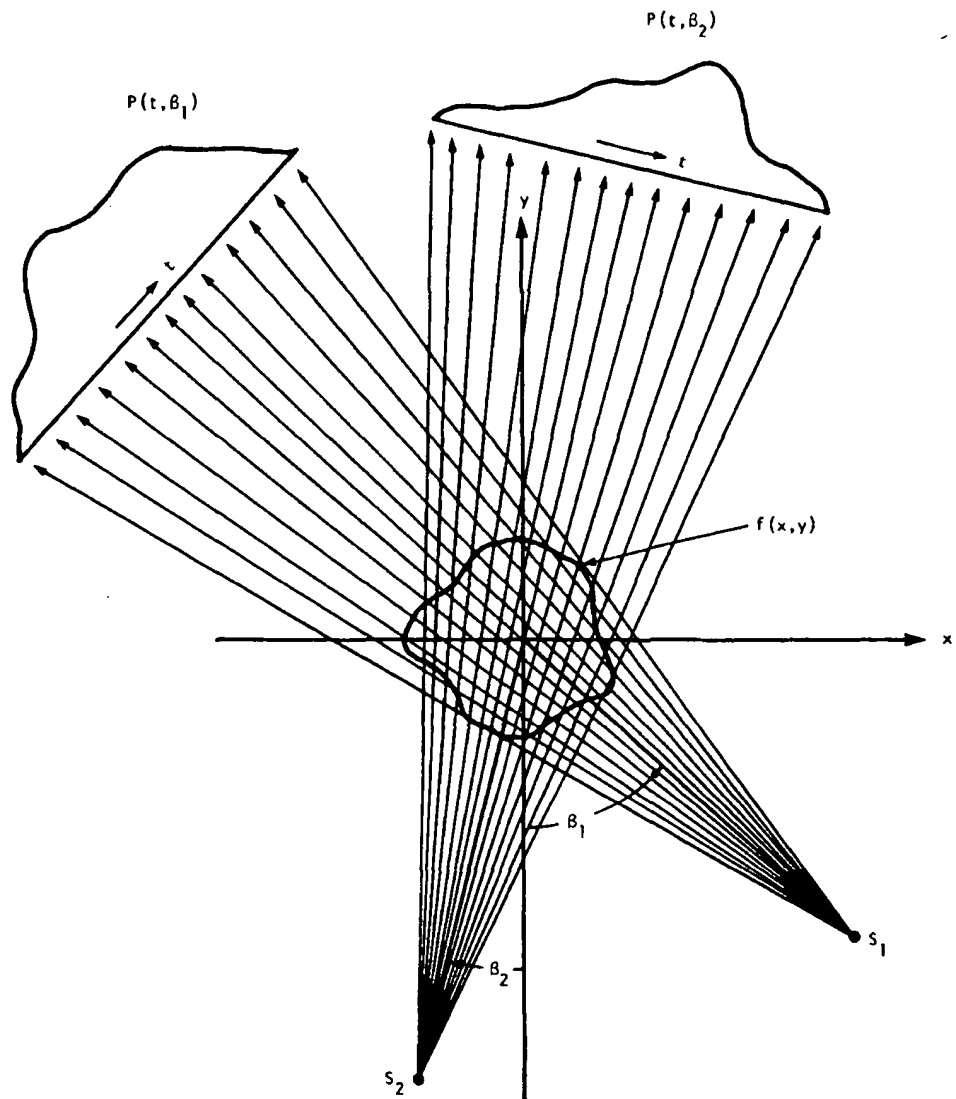
Fig. 3.3: *A fan beam projection is collected if all the rays meet in one location. (From [Ros82].)*

"head phantom," so called because of its use in testing the accuracy of reconstruction algorithms for their ability to reconstruct cross sections of the human head with x-ray tomography. (The human head is believed to place the greatest demands on the numerical accuracy and the freedom from artifacts of a reconstruction method.) The image in Fig. 3.4(a) is composed of 10 ellipses, as illustrated in Fig. 3.4(b). The parameters of these ellipses are given in Table 3.1.
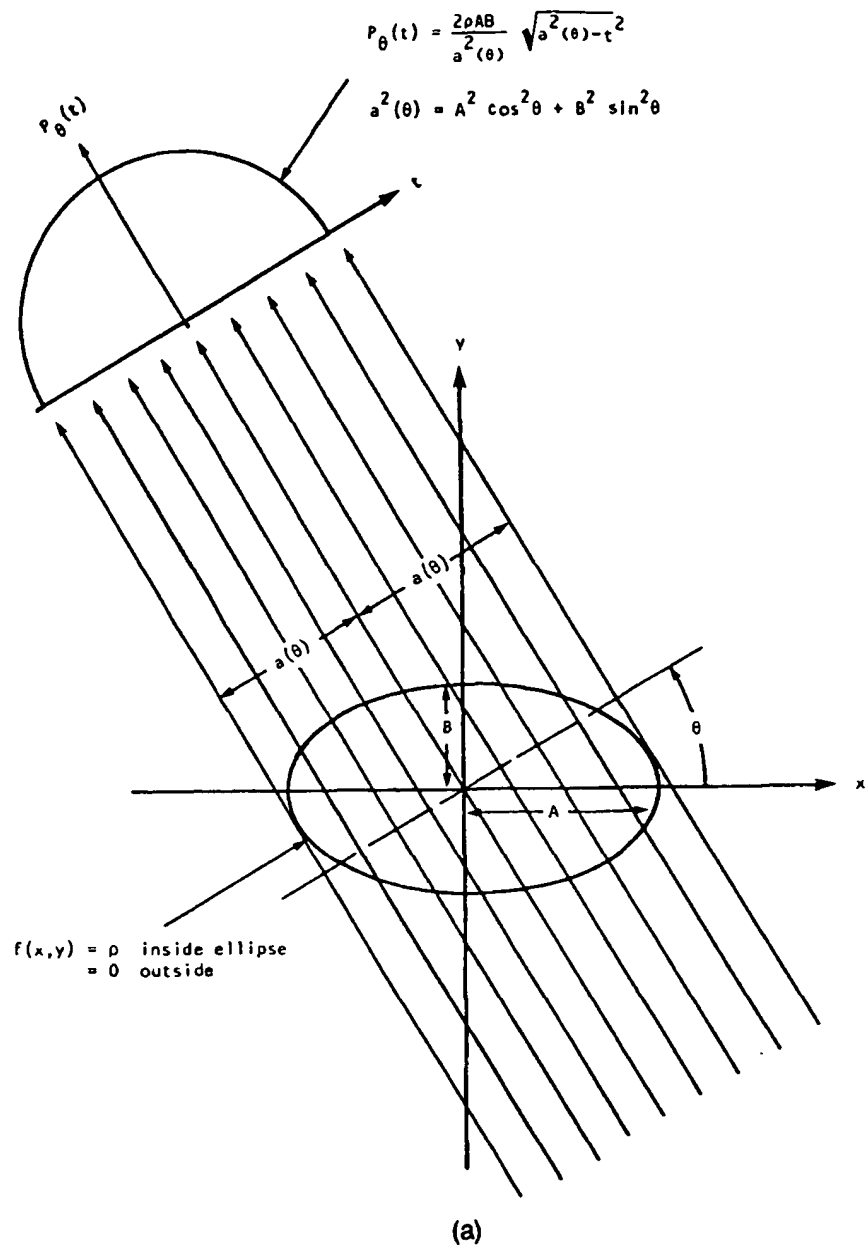
A major advantage of using an image like that in Fig. 3.4(a) for computer simulation is that now one can write analytical expressions for the projections. Note that the projection of an image composed of a number of ellipses is simply the sum of the projections for each of the ellipses; this follows from the linearity of the Radon transform. We will now present
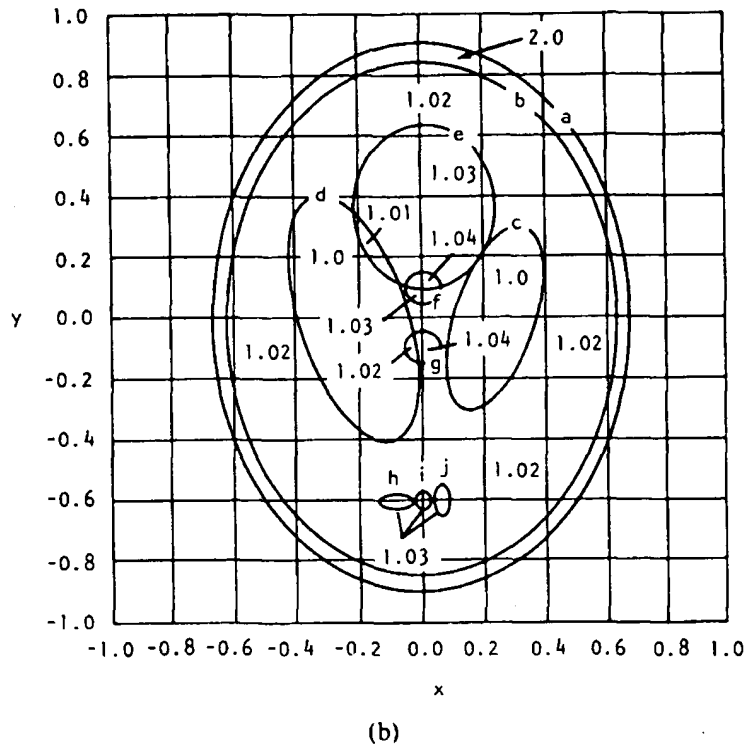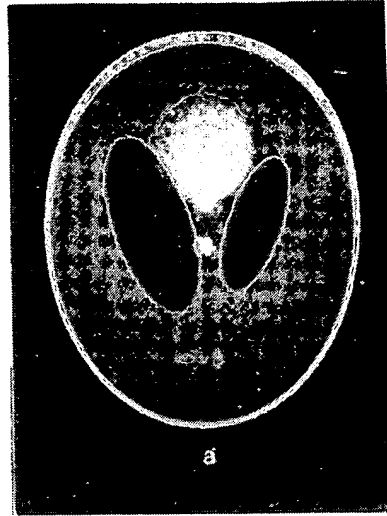
Fig. 3.4: *The Shepp and Logan "head phantom" is shown in (a). Most of the computer simulated results in this chapter were generated using this phantom. The phantom is a superposition of 10 ellipses, each with a size and magnitude as shown in (b). (From [Ros82].)*

expressions for the projections of a single ellipse. Let $f(x, y)$ be as shown in Fig. 3.5(a), i.e.,

$$f(x, y) = \begin{cases} \rho & \text{for } \dfrac{x^2}{A^2} + \dfrac{y^2}{B^2} \le 1 \quad \text{(inside the ellipse)} \\ 0 & \text{otherwise} \qquad \text{(outside the ellipse).} \end{cases} \tag{4}$$

$$P_\theta(t) = \frac{2\rho AB}{a^2(\theta)} \sqrt{a^2(\theta)-t^2}$$

$$a^2(\theta) = A^2 \cos^2\theta + B^2 \sin^2\theta$$

$f(x,y) = \rho$ inside ellipse
$= 0$ outside

Fig. 3.5: *(a) An analytic expression is shown for the projection of an ellipse. For computer simulations a projection can be generated by simply summing the projection of each individual ellipse. (b) Shown here is an ellipse with its center located at (x_1, y_1) and its major axis rotated by α. (From [Ros82].)*

(a)

Fig. 3.5: *Continued.*

(b)
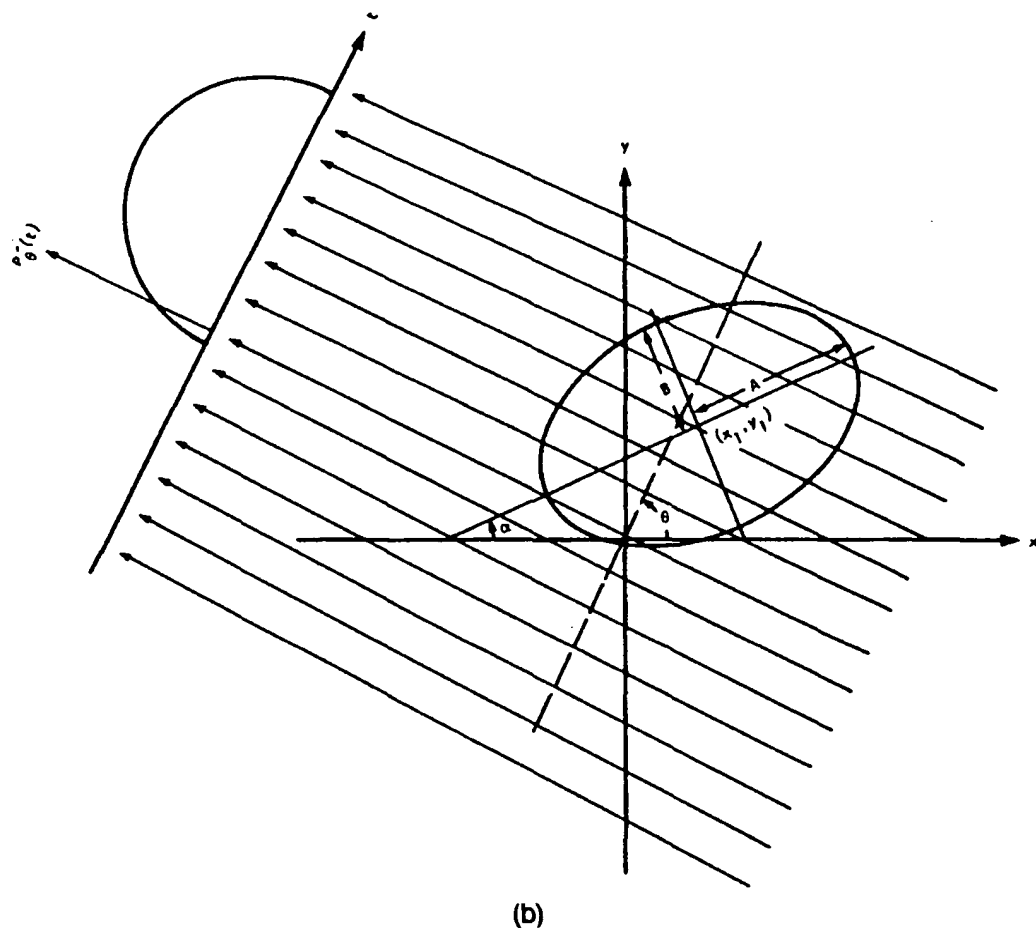
Table 3.1: Summary of parameters for tomography simulations.

Center Coordinate	Major Axis	Minor Axis	Rotation Angle	Refractive Index
(0, 0)	0.92	0.69	90	2.0
(0, −0.0184)	0.874	0.6624	90	−0.98
(0.22, 0)	0.31	0.11	72	−0.02
(−0.22, 0)	0.41	0.16	108	−0.02
(0, 0.35)	0.25	0.21	90	0.01
(0, 0.1)	0.046	0.046	0	0.01
(0, −0.1)	0.046	0.046	0	0.01
(−0.08, −0.605)	0.046	0.023	0	0.01
(0, −0.605)	0.023	0.023	0	0.01
(0.06, −0.605)	0.046	0.023	90	0.01

It is easy to show that the projections of such a function are given by

$$
P_\theta(t) = \begin{cases} \dfrac{2\rho AB}{a^2(\theta)} \sqrt{a^2(\theta) - t^2} & \text{for } |t| \leq a(\theta) \\ 0 & |t| > a(\theta) \end{cases} \tag{5}
$$

where $a^2(\theta) = A^2 \cos^2 \theta + B^2 \sin^2 \theta$. Note that $a(\theta)$ is equal to the projection half-width as shown in Fig. 3.5(a).

Now consider the ellipse described above centered at (x_1, y_1) and rotated by an angle α as shown in Fig. 3.5(b). Let $P'(\theta, t)$ be the resulting projections. They are related to $P_\theta(t)$ in (5) by

$$
P_\theta(t) = P_{\theta-\alpha}(t - s \cos (\gamma - \theta)) \tag{6}
$$

where $s = \sqrt{x_1^2 + y_1^2}$ and $\gamma = \tan^{-1}(y_1/x_1)$.

3.2 The Fourier Slice Theorem

We derive the Fourier Slice Theorem by taking the one-dimensional Fourier transform of a parallel projection and noting that it is equal to a slice of the two-dimensional Fourier transform of the original object. It follows that given the projection data, it should then be possible to estimate the object by simply performing a two-dimensional inverse Fourier transform.

We start by defining the two-dimensional Fourier transform of the object function as

$$
F(u, v) = \int_{-\infty}^{\infty} \int_{-\infty}^{\infty} f(x, y) e^{-j2\pi(ux + vy)} \, dx \, dy. \tag{7}
$$

Likewise define a projection at an angle θ, $P_\theta(t)$, and its Fourier transform by

$$
S_\theta(w) = \int_{-\infty}^{\infty} P_\theta(t) e^{-j2\pi wt} \, dt. \tag{8}
$$

The simplest example of the Fourier Slice Theorem is given for a projection at $\theta = 0$. First, consider the Fourier transform of the object along the line in the frequency domain given by $v = 0$. The Fourier transform integral now simplifies to

$$
F(u, 0) = \int_{-\infty}^{\infty} \int_{-\infty}^{\infty} f(x, y) e^{-j2\pi ux} \, dx \, dy \tag{9}
$$

but because the phase factor is no longer dependent on y we can split the integral into two parts,

$$
F(u, 0) = \int_{-\infty}^{\infty} \left[\int_{-\infty}^{\infty} f(x, y) \, dy \right] e^{-j2\pi ux} \, dx. \tag{10}
$$

From the definition of a parallel projection, the reader will recognize the term

in brackets as the equation for a projection along lines of constant x or

$$P_{\theta=0}(x) = \int_{-\infty}^{\infty} f(x, y)\, dy. \tag{11}$$

Substituting this in (10) we find

$$F(u, 0) = \int_{-\infty}^{\infty} P_{\theta=0}(x)e^{-j2\pi ux}\, dx. \tag{12}$$

The right-hand side of this equation represents the one-dimensional Fourier transform of the projection $P_{\theta=0}$; thus we have the following relationship between the vertical projection and the 2-D transform of the object function:

$$F(u, 0) = S_{\theta=0}(u). \tag{13}$$

This is the simplest form of the Fourier Slice Theorem. Clearly this result is independent of the orientation between the object and the coordinate system. If, for example, as shown in Fig. 3.6 the (t, s) coordinate system is rotated by an angle θ, the Fourier transform of the projection defined in (11) is equal to the two-dimensional Fourier transform of the object along a line rotated by θ. This leads to the Fourier Slice Theorem which is stated as [Kak85]:

Fig. 3.6: *The Fourier Slice Theorem relates the Fourier transform of a projection to the Fourier transform of the object along a radial line. (From [Pan83].)*

The Fourier transform of a parallel projection of an image $f(x, y)$ taken at angle θ gives a slice of the two-dimensional transform, $F(u, v)$, subtending an angle θ with the u-axis. In other words, the Fourier transform of $P_\theta(t)$ gives the values of $F(u, v)$ along line BB in Fig. 3.6.

space domain   frequency domain
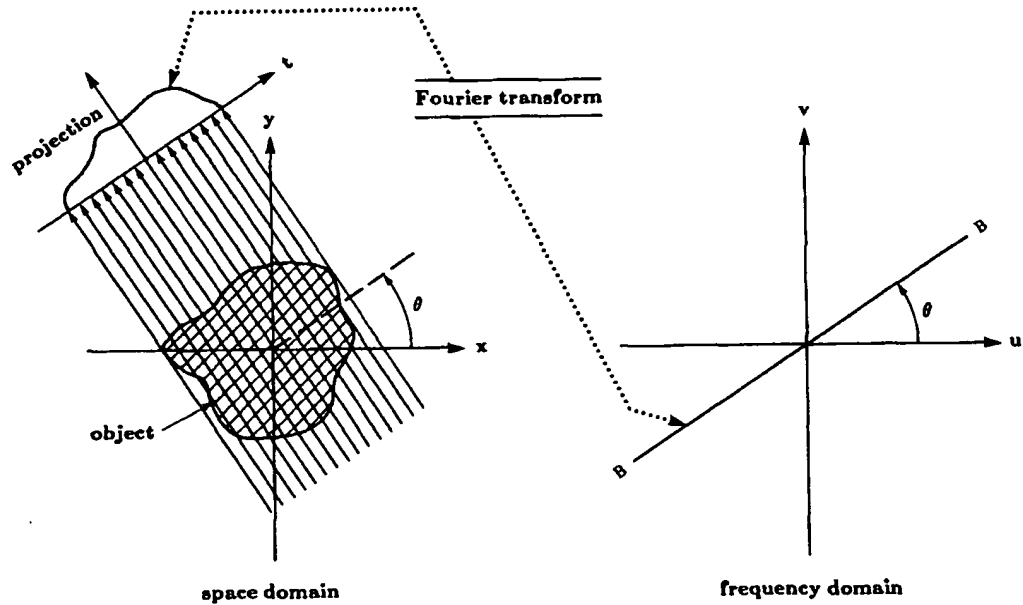
The derivation of the Fourier Slice Theorem can be placed on a more solid foundation by considering the (t, s) coordinate system to be a rotated version of the original (x, y) system as expressed by

$$\begin{bmatrix} t \\ s \end{bmatrix} = \begin{bmatrix} \cos \theta & \sin \theta \\ -\sin \theta & \cos \theta \end{bmatrix} \begin{bmatrix} x \\ y \end{bmatrix} . \tag{14}$$

In the (t, s) coordinate system a projection along lines of constant t is written

$$P_\theta(t) = \int_{-\infty}^{\infty} f(t, s) \, ds \tag{15}$$

and from (8) its Fourier transform is given by

$$S_\theta(w) = \int_{-\infty}^{\infty} P_\theta(t) e^{-j2\pi wt} \, dt. \tag{8}$$

Substituting the definition of a projection into the above equation we find

$$S_\theta(w) = \int_{-\infty}^{\infty} \left[f(t, s) \, ds \right] e^{-j2\pi wt} \, dt. \tag{16}$$

This result can be transformed into the (x, y) coordinate system by using the relationships in (14), the result being

$$S_\theta(w) = \int_{-\infty}^{\infty} \int_{-\infty}^{\infty} f(x, y) e^{-j2\pi w(x \cos \theta + y \sin \theta)} \, dx \, dy. \tag{17}$$

The right-hand side of this equation now represents the two-dimensional Fourier transform at a spatial frequency of $(u = w \cos \theta, v = w \sin \theta)$ or

$$S_\theta(w) = F(w, \theta) = F(w \cos \theta, w \sin \theta). \tag{18}$$

This equation is the essence of straight ray tomography and proves the Fourier Slice Theorem.

The above result indicates that by taking the projections of an object function at angles $\theta_1, \theta_2, \cdots, \theta_k$ and Fourier transforming each of these, we can determine the values of $F(u, v)$ on radial lines as shown in Fig. 3.6. If an infinite number of projections are taken, then $F(u, v)$ would be known at all points in the uv-plane. Knowing $F(u, v)$, the object function $f(x, y)$ can be recovered by using the inverse Fourier transform:

$$f(x, y) = \int_{-\infty}^{\infty} \int_{-\infty}^{\infty} F(u, v) e^{j2\pi(ux+vy)} \, du \, dv. \tag{19}$$

If the function $f(x, y)$ is bounded by $-A/2 < x < A/2$ and $-A/2 < y < A/2$, for the purpose of computation (19) can be written as

$$f(x, y) = \frac{1}{A^2} \sum_m \sum_n F\left(\frac{m}{A}, \frac{n}{A}\right) e^{j2\pi((m/A)x+(n/A)y)} \tag{20}$$

for

$$-\frac{A}{2}<x<\frac{A}{2} \text{ and } -\frac{A}{2}<y<\frac{A}{2}.$$ (21)

Since in practice only a finite number of Fourier components will be known, we can write

$$f(x, y) \approx \frac{1}{A^2} \sum_{m=-N/2}^{N/2} \sum_{n=-N/2}^{N/2} F\left(\frac{m}{A}, \frac{n}{A}\right) e^{j2\pi((m/A)x+(n/A)y)}$$ (22)

for

$$-\frac{A}{2}<x<\frac{A}{2} \text{ and } -\frac{A}{2}<y<\frac{A}{2}$$ (23)

where we arbitrarily assume N to be an even integer. It is clear that the spatial resolution in the reconstructed picture is determined by N. Equation (22) can be rapidly implemented by using the fast Fourier transform (FFT) algorithm provided the N^2 Fourier coefficients $F(m/A, n/A)$ are known.

In practice only a finite number of projections of an object can be taken. In that case it is clear that the function $F(u, v)$ is only known along a finite number of radial lines such as in Fig. 3.7. In order to be able to use (22) one must then interpolate from these radial points to the points on a square grid. Theoretically, one can exactly determine the N^2 coefficients required in (22) provided as many values of the function $F(u, v)$ are known on some radial lines [Cro70]. This calculation involves solving a large set of simultaneous equations often leading to unstable solutions. It is more common to determine the values on the square grid by some kind of nearest neighbor or linear interpolation from the radial points. Since the density of the radial points becomes sparser as one gets farther away from the center, the interpolation error also becomes larger. This implies that there is greater error in the

Fig. 3.7: *Collecting projections of the object at a number of angles gives estimates of the Fourier transform of the object along radial lines. Since an FFT algorithm is used for transforming the data, the dots represent the actual location of estimates of the object's Fourier transform. (From [Pan83].)*

frequency domain
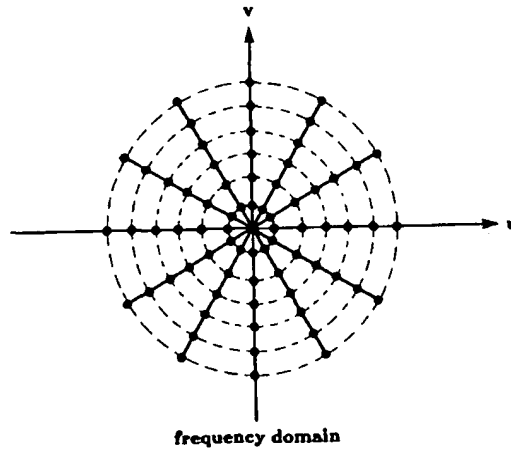
calculation of the high frequency components in an image than in the low frequency ones, which results in some image degradation.

3.3 Reconstruction Algorithms for Parallel Projections

The Fourier Slice Theorem relates the Fourier transform of a projection to the Fourier transform of the object along a single radial. Thus given the Fourier transform of a projection at enough angles the projections could be assembled into a complete estimate of the two-dimensional transform and then simply inverted to arrive at an estimate of the object. While this provides a simple conceptual model of tomography, practical implementations require a different approach.

The algorithm that is currently being used in almost all applications of straight ray tomography is the filtered backprojection algorithm. It has been shown to be extremely accurate and amenable to fast implementation and will be derived by using the Fourier Slice Theorem. This theorem is brought into play by rewriting the inverse Fourier transform in polar coordinates and rearranging the limits of the integration therein. *The derivation of this algorithm is perhaps one of the most illustrative examples of how we can obtain a radically different computer implementation by simply rewriting the fundamental expressions for the underlying theory.*

In this chapter, derivations and implementation details will be presented for the backprojection algorithms for three types of scanning geometries, parallel beam, equiangular fan beam, and equispaced fan beam. The computer implementation of these algorithms requires the projection data to be sampled and then filtered. Using FFT algorithms we will show algorithms for fast computer implementation. Before launching into the mathematical derivations of the algorithms, we will first provide a bit of intuitive rationale behind the filtered backprojection type of approach. If the reader finds this presentation excessively wordy, he or she may go directly to Section 3.3.2.

3.3.1 The Idea

The filtered backprojection algorithm can be given a rather straightforward intuitive rationale because each projection represents a nearly independent measurement of the object. This isn't obvious in the space domain but if the Fourier transform is found of the projection at each angle then it follows easily by the Fourier Slice Theorem. We say that the projections are nearly independent (in a loose intuitive sense) because the only common information in the Fourier transforms of the two projections at different angles is the dc term.

To develop the idea behind the filtered backprojection algorithm, we note that because of the Fourier Slice Theorem the act of measuring a projection can be seen as performing a two-dimensional filtering operation. Consider a single projection and its Fourier transform. By the Fourier Slice Theorem,

this projection gives the values of the object's two-dimensional Fourier transform along a single line. If the values of the Fourier transform of this projection are inserted into their proper place in the object's two-dimensional Fourier domain then a simple (albeit very distorted) reconstruction can be formed by assuming the other projections to be zero and finding the two-dimensional inverse Fourier transform. The point of this exercise is to show that the reconstruction so formed is equivalent to the original object's Fourier transform multiplied by the simple filter shown in Fig. 3.8(b).

What we really want from a simple reconstruction procedure is the sum of projections of the object filtered by pie-shaped wedges as shown in Fig. 3.8(a). It is important to remember that this summation can be done in either the Fourier domain or in the space domain because of the linearity of the Fourier transform. As will be seen later, when the summation is carried out in the space domain, this constitutes the backprojection process.

As the name implies, there are two steps to the filtered backprojection algorithm: the filtering part, which can be visualized as a simple weighting of each projection in the frequency domain, and the backprojection part, which is equivalent to finding the elemental reconstructions corresponding to each wedge filter mentioned above.

The first step mentioned above accomplishes the following: A simple weighting in the frequency domain is used to take each projection and estimate a pie-shaped wedge of the object's Fourier transform. Perhaps the simplest way to do this is to take the value of the Fourier transform of the projection, $S_\theta(w)$, and multiply it by the width of the wedge at that frequency. Thus if there are K projections over $180°$ then at a given frequency w, each wedge has a width of $2\pi|w|/K$. Later when we derive the theory more rigorously, we will see that this factor of $|w|$ represents the Jacobian for a change of variable between polar coordinates and the rectangular coordinates needed for the inverse Fourier transform.

The effect of this weighting by $2\pi|w|/K$ is shown in Fig. 3.8(c). Comparing this to that shown in (a) we see that at each spatial frequency, w, the weighted projection, $(2\pi|w|/K)S_\theta(w)$, has the same "mass" as the pie-shaped wedge. Thus the weighted projections represent an approximation to the pie-shaped wedge but the error can be made as small as desired by using enough projections.

The final reconstruction is found by adding together the two-dimensional inverse Fourier transform of each weighted projection. Because each

Fig. 3.8: *This figure shows the frequency domain data available from one projection. (a) is the ideal situation. A reconstruction could be formed by simply summing the reconstruction from each angle until the entire frequency domain is filled. What is actually measured is shown in (b). As predicted by the Fourier Slice Theorem, a projection gives information about the Fourier transform of the object along a single line. The filtered backprojection algorithm takes the data in (b) and applies a weighting in the frequency domain so that the data in (c) are an approximation to those in (a).*

(a)   (b)   (c)
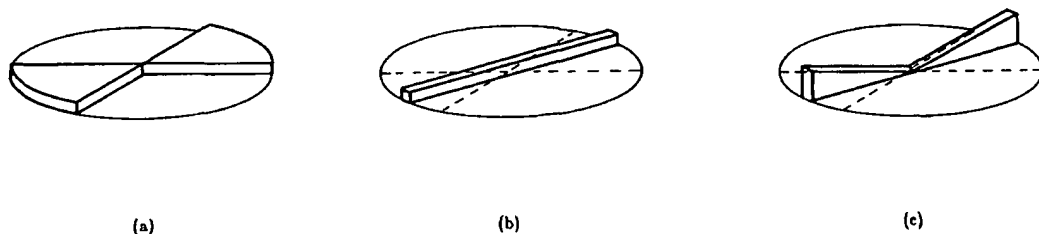
projection only gives the values of the Fourier transform along a single line, this inversion can be performed very fast. This step is commonly called a backprojection since, as we will show in the next section, it can be perceived as the smearing of each filtered projection over the image plane.

The complete filtered backprojection algorithm can therefore be written as:

> Sum for each of the K angles, θ, between 0 and 180°
>> Measure the projection, $P_\theta(t)$
>> Fourier transform it to find $S_\theta(w)$
>> Multiply it by the weighting function $2\pi|w|/K$
>> Sum over the image plane the inverse Fourier transforms of the filtered projections (the backprojection process).

There are two advantages to the filtered backprojection algorithm over a frequency domain interpolation scheme. Most importantly, the reconstruction procedure can be started as soon as the first projection has been measured. This can speed up the reconstruction procedure and reduce the amount of data that must be stored at any one time. To appreciate the second advantage, the reader must note (this will become clearer in the next subsection) that in the filtered backprojection algorithm, when we compute the contribution of each filtered projection to an image point, interpolation is often necessary; it turns out that it is usually more accurate to carry out interpolation in the space domain, as part of the backprojection or smearing process, than in the frequency domain. Simple linear interpolation is often adequate for the backprojection algorithm while more complicated approaches are needed for direct Fourier domain interpolation [Sta81].

Fig. 3.9: *A projection of an ellipse is shown in (a). (b) shows the projection after it has been filtered in preparation for backprojection.*

In Fig. 3.9(a) we show the projection of an ellipse as calculated by (5). To perform a reconstruction it is necessary to filter the projection and then backproject the result as shown in Fig. 3.9(b). The result due to backproject-

(a)

(b)
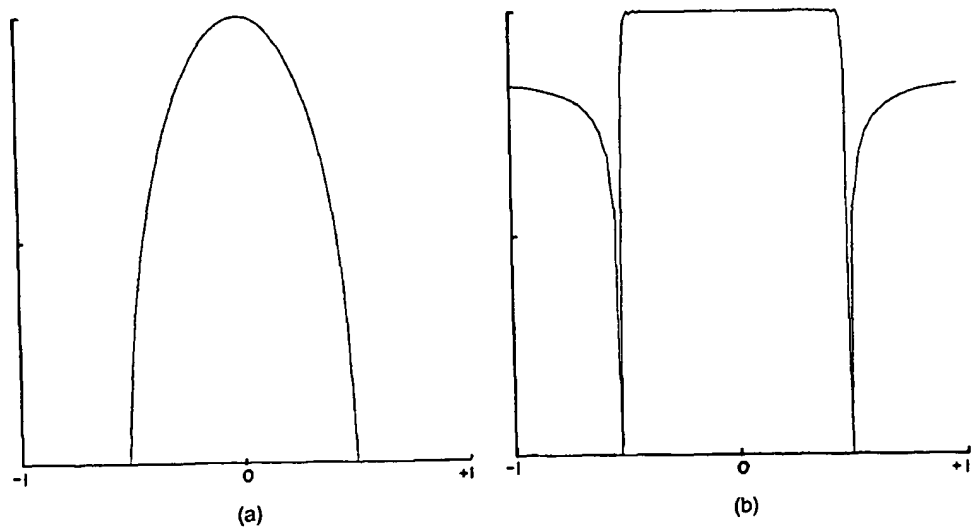
ing one projection is shown in Fig. 3.10. It takes many projections to accurately reconstruct an object; Fig. 3.10 shows the result of reconstructing an object with up to 512 projections.

3.3.2 Theory

We will first present the backprojection algorithm for parallel beam projections. Recalling the formula for the inverse Fourier transform, the object function, $f(x, y)$, can be expressed as

$$f(x, y) = \int_{-\infty}^{\infty} \int_{-\infty}^{\infty} F(u, v) e^{j2\pi(ux+vy)} \, du \, dv. \tag{24}$$

Exchanging the rectangular coordinate system in the frequency domain, (u, v), for a polar coordinate system, (w, θ), by making the substitutions
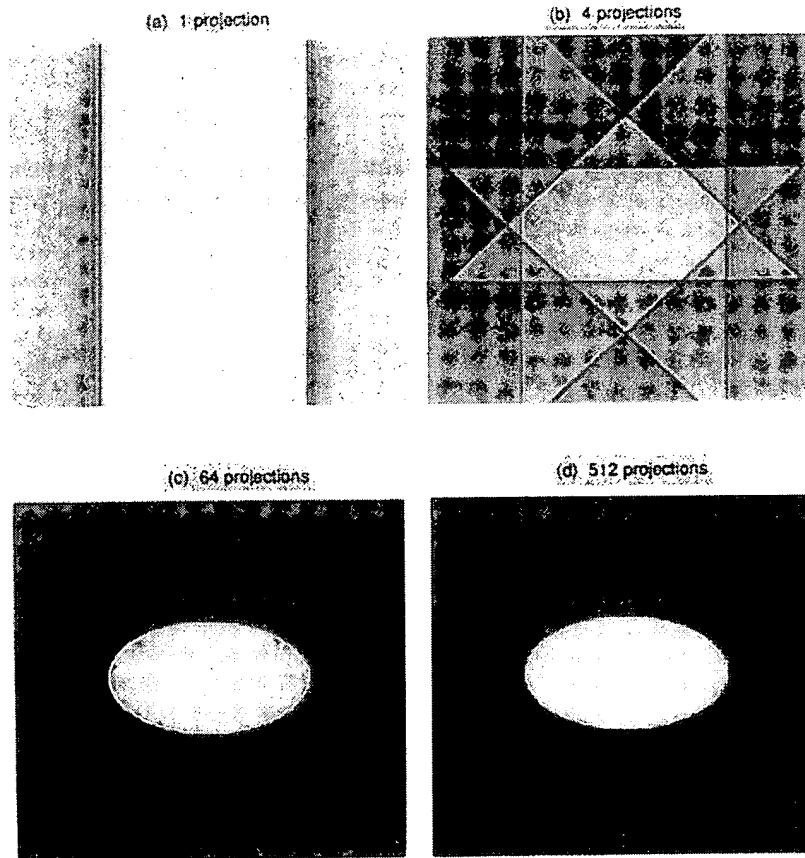
$$u = w \cos \theta \tag{25}$$

$$v = w \sin \theta \tag{26}$$

and then changing the differentials by using

$$du \, dv = w \, dw \, d\theta \tag{27}$$

Fig. 3.10: *The result of backprojecting the projection in Fig. 3.9 is shown here. (a) shows the result of backprojecting for a single angle, (b) shows the effect of backprojecting over 4 angles, (c) shows 64 angles, and (d) shows 512 angles.*

(a) 1 projection
(b) 4 projections
(c) 64 projections
(d) 512 projections

we can write the inverse Fourier transform of a polar function as

$$f(x, y) = \int_0^{2\pi} \int_0^\infty F(w, \theta)e^{j2\pi w(x \cos \theta + y \sin \theta)}w \, dw \, d\theta. \qquad (28)$$

This integral can be split into two by considering θ from $0°$ to $180°$ and then from $180°$ to $360°$,

$$f(x, y) = \int_0^\pi \int_0^\infty F(w, \theta)e^{j2\pi w(x \cos \theta + y \sin \theta)}w \, dw \, d\theta$$

$$+ \int_0^\pi \int_0^\infty F(w, \theta + 180°)e^{j2\pi w[x \cos (\theta + 180°) + y \sin (\theta + 180°)]}w \, dw \, d\theta, \qquad (29)$$

and then using the property

$$F(w, \theta + 180°) = F(-w, \theta) \qquad (30)$$

the above expression for $f(x, y)$ may be written as

$$f(x, y) = \int_0^\pi \left[\int_{-\infty}^\infty F(w, \theta)|w|e^{j2\pi wt} \, dw \right] d\theta. \qquad (31)$$

Here we have simplified the expression by setting

$$t = x \cos \theta + y \sin \theta. \qquad (32)$$

If we substitute the Fourier transform of the projection at angle θ, $S_\theta(w)$, for the two-dimensional Fourier transform $F(w, \theta)$, we get

$$f(x, y) = \int_0^\pi \left[\int_{-\infty}^\infty S_\theta(w)|w|e^{j2\pi wt} \, dw \right] d\theta. \qquad (33)$$

This integral in (33) may be expressed as

$$f(x, y) = \int_0^\pi Q_\theta(x \cos \theta + y \sin \theta) \, d\theta \qquad (34)$$

where

$$Q_\theta(t) = \int_{-\infty}^\infty S_\theta(w)|w|e^{j2\pi wt} \, dw. \qquad (35)$$

This estimate of $f(x, y)$, given the projection data transform $S_\theta(w)$, has a simple form. Equation (35) represents a filtering operation, where the frequency response of the filter is given by $|w|$; therefore $Q_\theta(w)$ is called a "filtered projection." The resulting projections for different angles θ are then added to form the estimate of $f(x, y)$.

Equation (34) calls for each filtered projection, Q_θ, to be "backprojected." This can be explained as follows. To every point (x, y) in the image

plane there corresponds a value of $t = x \cos \theta + y \sin \theta$ for a given value of θ, and the filtered projection Q_θ contributes to the reconstruction its value at t ($= x \cos \theta + y \sin \theta$). This is further illustrated in Fig. 3.11. It is easily shown that for the indicated angle θ, the value of t is the same for all (x, y) on the line LM. *Therefore, the filtered projection, Q_θ, will make the same contribution to the reconstruction at all of these points.* Therefore, one could say that in the reconstruction process each filtered projection, Q_θ, is smeared back, or backprojected, over the image plane.

The parameter w has the dimension of spatial frequency. The integration in (35) must, in principle, be carried out over all spatial frequencies. In practice the energy contained in the Fourier transform components above a certain frequency is negligible, so for all practical purposes the projections may be considered to be bandlimited. If W is a frequency higher than the highest frequency component in each projection, then by the sampling theorem the projections can be sampled at intervals of

$$T = \frac{1}{2W} \tag{36}$$

Fig. 3.11: *Reconstructions are often done using a procedure known as backprojection. Here a filtered projection is smeared back over the reconstruction plane along lines of constant t. The filtered projection at a point t makes the same contribution to all pixels along the line LM in the x-y plane. (From [Ros82].)*

without introducing any error. If we also assume that the projection data are equal to zero for large values of $|t|$ then a projection can be represented as

$$P_\theta(mT), \qquad m = \frac{-N}{2}, \cdots, 0, \cdots, \frac{N}{2} - 1 \tag{37}$$

for some (large) value of N. An FFT algorithm can then be used to
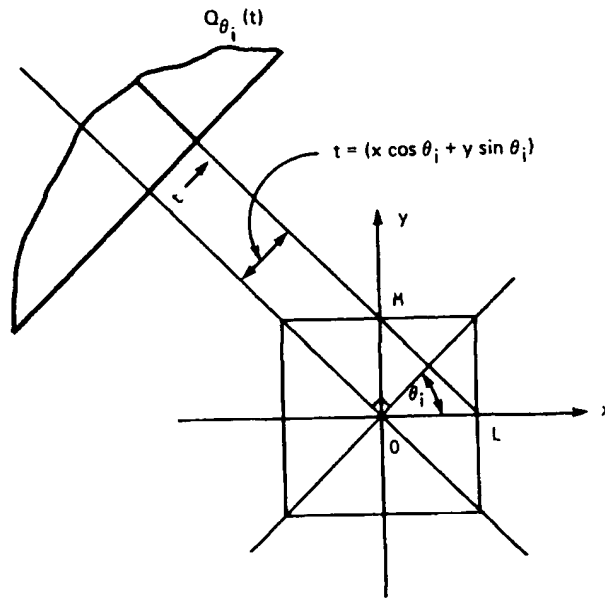
approximate the Fourier transform $S_\theta(w)$ of a projection by

$$S_\theta(w) \approx S\left(m\frac{2W}{N}\right) = \frac{1}{2W} \sum_{k=-N/2}^{N/2-1} P_\theta\left(\frac{k}{2W}\right) e^{-j2\pi(mk/N)}. \quad (38)$$

Given the samples of a projection, (38) gives the samples of its Fourier transform. The next step is to evaluate the "modified projection" $Q_\theta(t)$ digitally. Since the Fourier transforms $S_\theta(w)$ have been assumed to be bandlimited, (35) can be approximated by

$$Q_\theta(t) = \int_{-W}^{W} S_\theta(w)|w|e^{j2\pi wt} \, dw \quad (39)$$

$$\approx \frac{2W}{N} \sum_{m=-N/2}^{N/2} S_\theta\left(m\frac{2W}{N}\right)\left|m\frac{2W}{N}\right| e^{j2\pi m(2W/N)t} \quad (40)$$

provided N is large enough. Again, if we want to determine the projections $Q_\theta(t)$ for only those t at which the projections $P_\theta(t)$ are sampled, we get

$$Q_\theta\left(\frac{k}{2W}\right) \approx \left(\frac{2W}{N}\right) \sum_{m=-N/2}^{N/2} S_\theta\left(m\frac{2W}{N}\right)\left|m\frac{2W}{N}\right| e^{j2\pi(mk/N)} \quad (41)$$

$$k = -N/2, \cdots, -1, 0, 1, \cdots, N/2. \quad (42)$$

By the above equation the function $Q_\theta(t)$ at the sampling points of the projection functions is given (approximately) by the inverse DFT of the product of $S_\theta(m(2W/N))$ and $|m(2W/N)|$. From the standpoint of noise in the reconstructed image, superior results are usually obtained if one multiplies the filtered projection, $S_\theta(2W/N)|m(2W/N)|$, by a function such as a Hamming window [Ham77]:

$$Q_\theta\left(\frac{k}{2W}\right) \approx \left(\frac{2W}{N}\right) \sum_{n=-N/2}^{N/2} S_\theta\left(m\frac{2W}{N}\right)$$
$$\cdot \left|m\frac{2W}{N}\right| H\left(m\frac{2W}{N}\right) e^{j2\pi(mk/N)} \quad (43)$$

where $H(m(2W/N))$ represents the window function used. The purpose of the window function is to deemphasize high frequencies which in many cases represent mostly observation noise. By the familiar convolution theorem for the case of discrete transforms, (43) can be written as

$$Q_\theta\left(\frac{k}{2W}\right) \approx \frac{2W}{N} P_\theta\left(\frac{k}{2W}\right) * \phi\left(\frac{k}{2W}\right) \quad (44)$$

where $*$ denotes circular (periodic) convolution and where $\phi(k/2W)$ is the inverse DFT of the discrete function $|m(2W/N)|H(m(2W/N))$, $m = -N/2, \cdots, -1, 0, 1, \cdots, N/2$.

Clearly at the sampling points of a projection, the function $Q_\theta(t)$ may be obtained either in the Fourier domain by using (40), or in the space domain by using (44). The reconstructed picture $f(x, y)$ may then be obtained by the discrete approximation to the integral in (34), i.e.,

$$f(x, y) = \frac{\pi}{K} \sum_{i=1}^{K} Q_{\theta_i}(x \cos \theta_i + y \sin \theta_i) \tag{45}$$

where the K angles θ_i are those for which the projections $P_\theta(t)$ are known.

Note that the value of $x \cos \theta_i + y \sin \theta_i$ in (45) may not correspond to one of the values of t for which Q_{θ_i} is determined in (43) or in (44). However, Q_{θ_i} for such t may be approximated by suitable interpolation; often linear interpolation is adequate.

Before concluding this subsection we would like to make two comments about the filtering operation in (35). First, note that (35) may be expressed in the t-domain as

$$Q_\theta(t) = \int P_\theta(\alpha) p(t - \alpha) \, d\alpha \tag{46}$$

where $p(t)$ is nominally the inverse Fourier transform of the $|w|$ function in the frequency domain. Since $|w|$ is not a square integrable function, its inverse transform doesn't exist in an ordinary sense. However, one may examine the inverse Fourier transform of

$$|w| e^{-\epsilon |w|} \tag{47}$$

as $\epsilon \to 0$. The inverse Fourier transform of this function, denoted by $p_\epsilon(t)$, is given by

$$p_\epsilon(t) = \frac{\epsilon^2 - (2\pi t)^2}{(\epsilon^2 + (2\pi t)^2)^2} . \tag{48}$$

This function is sketched in Fig. 3.12. Note that for large t we get $p_\epsilon(t) \approx -1/(2\pi t)^2$.

Now our second comment about the filtered projection in (35): This equation may also be written as

$$Q_\theta(t) = \int_{-\infty}^{\infty} j2\pi w S_\theta(w) \left[\frac{-j}{2\pi} \text{sgn}(w) \right] e^{j2\pi wt} \, dw \tag{49}$$
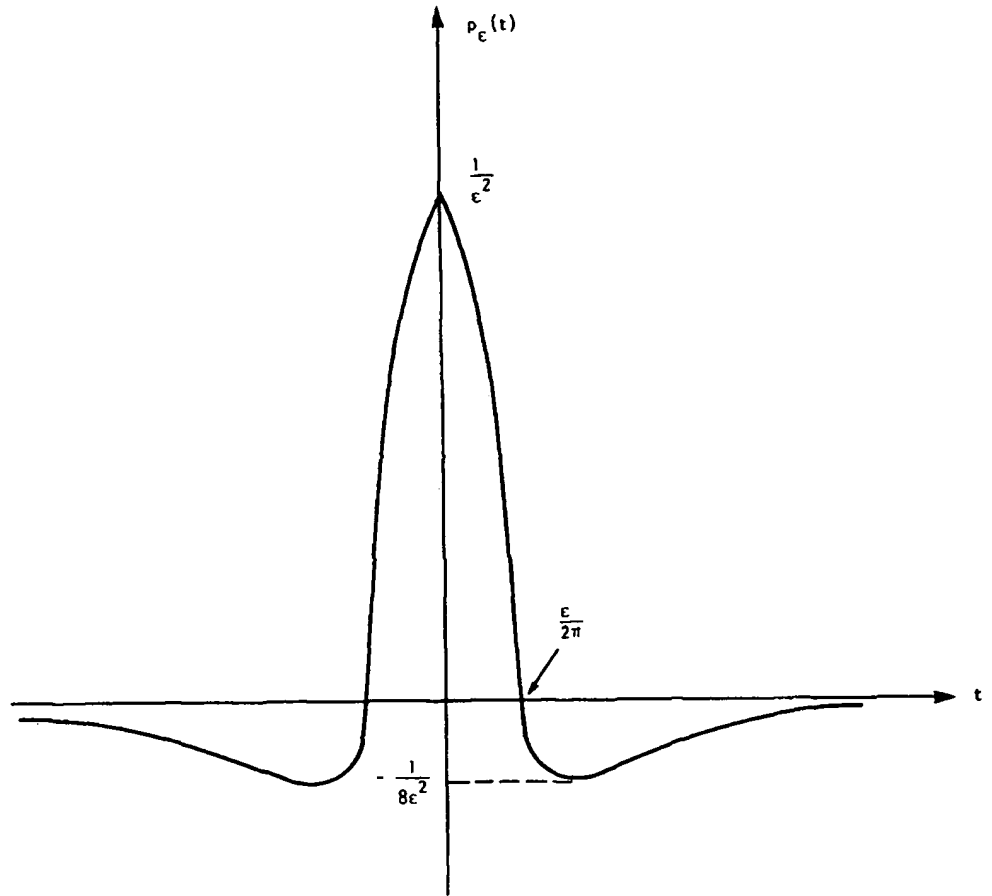
where

$$\text{sgn}(w) = \begin{cases} 1 & \text{for } w > 0 \\ -1 & \text{for } w < 0. \end{cases} \tag{50}$$

By the standard convolution theorem, this equation may be expressed as

$$Q_\theta(t) = \{\text{IFT of } j2\pi w S_\theta(w)\} * \{\text{IFT of } \frac{-j}{2\pi} \text{sgn}(w)\} \tag{51}$$

Fig. 3.12: *An approximation to the impulse response of the ideal backprojection filter is shown here. (From [Ros82].)*

where the symbol * denotes convolution and the abbreviation IFT stands for inverse fast Fourier transform. The IFT of $j2\pi wS_\theta(w)$ is $(\partial/\partial t)P_\theta(t)$ while the IFT of $(-j/2\pi)$ sgn (w) is $1/t$. Therefore, the above result may be written as

$$Q_\theta(t) = \frac{1}{2\pi^2 t} * \frac{\partial P_\theta(t)}{\partial t} \tag{52}$$

$$= \text{Hilbert Transform of } \frac{\partial P_\theta(t)}{\partial t} \tag{53}$$

where, expressed as a filtering operation, the Hilbert Transform is usually defined as the following frequency response:

$$H(w) = \begin{cases} -j, & w > 0 \\ j, & w < 0. \end{cases} \tag{54}$$

### 3.3.3 Computer Implementation of the Algorithm

Let's assume that the projection data are sampled with a sampling interval of τ cm. If there is no aliasing, this implies that in the transform domain the projections don't contain any energy outside the frequency interval $(-W, W)$ where

$$W = \frac{1}{2\tau} \text{ cycles/cm.} \tag{55}$$

Let the sampled projections be represented by $P_\theta(k\tau)$ where k takes integer values. The theory presented in the preceding subsection says that for each sampled projection $P_\theta(k\tau)$ we must generate a filtered $Q_\theta(k\tau)$ by using the periodic (circular) convolution given by (40). Equation (40) is very attractive since it directly conforms to the definition of the DFT and, if N is decomposable, possesses a fast FFT implementation. However, note that (40) is only valid when the projections are of finite bandwidth and finite order. Since these two assumptions (taken together) are never strictly satisfied, computer processing based on (40) usually leads to interperiod interference artifacts created when an aperiodic convolution (required by (35)) is implemented as a periodic convolution. This is illustrated in Fig. 3.13. Fig. 3.13(a) shows a reconstruction of the Shepp and Logan head phantom from 110 projections and 127 rays in each projection using (40) and (45). Equation (40) was implemented with a base 2 FFT algorithm using 128 points. Fig. 3.13(b) shows the reconstructed values on the horizontal line for $y = -0.605$. For comparison we have also shown the values on this line in the original object function.

The comparison illustrated in Fig. 3.13(b) shows that reconstruction based on (42) and (45) introduces a slight "dishing" and a dc shift in the image. These artifacts are partly caused by the periodic convolution implied by (40) and partly by the fact that the implementations in (40) "zero out" all the information in the continuous frequency domain in the cell represented by $m = 0$, whereas the theory (eq. (35)) calls for such "zeroing out" to occur at only *one* frequency, viz. $w = 0$. The contribution to these artifacts by the interperiod interference can be *eliminated* by adequately zero-padding the projection data before using the implementations in (42) or (43).

Zero-padding of the projections also reduces, *but never completely eliminates*, the contribution to the artifacts by the zeroing out of the information in the $m = 0$ cell in (40). This is because zero-padding in the space domain causes the cell size to get smaller in the frequency domain. (If N_{FFT} points are used for performing the discrete Fourier transform, the size of each sampling cell in the frequency domain is equal to $1/N_{FFT}\tau$.) To illustrate the effect of zero-padding, the 127 rays in each projection in the preceding example were padded with 129 zeros to make the data string 256 elements long. These data were transformed by an FFT algorithm and filtered with a $|w|$ function as before. The $y = -0.605$ line through the

(a)
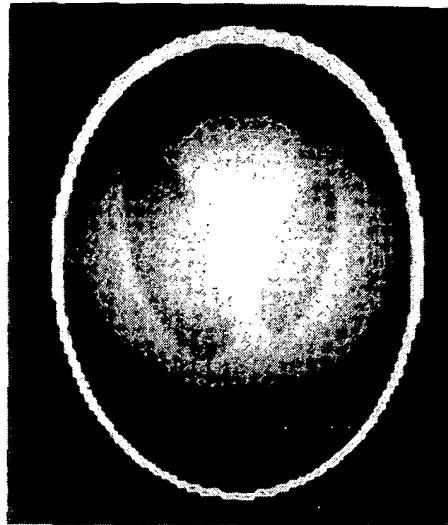
Fig. 3.13: *(a) This reconstruction of the Shepp and Logan phantom shows the artifacts caused when the projection data are not adequately zero-padded and FFTs are used to perform the filtering operation in the filtered backprojection algorithm. The dark regions at the top and the bottom of the reconstruction are the most visible artifacts here. This 128 × 128 reconstruction was made from 110 projections with 127 rays in each projection. (b) A numerical comparison of the true and the reconstructed values on the y = −0.605 line. (For the location of this line see Fig. 3.4.) The "dishing" and the dc shift artifacts are quite evident in this comparison. (c) Shown here are the reconstructed values obtained on the y = −0.605 line if the 127 rays in each projection are zero-padded to 256 points before using the FFTs. The dishing caused by interperiod interference has disappeared; however, the dc shift still remains. (From [Ros82].)*
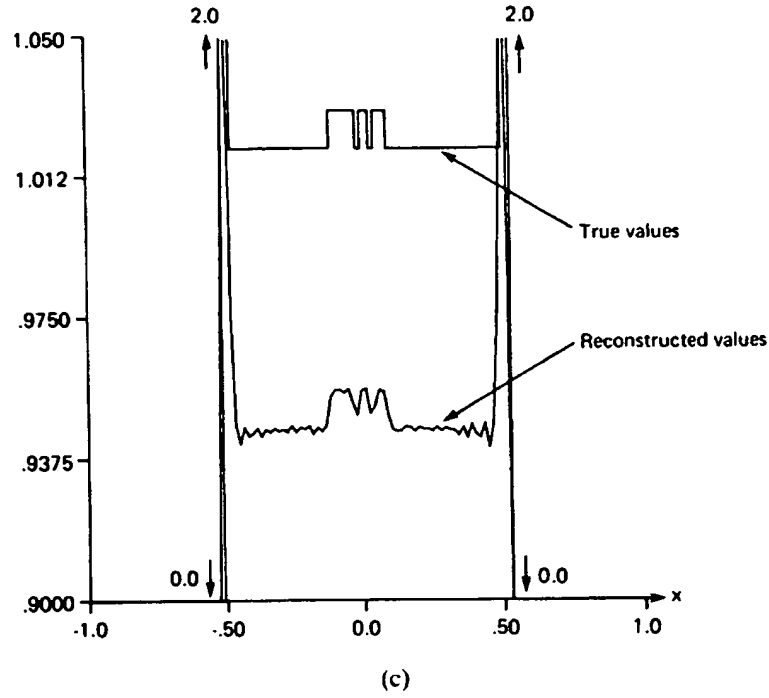

(b)

(c)
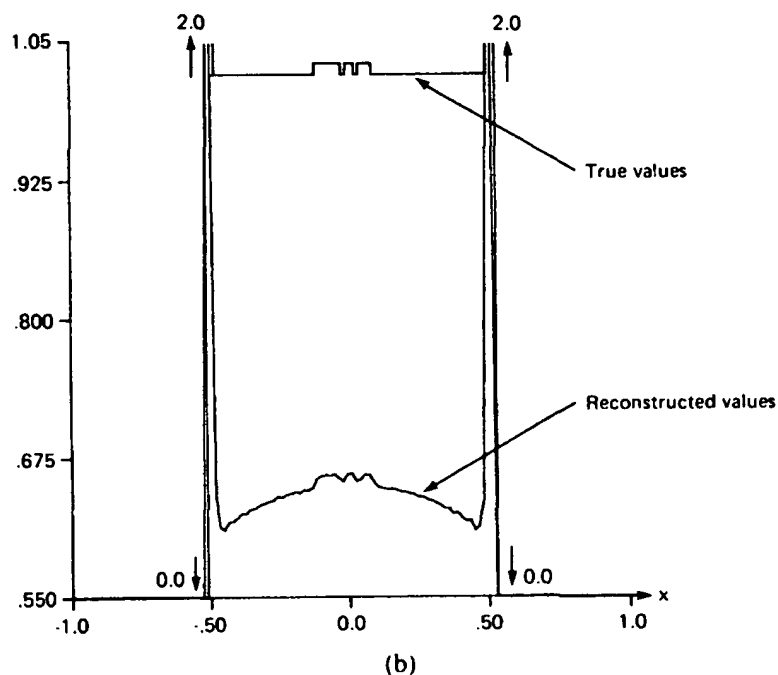
Fig. 3.13: *Continued.*

reconstruction is shown in Fig. 3.13(c), demonstrating that the dishing distortion is now less severe.

We will now show that the artifacts mentioned above can be eliminated by the following alternative implementation of (35) which doesn't require the approximation used in the discrete representation of (40). When the highest frequency in the projections is finite (as given by (55)), (35) may be expressed as

$$Q_\theta(t) = \int_{-\infty}^{\infty} S_\theta(w)H(w)e^{j2\pi wt}\,dw \qquad (56)$$
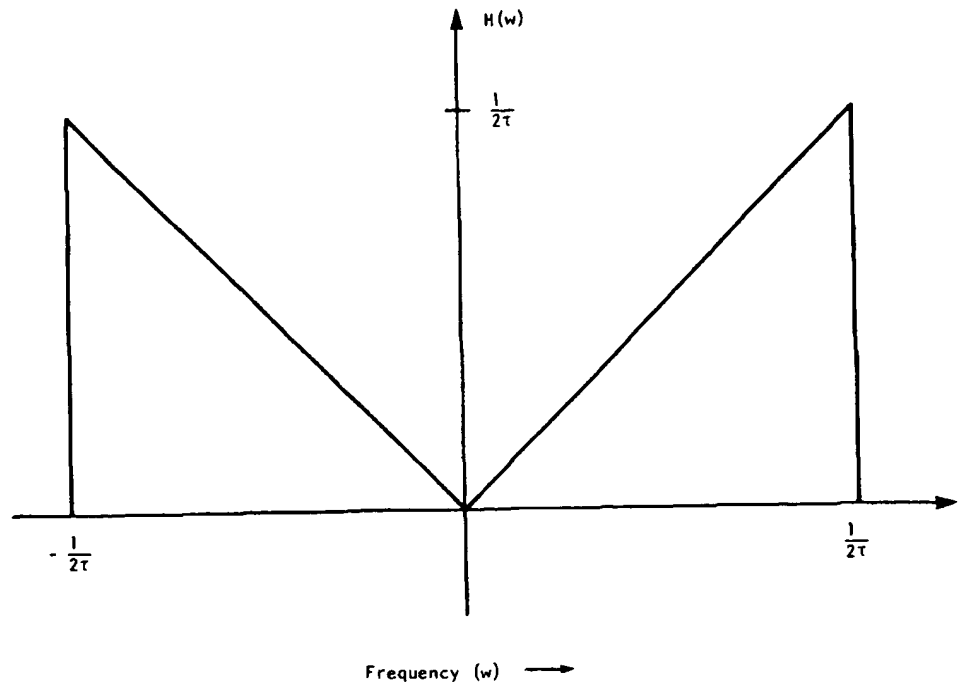
where

$$H(w) = |w|b_w(w) \qquad (57)$$

where, again,

$$b_W(w) = \begin{cases} 1 & |w| < W \\ 0 & \text{otherwise.} \end{cases} \qquad (58)$$

$H(w)$, shown in Fig. 3.14, represents the transfer function of a filter with which the projections must be processed. The impulse response, $h(t)$, of this filter is given by the inverse Fourier transform of $H(w)$ and is

$$h(t) = \int_{-\infty}^{\infty} H(w)e^{+j2\pi wt}\,dw \qquad (59)$$

$$= \frac{1}{2\tau^2}\frac{\sin 2\pi t/2\tau}{2\pi t/2\tau} - \frac{1}{4\tau^2}\left(\frac{\sin \pi t/2\tau}{\pi t/2\tau}\right)^2 \qquad (60)$$

H(w)

$\frac{1}{2\tau}$

$-\frac{1}{2\tau}$

$\frac{1}{2\tau}$

Frequency (w) ⟶

Fig. 3.14: *The ideal filter response for the filtered backprojection algorithm is shown here. It has been bandlimited to 1/2τ. (From [Ros82].)*

where we have used (55). Since the projection data are measured with a sampling interval of τ, for digital processing the impulse response need only be known with the same sampling interval. The samples, $h(n\tau)$, of $h(t)$ are given by

$$h(n\tau) = \begin{cases} 1/4\tau^2, & n = 0 \\ 0, & n \text{ even} \\ -\dfrac{1}{n^2\pi^2\tau^2}, & n \text{ odd.} \end{cases} \tag{61}$$

This function is shown in Fig. 3.15.

Since both $P_\theta(t)$ and $h(t)$ are now bandlimited functions, they may be expressed as

$$P_\theta(t) = \sum_{k=-\infty}^{\infty} P_\theta(k\tau) \frac{\sin 2\pi W(t - k\tau)}{2\pi W(t - k\tau)} \tag{62}$$

$$h(t) = \sum_{k=-\infty}^{\infty} h(k\tau) \frac{\sin 2\pi W(t - k\tau)}{2\pi W(t - k\tau)}. \tag{63}$$

By the convolution theorem the filtered projection (56) can be written as

$$Q_\theta(t) = \int_{-\infty}^{\infty} P_\theta(t')h(t - t') \, dt'. \tag{64}$$
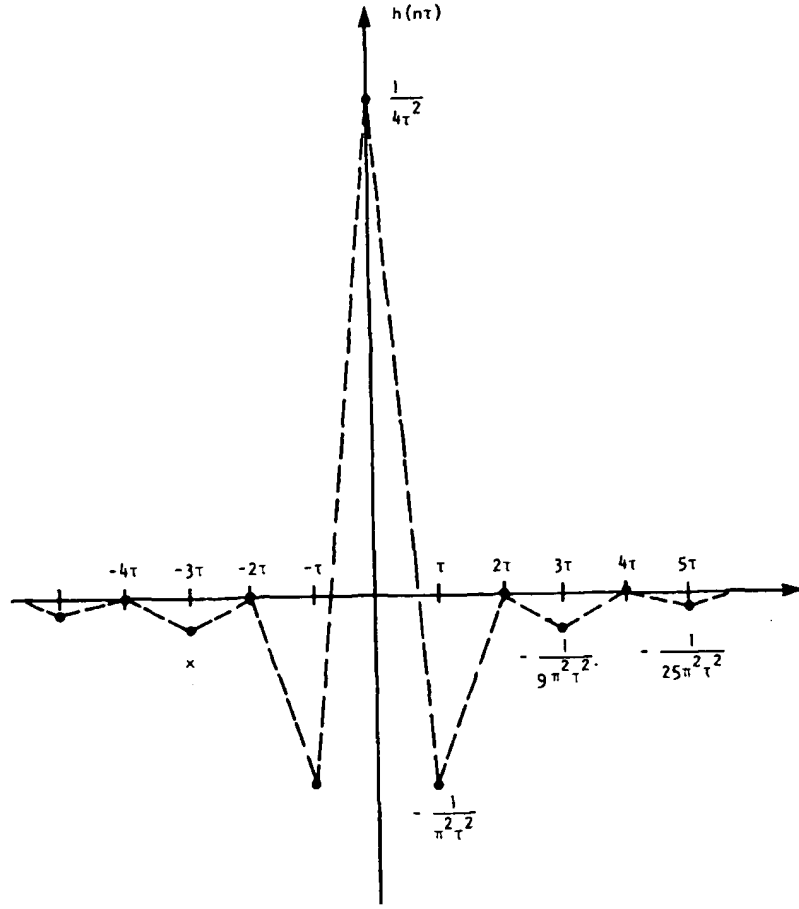
Fig. 3.15: *The impulse response of the filter shown in Fig. 3.14 is shown here. (From [Ros82].)*

Substituting (62) and (63) in (64) we get the following result for the values of the filtered projection at the sampling points:
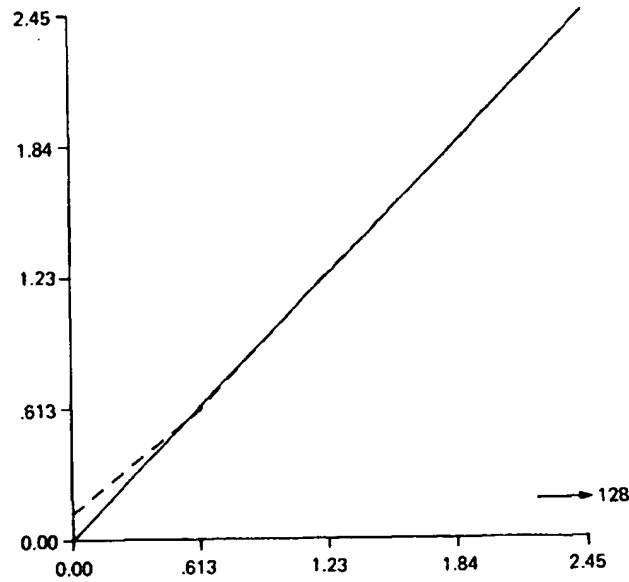
$$Q_\theta(n\tau) = \tau \sum_{k=-\infty}^{\infty} h(n\tau - k\tau) P_\theta(k\tau). \tag{65}$$

In practice each projection is of only finite extent. Suppose that each $P_\theta(k\tau)$ is zero outside the index range $k = 0, \cdots, N - 1$. We may now write the following two equivalent forms of (65):

$$Q_\theta(n\tau) = \tau \sum_{k=0}^{N-1} h(n\tau - k\tau) P_\theta(k\tau), \qquad n = 0, 1, 2, \cdots, N-1 \tag{66}$$

or

$$Q_\theta(n\tau) = \tau \sum_{k=-(N-1)}^{N-1} h(k\tau) P_\theta(n\tau - k\tau), \qquad n = 0, 1, 2, \cdots, N-1. \tag{67}$$

2.45
1.84
1.23
.613
0.00

0.00   .613   1.23   1.84   2.45

——➤ 128

Fig. 3.16: *The DFT of the bandlimited filter (broken line) and that of the ideal filter (solid line) are shown here. Notice the primary difference is in the dc component. (From [Ros82].)*

These equations imply that in order to determine $Q_\theta(n\tau)$ the length of the sequence $h(n\tau)$ used should be from $l = -(N - 1)$ to $l = (N - 1)$. It is important to realize that the results obtained by using (66) or (67) aren't identical to those obtained by using (42). This is because the discrete Fourier transform of the sequence $h(n\tau)$ with n taking values in a finite range [such as when n ranges from $-(N - 1)$ to $(N - 1)$] is not the sequence $|k[(2W)/N]|$. While the latter sequence is zero at $k = 0$, the DFT of $h(n\tau)$ with n ranging from $-(N - 1)$ to $(N - 1)$ is nonzero at this point. This is illustrated in Fig. 3.16.

The discrete convolution in (66) or (67) may be implemented directly on a general purpose computer. However, it is much faster to implement it in the frequency domain using FFT algorithms. [By using specially designed hardware, direct implementation of (66) can be made as fast or faster than the frequency domain implementation.] For the frequency domain implementation one has to keep in mind the fact that one can now only perform periodic (or circular) convolutions, while the convolution required in (66) is aperiodic. To eliminate the interperiod interference artifacts inherent to periodic convolution, we pad the projection data with a sufficient number of zeros. It can easily be shown [Jak76] that if we pad $P_\theta(k\tau)$ with zeros so that it is $(2N - 1)$ elements long, we avoid interperiod interference over the N samples of $Q_\theta(k\tau)$. Of course, if one wants to use the base 2 FFT algorithm, which is most often the case, the sequences $P_\theta(k\tau)$ and $h(k\tau)$ have to be zero-padded so that each is $(2N - 1)_2$ elements long, where $(2N - 1)_2$ is the smallest integer that is a power of 2 and that is greater than $2N - 1$. Therefore, the frequency domain implementation may be expressed as

$$Q_\theta(n\tau) = \tau \times \text{IFFT} \ \{[\text{FFT} \ P_\theta(n\tau) \text{ with ZP}] \times [\text{FFT} \ h(n\tau) \text{ with ZP}]\}, \quad (68)$$

where FFT and IFFT denote, respectively, fast Fourier transform and inverse fast Fourier transform; ZP stands for zero-padding. One usually obtains superior reconstructions when some smoothing is also incorporated in (68). Smoothing may be implemented by multiplying the product of the two FFTs by a Hamming window. When such a window is incorporated, (68) may be rewritten as

$$Q_\theta(n\tau) = \tau \times \text{IFFT } \{[\text{FFT } P_\theta(n\tau) \text{ with ZP}]$$

$$\times [\text{FFT } h(n\tau) \text{ with ZP}] \times \text{smoothing} - \text{window}\}. \qquad (69)$$

After the filtered projections $Q_\theta(n\tau)$ are calculated with the alternative method presented here, the rest of the implementation for reconstructing the image is the same as in the preceding subsection. That is, we use (45) for backprojections and their summation. Again for a given (x, y) and θ_i the argument $x \cos \theta_i + y \sin \theta_i$ may not correspond to one of the $k\tau$ at which Q_{θ_i} is known. This will call for interpolation and often linear interpolation is adequate. Sometimes, in order to eliminate the computations required for interpolation, preinterpolation of the functions $Q_\theta(t)$ is also used. In this technique, which can be combined with the computation in (69), prior to backprojection, the function $Q_\theta(t)$ is preinterpolated onto 10 to 1000 times the number of points in the projection data. From this dense set of points one simply retains the nearest neighbor to obtain the value of Q_{θ_i} at $x \cos \theta_i + y \sin \theta_i$. A variety of techniques are available for preinterpolation [Sch73].

One method of preinterpolation, which combines it with the operations in (69), consists of the following: In (69), prior to performing the IFFT, the *frequency domain function* is padded with a large number of zeros. The inverse transform of this sequency yields the preinterpolated Q_θ. It was recently shown [Kea78] that if the data sequence contains "fractional" frequencies this approach may lead to large errors especially near the beginning and the end of the data sequence. Note that with preinterpolation and with appropriate programming, the backprojection for parallel projection data can be accomplished with virtually no multiplications.

Using the implementation in (68), Fig. 3.17(b) shows the reconstructed values on the line $y = -0.605$ for the Shepp and Logan head phantom. Comparing with Fig. 3.13(b), we see that the dc shift and the dishing have been eliminated. Fig. 3.17(a) shows the complete reconstruction. The number of rays used in each projection was 127 and the number of projections 100. To make convolutions aperiodic, the projection data were padded with zeros to make each projection 256 elements long.

## 3.4 Reconstruction from Fan Projections

The theory in the preceding subsections dealt with reconstructing images from their parallel projections such as those shown in Fig. 3.1. In generating these parallel data a source–detector combination has to linearly scan over the

Fig. 3.17: *(a) Reconstruction obtained by using the filter shown in Fig. 3.16. The 127 rays in the projection were zero-padded so that each projection was 256 elements long. The unit sample response h(nτ) was used with n ranging from − 128 to 127, yielding 256 points for this function. The number of projections was 100 and the display matrix size is 128 × 128. (b) A numerical comparison of the y = − 0.605 line of the reconstruction in (a) with the true values. Note that the dishing and dc shift artifacts visible in Fig. 3.13 have disappeared. (From [Ros82].)*

(a)
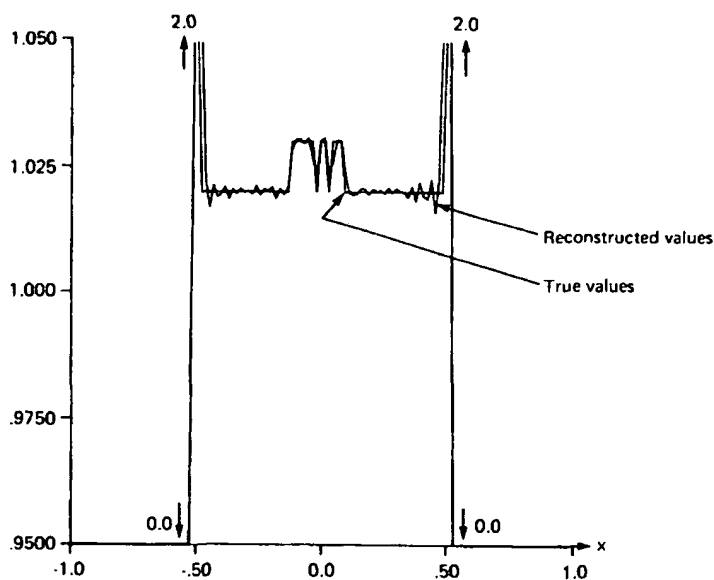
(b)

length of a projection, then rotate through a certain angular interval, then scan linearly over the length of the next projection, and so on. This usually results in times that are as long as a few minutes for collecting all the data. A much faster way to generate the line integrals is by using fan beams such as those shown in Fig. 3.3. One now uses a point source of radiation that emanates a fan-shaped beam. On the other side of the object a bank of detectors is used to make all the measurements in one fan simultaneously. The source and the entire bank of detectors are rotated to generate the desired number of fan projections. As might be expected, one has to pay a price for this simpler and

faster method of data collection; as we will see later the simple backprojection of parallel beam tomography now becomes a weighted backprojection.

There are two types of fan projections depending upon whether a projection is sampled at equiangular or equispaced intervals. This difference is illustrated in Fig. 3.18. In (a) we have shown an equiangular set of rays. If the detectors for the measurement of line integrals are arranged on the straight line D_1D_2, this implies unequal spacing between them. If, however, the detectors are arranged on the arc of a circle whose center is at S, they may now be positioned with equal spacing along this arc (Fig. 3.18(b)). The second type of fan projection is generated when the rays are arranged such that the detector spacing on a straight line is now equal (Fig. 3.18(c)). The algorithms that reconstruct images from these two different types of fan projections are different and will be separately derived in the following subsection.

3.4.1 Equiangular Rays

Let $R_\beta(\gamma)$ denote a fan projection as shown in Fig. 3.19. Here β is the angle that the source S makes with a reference axis, and the angle γ gives the location of a ray within a fan. Consider the ray SA. If the projection data were generated along a set of parallel rays, then the ray SA would belong to a parallel projection $P_\theta(t)$ for θ and t given by

$$\theta = \beta + \gamma \quad \text{and} \quad t = D \sin \gamma \tag{70}$$

where D is the distance of the source S from the origin O. The relationships in (70) are derived by noting that all the rays in the parallel projection at angle θ are perpendicular to the line PQ and that along such a line the distance OB is equal to the value of t. Now we know that from parallel projections $P_\theta(t)$ we may reconstruct $f(x, y)$ by
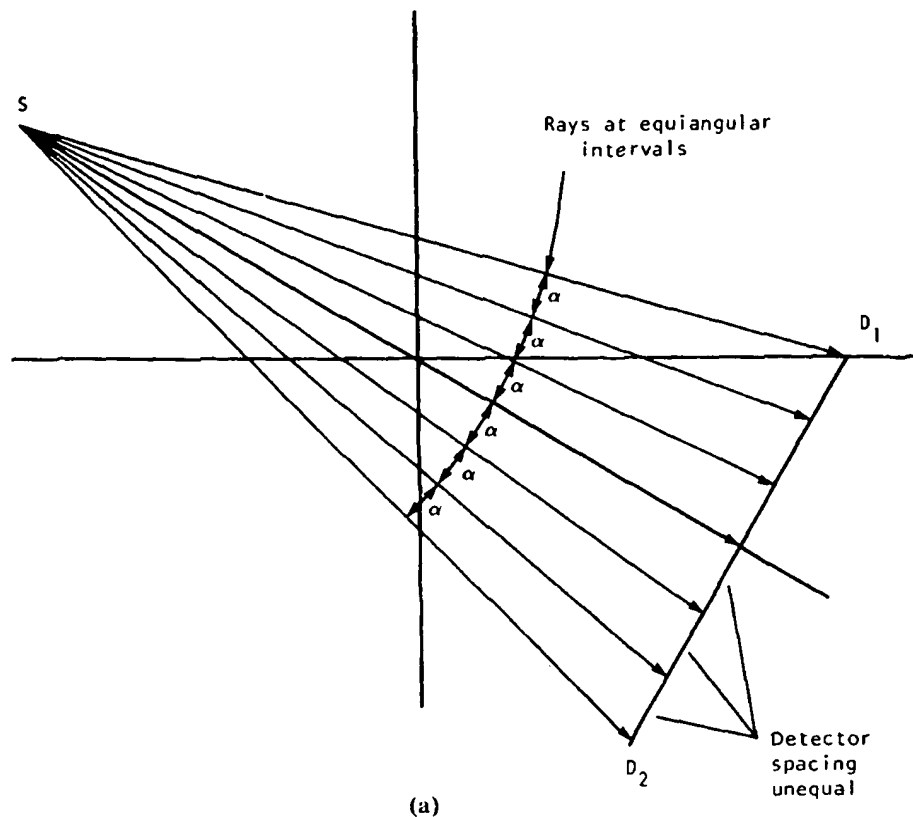
$$f(x, y) = \int_0^\pi \int_{-t_m}^{t_m} P_\theta(t) h(x \cos \theta + y \sin \theta - t) \, dt \, d\theta \tag{71}$$

where t_m is the value of t for which $P_\theta(t) = 0$ with $|t| > t_m$ in all projections. This equation only requires the parallel projections to be collected over $180°$. However, if one would like to use the projections generated over $360°$, this equation may be rewritten as
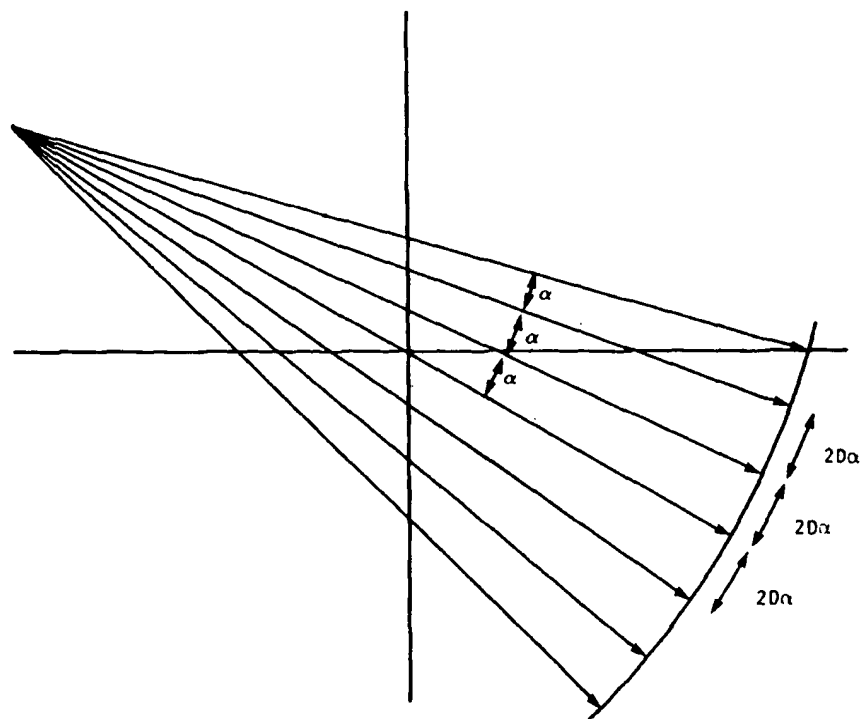
$$f(x, y) = \frac{1}{2} \int_0^{2\pi} \int_{-t_m}^{t_m} P_\theta(t) h(x \cos \theta + y \sin \theta - t) \, dt \, d\theta. \tag{72}$$

Derivation of the algorithm becomes easier when the point (x, y) (marked C in Fig. 3.20) is expressed in polar coordinates (r, ϕ), that is,

$$x = r \cos \phi \qquad y = r \sin \phi. \tag{73}$$

S

Rays at equiangular
intervals

α
α
α
α
α
α

D₁ → D_1

Detector
spacing
unequal

D₂ → D_2

(a)

α
α
α

2Dα
2Dα
2Dα

(b)

Fig. 3.18: *Two different types of fan beams are shown here. In (a) the angle between rays is constant but the detector spacing is uneven. If the detectors are placed along a circle the spacing will then be equal as shown in (b). As shown in (c) the detectors can be arranged with constant spacing along a line but then the angle between rays is not constant. (From [Ros82].)*
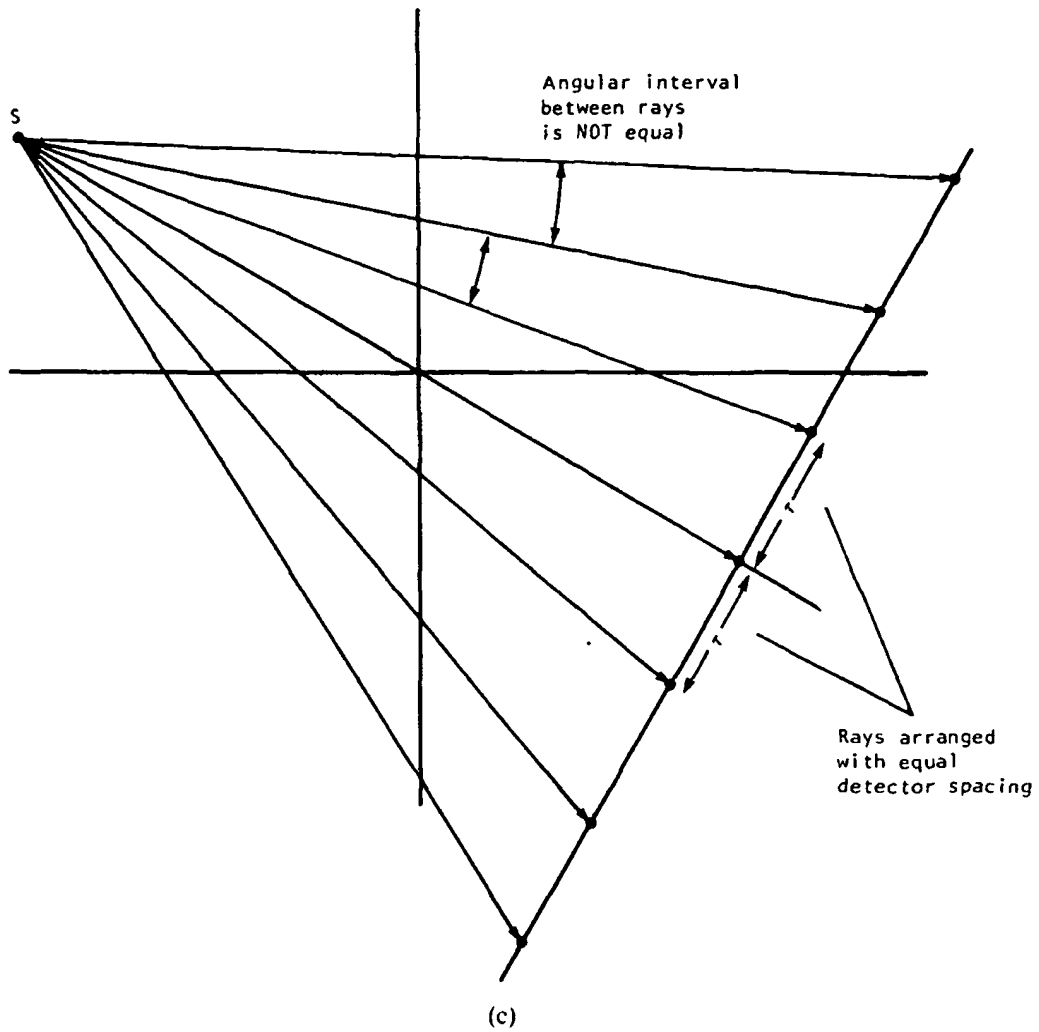
S

Angular interval
between rays
is NOT equal

Rays arranged
with equal
detector spacing

(c)

Fig. 3.18: *Continued.*

The expression in (72) can now be written as

$$f(r, \phi) = \frac{1}{2} \int_0^{2\pi} \int_{-t_m}^{t_m} P_\theta(t) h(r \cos (\theta - \phi) - t) \, dt \, d\theta. \tag{74}$$

Using the relationships in (70), the double integration may be expressed in terms of γ and β,

$$f(r, \phi) = \frac{1}{2} \int_{-\gamma}^{2\pi-\gamma} \int_{-\sin^{-1}(t_m/D)}^{\sin^{-1}(t_m/D)} P_{\beta+\gamma}(D \sin \gamma) h(r \cos (\beta + \gamma - \phi)$$

$$- d \sin \gamma) D \cos \gamma \, d\gamma \, d\beta \tag{75}$$

where we have used $dt \, d\theta = D \cos \gamma \, d\gamma \, d\beta$. A few observations about this expression are in order. The limits $-\gamma$ to $2\pi - \gamma$ for β cover the entire range of $360°$. Since all the functions of β are periodic (with period 2π) these limits
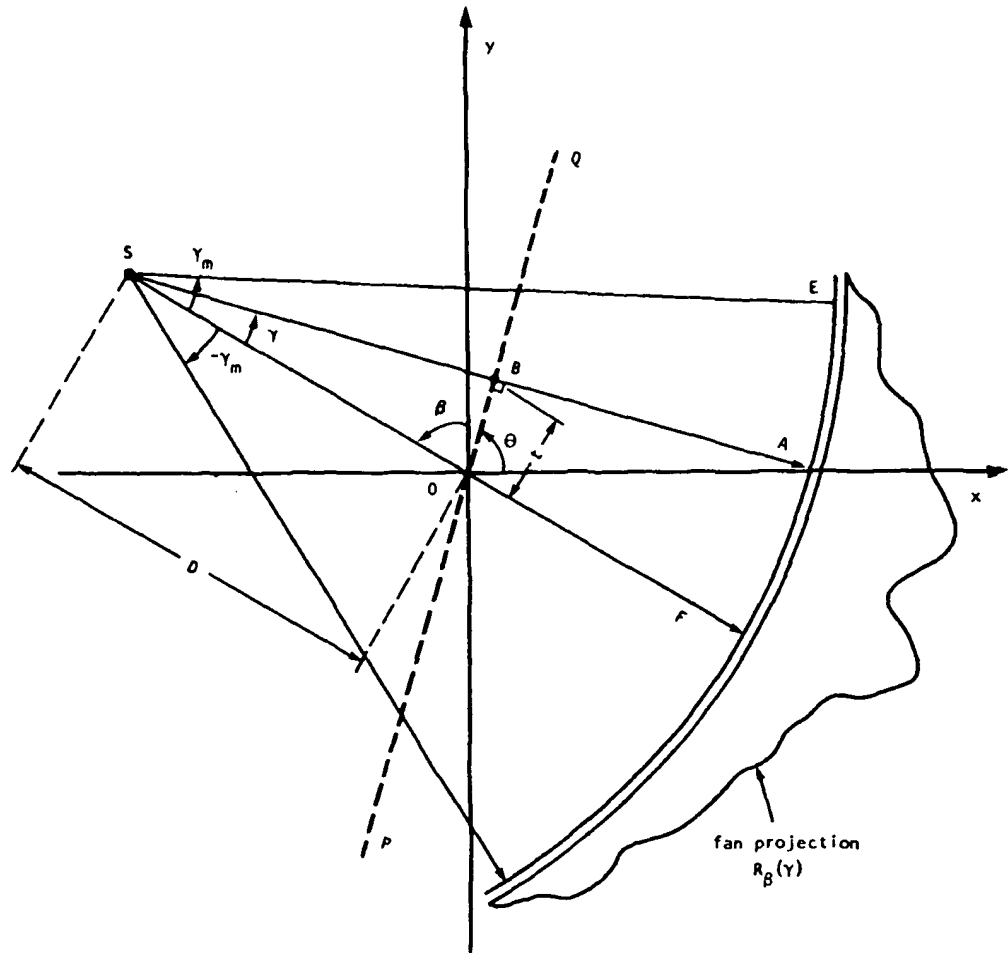
**Fig. 3.19:** *An equiangular fan is shown here. Each ray is identified by its angle γ from the central ray. (From [Ros82].)*

may be replaced by 0 and 2π, respectively. $\text{Sin}^{-1}\,(t_m/D)$ is equal to the value of γ for the extreme ray SE in Fig. 3.19. Therefore, the upper and lower limits for γ may be written as γ_m and $-\gamma_m$, respectively. The expression $P_{\beta+\gamma}(D\,\sin\,\gamma)$ corresponds to the ray integral along SA in the parallel projection data $P_\theta(t)$. The identity of this ray integral in the fan projection data is simply $R_\beta(\gamma)$. Introducing these changes in (75) we get

$$f(r,\,\phi) = \frac{1}{2}\int_0^{2\pi}\int_{-\gamma_m}^{\gamma_m} R_\beta(\gamma)h(r\,\cos\,(\beta+\gamma-\phi)-D\,\sin\,\gamma)D\,\cos\,\gamma\,d\gamma\,d\beta.$$

$$(76)$$

In order to express the reconstruction formula given by (76) in a form that can be easily implemented on a computer we will first examine the argument
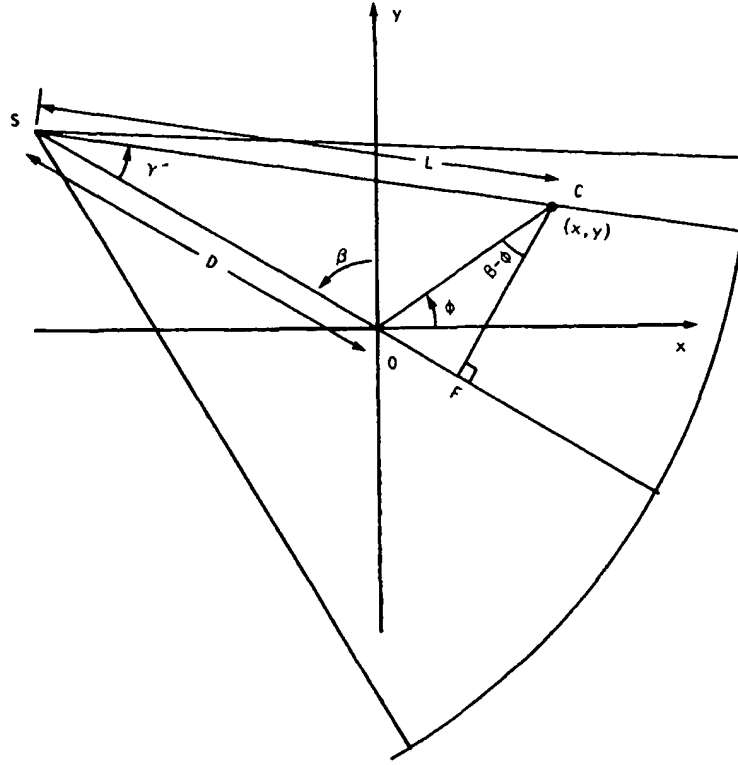
Fig. 3.20: *This figure illustrates that L is the distance of the pixel at location (x, y) from the source S; and γ is the angle that the source-to-pixel line subtends with the central ray. (From [Ros82].)*

of the function h. The argument may be rewritten as

$$r \cos (\beta + \gamma - \phi) - D \sin \gamma$$

$$= r \cos (\beta - \phi) \cos \gamma - [r \sin (\beta - \phi) + D] \sin \gamma. \qquad (77)$$

Let L be the distance from the source S to a point (x, y) [or (r, ϕ) in polar coordinates] such as C in Fig. 3.20. Clearly, L is a function of three variables, r, ϕ, and β. Also, let γ' be the angle of the ray that passes through this point (r, ϕ). One can now easily show that

$$L \cos \gamma' = D + r \sin (\beta - \phi)$$

$$L \sin \gamma' = r \cos (\beta - \phi). \qquad (78)$$

Note that the pixel location (r, ϕ) and the projection angle β completely determine both L and γ':

$$L(r, \phi, \beta) = \sqrt{[D + r \sin (\beta - \phi)]^2 + [r \cos (\beta - \phi)]^2} \qquad (79)$$

and

$$\gamma' = \tan^{-1} \frac{r \cos (\beta - \phi)}{D + r \sin (\beta - \phi)}. \qquad (80)$$

Using (78) in (77) we get for the argument of h

$$r \cos (\beta + \gamma - \phi) - D \sin \gamma = L \sin (\gamma' - \gamma) \qquad (81)$$

and substituting this in (76) we get

$$f(r, \phi) = \frac{1}{2} \int_0^{2\pi} \int_{-\gamma_m}^{\gamma_m} R_\beta(\gamma) h(L \sin (\gamma' - \gamma)) D \cos \gamma \, d\gamma \, d\beta. \qquad (82)$$

We will now express the function $h(L \sin (\gamma' - \gamma))$ in terms of $h(t)$. Note that $h(t)$ is the inverse Fourier transform of $|w|$ in the frequency domain:

$$h(t) = \int_{-\infty}^{\infty} |w| e^{j2\pi wt} \, dw. \qquad (83)$$

Therefore,

$$h(L \sin \gamma) = \int_{-\infty}^{\infty} |w| e^{j2\pi wL \sin \gamma} \, dw. \qquad (84)$$

Using the transformation

$$w' = \frac{wL \sin \gamma}{\gamma} \qquad (85)$$

we can write

$$h(L \sin \gamma) = \left(\frac{\gamma}{L \sin \gamma} \right)^2 \int_{-\infty}^{\infty} |w'| e^{j2\pi w'\gamma} \, dw' \qquad (86)$$

$$= \left(\frac{\gamma}{L \sin \gamma} \right)^2 h(\gamma). \qquad (87)$$

Therefore, (82) may be written as

$$f(r, \phi) = \int_0^{2\pi} \frac{1}{L^2} \int_{-\gamma_m}^{\gamma_m} R_\beta(\gamma) g(\gamma' - \gamma) D \cos \gamma \, d\gamma \, d\beta \qquad (88)$$

where

$$g(\gamma) = \frac{1}{2} \left(\frac{\gamma}{\sin \gamma} \right)^2 h(\gamma). \qquad (89)$$

For the purpose of computer implementation, (88) may be interpreted as a weighted filtered backprojection algorithm. To show this we rewrite (88) as follows:

$$f(r, \phi) = \int_0^{2\pi} \frac{1}{L^2} Q_\beta(\gamma') \, d\beta \qquad (90)$$

where

$$Q_\beta(\gamma) = R'_\beta(\gamma) * g(\gamma) \qquad (91)$$

and where

$$R'_\beta(\gamma) = R_\beta(\gamma) \cdot D \cdot \cos \gamma. \qquad (92)$$

This calls for reconstructing an image using the following three steps:

Step 1:

Assume that each projection $R_\beta(\gamma)$ is sampled with sampling interval α. The known data then are $R_{\beta_i}(n\alpha)$ where n takes integer values. β_i are the angles at which projections are taken. The first step is to generate for each fan projection $R_{\beta_i}(n\alpha)$ the corresponding $R'_{\beta_i}(n\alpha)$ by

$$R'_{\beta_i}(n\alpha) = R_{\beta_i}(n\alpha) \cdot D \cdot \cos n\alpha. \qquad (93)$$

Note that $n = 0$ corresponds to the ray passing through the center of the projection.

Step 2:

Convolve each modified projection $R'_{\beta_i}(n\alpha)$ with $g(n\alpha)$ to generate the corresponding filtered projection:

$$Q_{\beta_i}(n\alpha) = R'_{\beta_i}(n\alpha) * g(n\alpha). \qquad (94)$$

To perform this discrete convolution using an FFT program the function $R'_{\beta_i}(n\alpha)$ must be padded with a sufficient number of zeros to avoid interperiod interference artifacts. The sequence $g(n\alpha)$ is given by the samples of (89):

$$g(n\alpha) = \frac{1}{2} \left(\frac{n\alpha}{\sin n\alpha} \right)^2 h(n\alpha). \qquad (95)$$

If we substitute in this the values of $h(n\alpha)$ from (61), we get for the discrete impulse response

$$g(n\alpha) = \begin{cases} \dfrac{1}{8\alpha^2}, & n = 0 \\[2mm] 0, & n \text{ is even} \\[2mm] \left(\dfrac{\alpha}{\pi\alpha \sin n\alpha} \right)^2, & n \text{ is odd}. \end{cases} \qquad (96)$$

Although, theoretically, no further filtering of the projection data than that called for by (94) is required, in practice superior reconstructions are obtained if a certain amount of smoothing is combined with the required filtering:

$$Q_{\beta_i}(n\alpha) = R'_{\beta_i}(n\alpha) * g(n\alpha) * k(n\alpha) \qquad (97)$$

$Q_{\theta_i}(t)$

(a)
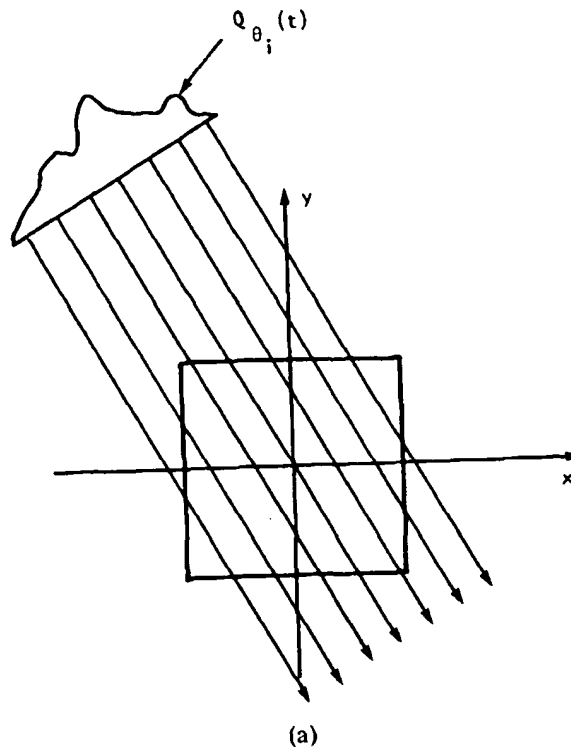
Fig. 3.21: *While the filtered projections are backprojected along parallel lines for the parallel beam case (a), for the fan beam case the backprojection is performed along converging lines (b). (c) This figure illustrates the implementation step that in order to determine the backprojected value at pixel (x, y), one must first compute* γ' *for that pixel. (From [Ros82].)*
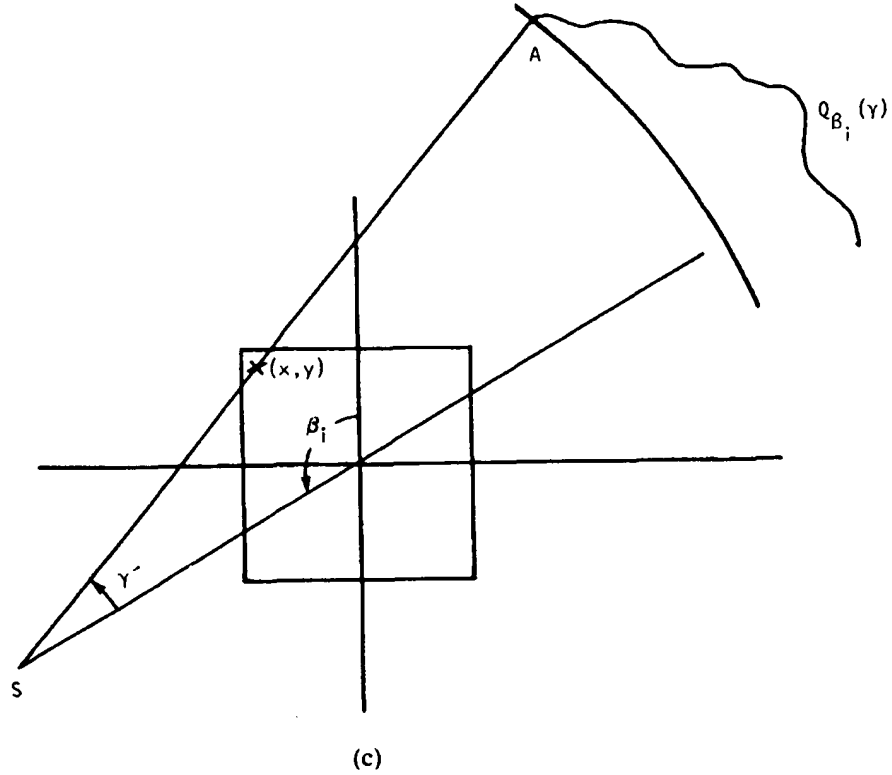
β_i

(b)

(c)
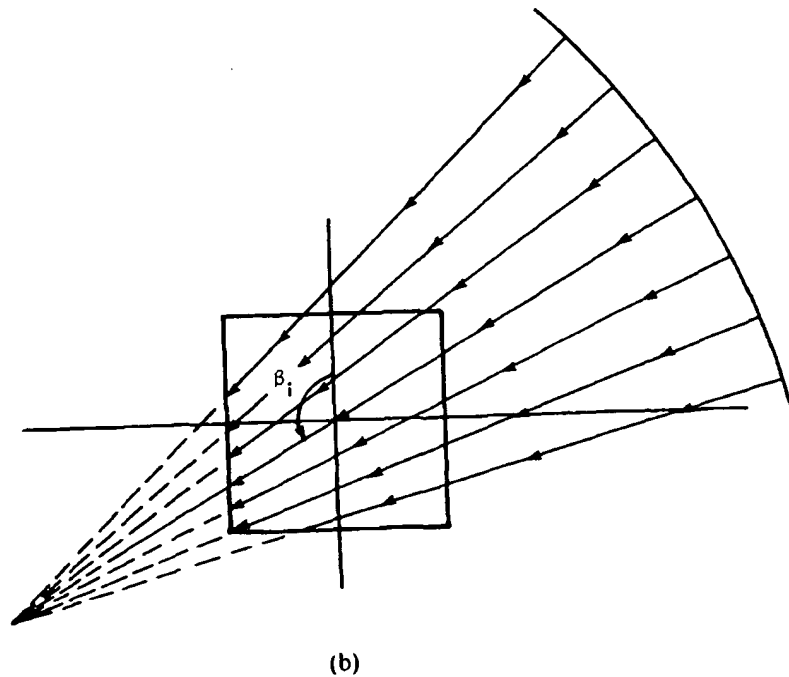
where $k(n\alpha)$ is the impulse response of the smoothing filter. In the frequency domain implementation this smoothing filter may be a simple cosine function or a Hamming window.

Step 3:

Perform a *weighted* backprojection of each filtered projection *along the fan*. Since the backprojection here is very different from that for the parallel case, we will explain it in some detail. For the parallel case the filtered projection is backprojected along a set of parallel lines as shown in Fig. 3.21(a). For the fan beam case the backprojection is done along the fan (Fig. 3.21(b)). This is dictated by the structure of (90):

$$f(x, y) \approx \Delta\beta \sum_{i=1}^{M} \frac{1}{L^2(x, y, \beta_i)} Q_{\beta_i}(\gamma')$$ (98)

where γ' is the angle of the fan beam ray that passes through the point (x, y) and $\Delta\beta = 2\pi/M$. For β_i chosen in Fig. 3.21(c) in order to find the contribution of $Q_{\beta_i}(\gamma)$ to the point (x, y) shown there one must first find the angle, γ', of the ray SA that passes through that point (x, y). $Q_{\beta_i}(\gamma')$ will then be contributed from the filtered projection at β_i to the point (x, y) under consideration. Of course, the computed value of γ' may not correspond to one of $n\alpha$ for which $Q_{\beta_i}(n\alpha)$ is known. One must

then use interpolation. The contribution $Q_{\beta_i}(\gamma')$ at the point (x, y) must then be divided by L^2 where L is the distance from the source S to the point (x, y).

This concludes our presentation of the algorithm for reconstructing projection data measured with detectors spaced at equiangular increments.

3.4.2 Equally Spaced Collinear Detectors

Let $R_\beta(s)$ denote a fan projection as shown in Fig. 3.22, where s is the distance along the straight line corresponding to the detector bank. The principal difference between the algorithm presented in the preceding subsection and the one presented here lies in the way a fan projection is represented, which then introduces differences in subsequent mathematical manipulations. Before, fan projections were sampled at equiangular intervals and we represented them by $R_\beta(\gamma)$ where γ represented the angular location of a ray. Now we represent them by $R_\beta(s)$.

Although the projections are measured on a line such as D_1D_2 in Fig. 3.22,

Fig. 3.22: *For the case of equispaced detectors on a straight line, each projection is denoted by the function $R_\beta(s)$. (From [Ros82].)*
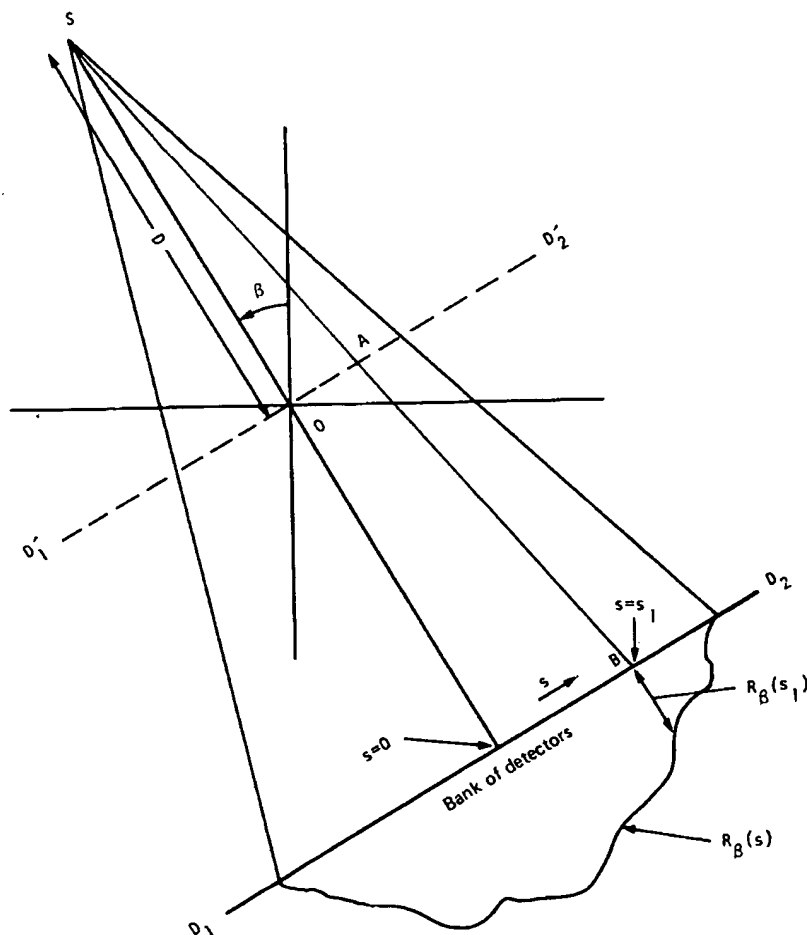
for theoretical purposes it is more efficient to assume the existence of an imaginary detector line $D_1'\,D_2'$ passing through the origin. We now associate the ray integral along SB with point A on $D_1'\,D_2'$, as opposed to point B on $D_1 D_2$. Thus in Fig. 3.23 we will associate a fan projection $R_\beta(s)$ with the imaginary detector line $D_1'\,D_2'$. Now consider a ray SA in the figure; the value of s for this ray is the length of OA. If parallel projection data were generated for the object under consideration, the ray SA would belong to a parallel projection $P_\theta(t)$ with θ and t as shown in the figure. The relationship between β and t for the parallel case is given by

$$t = s \cos \gamma \qquad \theta = \beta + \gamma$$

$$t = \frac{sD}{\sqrt{D^2 + s^2}} \qquad \theta = \beta + \tan^{-1} \frac{s}{D} \tag{99}$$

where use has been made of the fact that angle AOC is equal to angle OSC, and where D is the distance of the source point S from the origin O.

Fig. 3.23: *This figure illustrates several of the parameters used in the derivation of the reconstruction algorithm for equispaced detectors. (From [Ros82].)*

In terms of the parallel projection data the reconstructed image is given by (74) which is repeated here for convenience:

$$f(r, \phi) = \frac{1}{2} \int_0^{2\pi} \int_{-t_m}^{t_m} P_\theta(t) h(r \cos (\theta - \phi) - t) \, dt \, d\theta \tag{74}$$
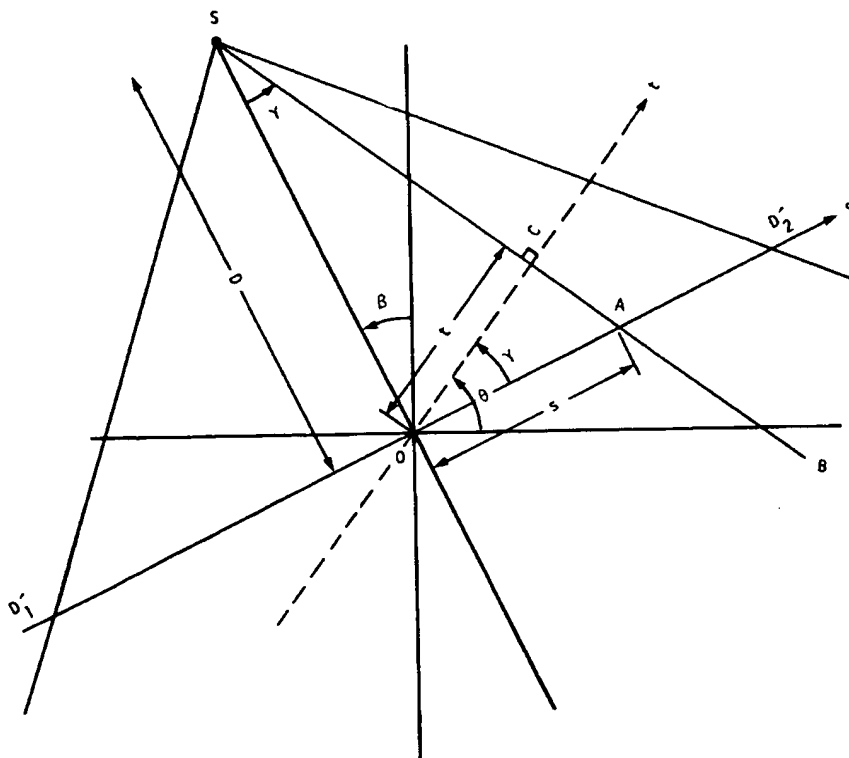
where $f(r, \phi)$ is the reconstructed image in polar coordinates. Using the relationships in (99) the double integration may be expressed as

$$f(r, \phi) = \frac{1}{2} \int_{-\tan^{-1}(S_m/D)}^{2\pi-\tan^{-1}(S_m/D)} \int_{-S_m}^{S_m} P_{\beta+\gamma}\left(\frac{sD}{\sqrt{D^2+s^2}}\right)$$

$$\cdot h\left[r \cos\left(\beta+\tan^{-1}\left(\frac{s}{D}\right)-\phi\right)-\frac{Ds}{\sqrt{D^2+s^2}}\right] \frac{D^3}{(D^2+s^2)^{3/2}} \, ds \, d\beta$$

(100)

where we have used

$$dt \, d\theta = \frac{D^3}{(D^2+s^2)^{3/2}} \, ds \, d\beta.$$

(101)

In (100) s_m is the largest value of s in each projection and corresponds to t_m for parallel projection data. The limits $-\tan^{-1}(s_m/D)$ and $2\pi-\tan^{-1}(s_m/D)$ cover the angular interval of 360°. Since all functions of β in (100) are periodic with period 2π, these limits may be replaced by 0 and 2π, respectively. Also, the expression

$$P_{\beta+\gamma}\left(\frac{sD}{\sqrt{D^2+s^2}}\right)$$

(102)

corresponds to the ray integral along SA in the parallel projection data $P_\theta(t)$. The identity of this ray integral in the fan projection data is simply $R_\beta(s)$. Introducing these changes in (100) we get

$$f(r, \phi) = \frac{1}{2} \int_0^{2\pi} \int_{-S_m}^{S_m} R_\beta(s) h \left(r \cos\left(\beta+\tan^{-1}\frac{s}{D}-\phi\right)\right.$$

$$\left.-\frac{Ds}{\sqrt{D^2+s^2}}\right) \frac{D^3}{(D^2+s^2)^{3/2}} \, ds \, d\beta. \quad (103)$$

In order to express this formula in a filtered backprojection form we will first examine the argument of h. The argument may be written as

$$r \cos\left(\beta+\tan^{-1}\frac{s}{D}-\phi\right)-\frac{Ds}{\sqrt{D^2+s^2}}$$

$$= r \cos(\beta-\phi) \frac{D}{\sqrt{D^2+s^2}} - (D+r \sin(\beta-\phi)) \frac{s}{\sqrt{D^2+s^2}}. \quad (104)$$

We will now introduce two new variables that are easily calculated in a computer implementation. The first of these, denoted by U, is for each pixel (x, y) the ratio of SP (Fig. 3.24) to the source-to-origin distance. Note that
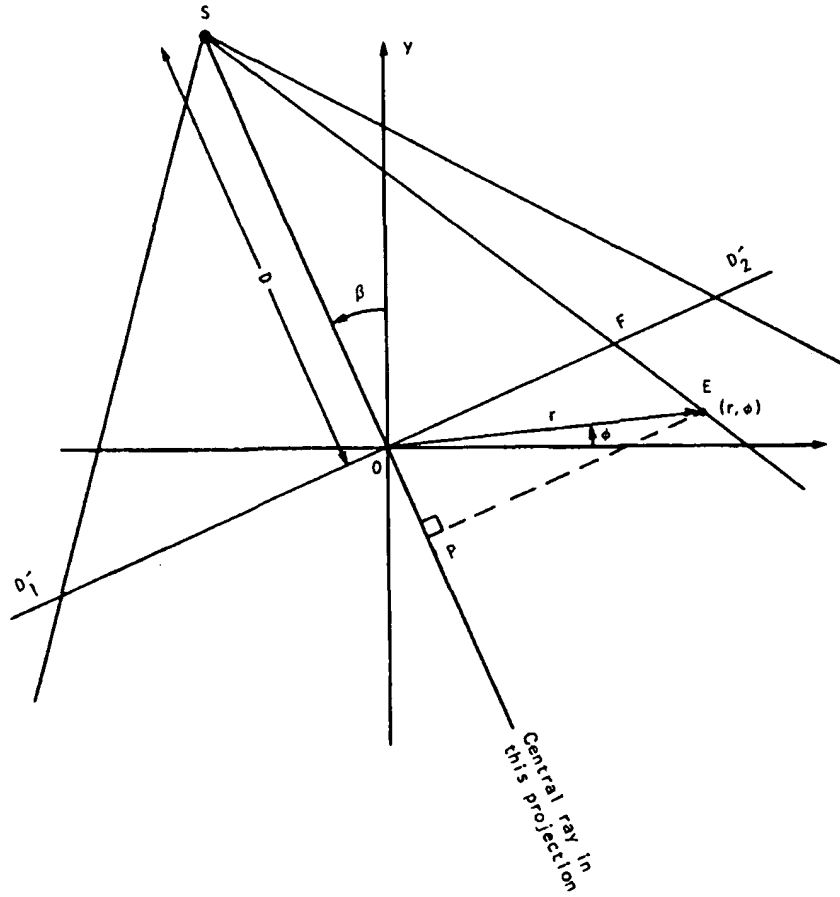
Fig. 3.24: *For a pixel at the polar coordinates (r, ϕ) the variable U is the ratio of the distance SP, which is the projection of the source to pixel line on the central ray, to the source-to-center distance. (Adapted from [Ros82].)*

SP is the projection of the source to pixel distance SE on the central ray. Thus

$$U(r, \phi, \beta) = \frac{\overline{SO} + \overline{OP}}{D} \tag{105}$$

$$= \frac{D + r \sin (\beta - \phi)}{D} . \tag{106}$$

The other parameter we want to define is the value of s for the ray that passes through the pixel (r, ϕ) under consideration. Let s' denote this value of s. Since s is measured along the imaginary detector line $D_1' D_2'$, it is given by the distance OF. Since

$$\frac{s'}{\overline{SO}} = \frac{\overline{EP}}{\overline{SP}} \tag{107}$$

we have

$$s' = D \frac{r \cos (\beta - \phi)}{D + r \sin (\beta - \phi)} . \tag{108}$$

Equations (106) and (108) can be utilized to express (104) in terms of U and s':

$$r \cos \left(\beta + \tan^{-1} \frac{s}{D} - \phi \right) \frac{Ds}{\sqrt{D^2 + s^2}} = \frac{s'UD}{\sqrt{D^2 + s^2}} - \frac{sUD}{\sqrt{D^2 + s^2}}. \quad (109)$$

Substituting (109) in (103), we get

$$f(r, \phi) = \frac{1}{2} \int_0^{2\pi} \int_{-S_m}^{S_m} R_\beta(s) h \left[(s' - s) \frac{UD}{\sqrt{D^2 + s^2}} \right] \frac{D^3}{(D^2 + s^2)^{3/2}} \, ds \, d\beta. \quad (110)$$

We will now express the convolving kernel h in this equation in a form closer to that given by (61). Note that, nominally, $h(t)$ is the inverse Fourier transform of $|w|$ in the frequency domain:

$$h(t) = \int_{-\infty}^{\infty} |w| e^{j2\pi wt} \, dw. \quad (111)$$

Therefore,

$$h \left[(s' - s) \frac{UD}{\sqrt{D^2 + s^2}} \right] = \int_{-\infty}^{\infty} |w| e^{j2\pi w (s' - s)(UD/\sqrt{D^2 + s^2})} \, dw. \quad (112)$$

Using the transformation

$$w' = w \frac{UD}{\sqrt{D^2 + s^2}} \quad (113)$$

we can rewrite (112) as follows:

$$h \left[(s' - s) \frac{UD}{\sqrt{D^2 + s^2}} \right] = \frac{D^2 + s^2}{U^2 D^2} \int_{-\infty}^{\infty} |w'| e^{j2\pi (s' - s)w'} \, dw' \quad (114)$$

$$= \frac{D^2 + s^2}{U^2 D^2} h(s' - s). \quad (115)$$

Substituting this in (110) we get

$$f(r, \phi) = \int_0^{2\pi} \frac{1}{U^2} \int_{-\infty}^{\infty} R_\beta(s) g(s' - s) \frac{D}{\sqrt{D^2 + s^2}} \, ds \, d\beta \quad (116)$$

where

$$g(s) = \frac{1}{2} h(s). \quad (117)$$

For the purpose of computer implementation, (116) may be interpreted as a weighted filtered backprojection algorithm. To show this we rewrite (116) as

follows:

$$f(r, \phi) = \int_0^{2\pi} \frac{1}{U^2} Q_\beta(s') \, d\beta \qquad (118)$$

where

$$Q_\beta(s) = R_\beta'(s) * g(s) \qquad (119)$$

and

$$R_\beta'(s) = R_\beta(s) \cdot \frac{D}{\sqrt{D^2 + s^2}} \cdot \qquad (120)$$

Equations (118) through (120) suggest the following steps for computer implementation:

Step 1:

Assume that each projection $R_\beta(s)$ is sampled with a sampling interval of a. The known data then are $R_{\beta_i}(na)$ where n takes integer values with $n = 0$ corresponding to the central ray passing through the origin; β_i are the angles for which fan projections are known. The first step is to generate for each fan projection $R_{\beta_i}(na)$ the corresponding modified projection $R_{\beta_i}'(na)$ given by

$$R_{\beta_i}'(na) = R_{\beta_i}(na) \cdot \frac{D}{\sqrt{D^2 + n^2 a^2}} \cdot \qquad (121)$$

Step 2:

Convolve each modified projection $R_{\beta_i}'(na)$ with $g(na)$ to generate the corresponding filtered projection:

$$Q_{\beta_i}(na) = R_{\beta_i}(na) * g(na) \qquad (122)$$

where the sequence $g(na)$ is given by the samples of (117):

$$g(na) = \frac{1}{2} h(na). \qquad (123)$$

Substituting in this the values of $h(na)$ given in (61) we get for the impulse response of the convolving filter:

$$g(na) = \begin{cases} \dfrac{1}{8a^2}, & n = 0 \\[2ex] 0, & n \text{ even} \\[2ex] -\dfrac{1}{2n^2\pi^2 a^2}, & n \text{ odd}. \end{cases} \qquad (124)$$

When the convolution of (122) is implemented in the frequency domain using an FFT algorithm the projection data must be padded with a sufficient number of zeros to avoid distortion due to interperiod interference.

In practice superior reconstructions are obtained if a certain amount of smoothing is included with the convolution in (122). If $k(na)$ is the impulse response of the smoothing filter, we can write

$$Q_{\beta_i}(na) = R_{\beta_i}(na) * g(na) * k(na). \tag{125}$$

In a frequency domain implementation this smoothing may be achieved by a simple multiplicative window such as a Hamming window.

Step 3:

Perform a *weighted* backprojection of each filtered projection along the corresponding fan. The sum of all the backprojections is the reconstructed image

$$f(x, y) = \Delta B \sum_{i=1}^{M} \frac{1}{U^2(x, y, \beta_i)} Q_{\beta_i}(s') \tag{126}$$

where U is computed using (106) and s' identifies the ray that passes through (x, y) in the fan for the source located at angle β_i. Of course, this value of s' may not correspond to one of the values of na at which Q_{β_i} is known. In that case interpolation is necessary.

3.4.3 A Re-sorting Algorithm

We will now describe an algorithm that rapidly re-sorts the fan beam projection data into equivalent parallel beam projection data. After re-sorting one may use the filtered backprojection algorithm for parallel projection data to reconstruct the image. This fast re-sorting algorithm does place constraints on the angles at which the fan beam projections must be taken and also on the angles at which projection data must be sampled within each fan beam projection.

Referring to Fig. 3.19, the relationships between the independent variables of the fan beam projections and parallel projections are given by (70):

$$t = D \sin \gamma \quad \text{and} \quad \theta = \beta + \gamma. \tag{127}$$

If, as before, $R_\beta(\gamma)$ denotes a fan beam projection taken at angle β, and $P_\theta(t)$ a parallel projection taken at angle θ, using (127) we can write

$$R_\beta(\gamma) = P_{\beta+\gamma}(D \sin \gamma). \tag{128}$$

Let $\Delta \beta$ denote the angular increment between successive fan beam projections, and let $\Delta \gamma$ denote the angular interval used for sampling the fan

beam projections. We will assume that the following condition is satisfied:

$$\Delta\beta = \Delta\gamma = \alpha. \tag{129}$$

Clearly then β and γ in (128) are equal to $m\alpha$ and $n\alpha$, respectively, for some integer values of the indices m and n. We may therefore write (128) as

$$R_{m\alpha}(n\alpha) = P_{(m+n)\alpha}(D \sin n\alpha). \tag{130}$$

This equation serves as the basis of a fast re-sorting algorithm. It expresses the fact that the nth ray in the mth radial projection is the nth ray in the $(m + n)$th parallel projection. Of course, because of the $\sin n\alpha$ factor on the right-hand side of (130), the parallel projections obtained are not uniformly sampled. This can usually be rectified by interpolation.

3.5 Fan Beam Reconstruction from a Limited Number of Views

Simple geometrical arguments should convince the reader that parallel projections that are 180° apart, $P_\theta(t)$ and $P_{\theta+180^\circ}(t)$, are mirror images of each other. That is,

$$P_\theta(t) = P_{\theta+180^\circ}(-t) \tag{131}$$

and thus it is only necessary to measure the projections of an object for angles from 0 to 180°.

We can extend this result by noting that an object is completely specified if the ray integrals of the object are known for

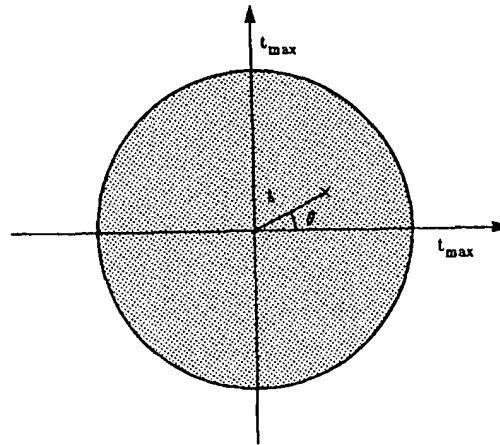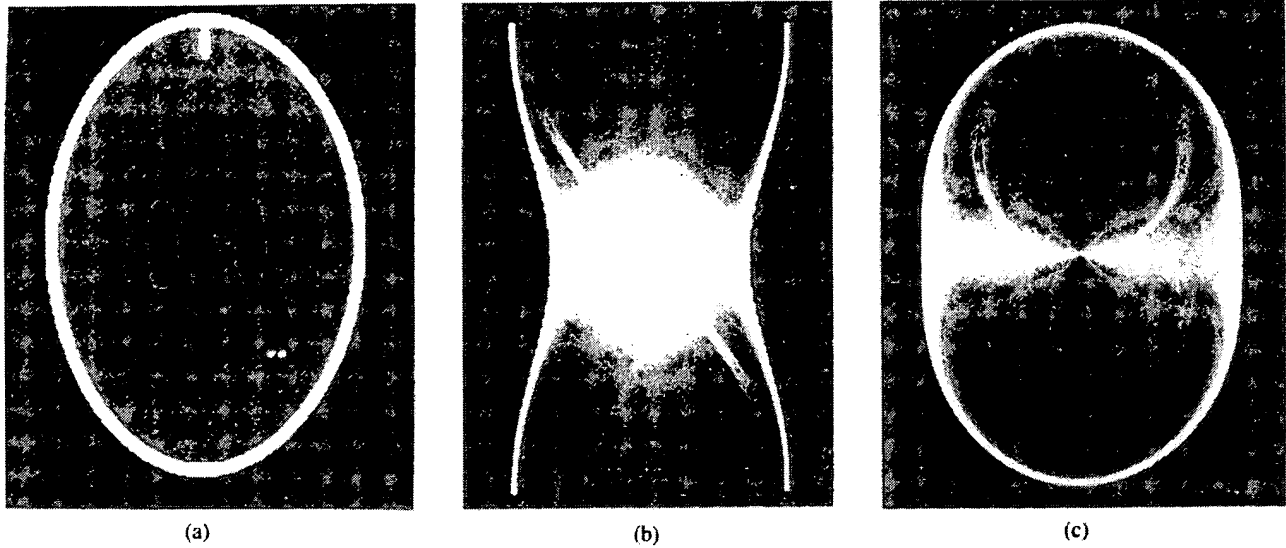$$\theta_0 \leq \theta < \theta_0 + 180^\circ \tag{132}$$

and

$$-t_{\max} \leq t \leq t_{\max} \tag{133}$$

where $t_{\max}$ is large enough so that each projection is at least as wide as the object at its widest. If each ray integral is represented as a point in a polar coordinate system (t, θ) as shown in Fig. 3.25 then a complete set of ray

(a)   (b)   (c)

Fig. 3.26: *An object and its Radon transform are shown here. The object in (a) is used to illustrate the short scan algorithm developed by Parker [Par82a]. (b) shows the Radon transform in rectangular coordinates, while (c) represents the Radon transform in polar coordinates. (Reprinted with permission from [Par82a], [Par82b].)*

integrals will completely fill a disk of radius t_{max}. This is commonly known as the Radon transform or a sinogram and is shown for the Shepp and Logan phantom both in polar and rectangular coordinates in Fig. 3.26.

These ideas can also be extended to the fan beam case. From Fig. 3.27 we see that two ray integrals represented by the fan beam angles (β_1, γ_1) and (β_2, γ_2) are identical provided

$$\beta_1 - \gamma_1 = \beta_2 - \gamma_2 + 180° \tag{134}$$

and

$$\gamma_1 = -\gamma_2. \tag{135}$$

With fan beam data the coordinate transformation

$$t = D \sin \gamma$$

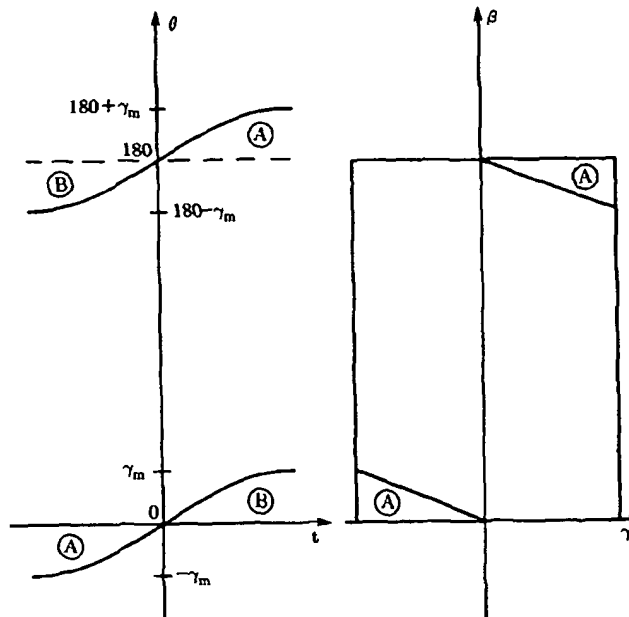$$\theta = \beta + \gamma \tag{136}$$

maps the (β, γ) description of a ray in a fan into its Radon transform equivalent. This transformation can then be used to construct Fig. 3.27, which shows the data available in Radon domain as the projection angle β varies between 0 and 180° with a fan angle of 40° $(\gamma_{max} = 20°)$.
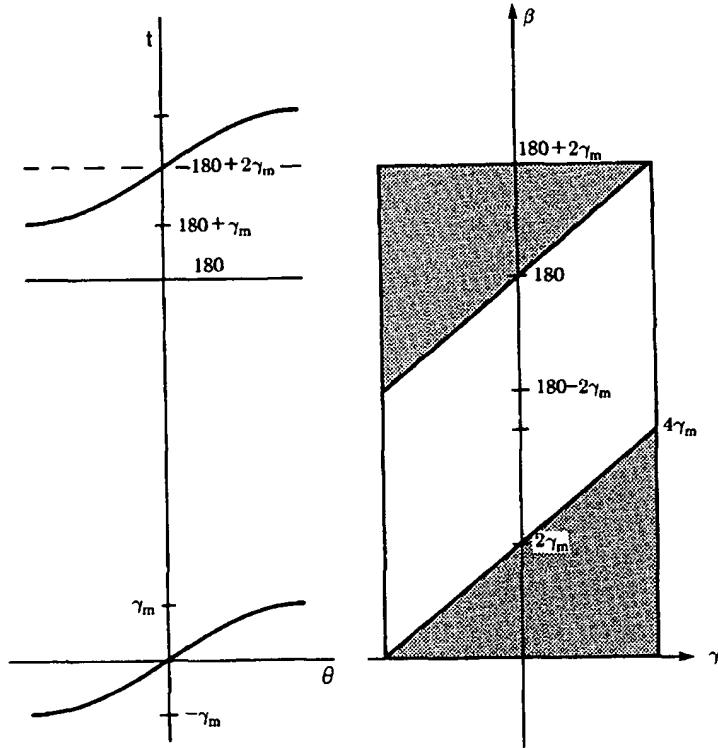
Recall that points in Radon space that are periodic with respect to the intervals shown in (132) and (133) represent the same ray integral. Thus the data in Fig. 3.28 for angles $\theta > 180°$ and $t > 0$ are equal to the Radon data for $\theta < 0$ and $t < 0$. These two regions are labeled A in Fig. 3.28. On the other hand, the regions marked B in Fig. 3.28 are areas in the Radon space where there are no measurements of the object. To cover these areas it is necessary to measure projections over an additional $2\gamma_m$ degrees as shown in
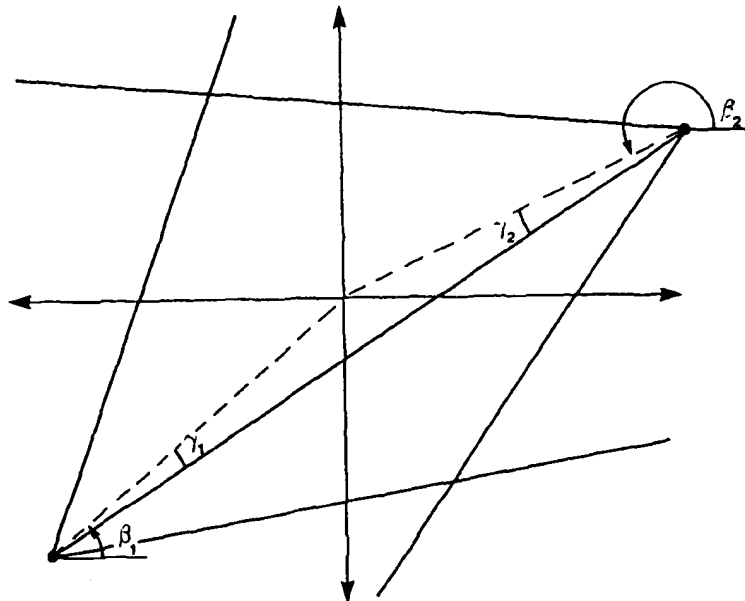
Fig. 3.27: *Rays in two fan beams will represent the same line integral if they satisfy the relationship* $\beta_1 - \gamma_1 = \beta_2 - \gamma_2 + 180°$.

Fig. 3.28: *Collecting projections over 180° gives estimates of the Radon transform between the curved lines as shown on the left. The curved lines represent the most extreme projections for a fan angle of* γ_m. *On the right is shown the available data in the* β-γ *coordinate system used in describing fan beams. In both cases the region marked A represents the part of the Radon transform where two estimates are available. On the other hand, for 180° of projections there are no estimates of the Radon transform in the regions marked B.*

Fig. 3.29. Thus it should be possible to reconstruct an object using fan beam projections collected over 180 + $2\gamma_m$ degrees.

Fig. 3.30 shows a "perfect" reconstruction of a phantom used by Parker [Par82a], [Par82b] to illustrate his algorithm for short scan or "180 degree plus" reconstructions. Projection data measured over a full 360° of β were used to generate the reconstruction.

It is more natural to discuss the projection data overlap in the (β, γ) coordinate system. We derive the overlap region in this space by using the relations in (134) and (135) and the limits

$$0 \le \beta_1 \le 180° + 2\gamma_m$$

$$0 \le \beta_2 \le 180° + 2\gamma_m. \tag{137}$$
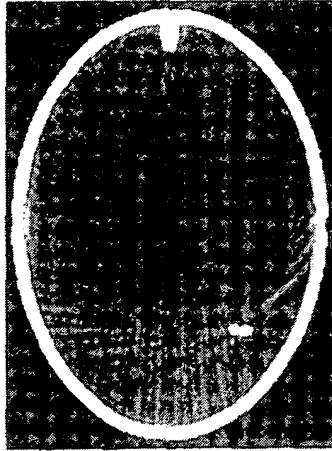
Substituting (134) and (135) into the first equation above we find

$$0 \le \beta_2 - 2\gamma_2 + 180° \le 180° + 2\gamma_m \tag{138}$$

and then by rearranging

$$-180° + 2\gamma_2 \le \beta_2 \le 2\gamma_m - 2\gamma_2. \tag{139}$$

Substituting the same two equations into the second inequality in (137) we find

$$0 \le \beta_1 - 2\gamma_1 - 180° \le 180° + 2\gamma_m \tag{140}$$

Fig. 3.30: *This figure shows a reconstruction using 360° of fan beam projections and a standard filtered backprojection algorithm. (Reprinted with permission from [Par82a], [Par82b].)*

and then by rearranging

$$180° + 2\gamma_1 \leq \beta_1 \leq 360° + 2\gamma_m + 2\gamma_1. \tag{141}$$

Since the fan beam angle, γ, is always less then $90°$, the overlapping regions are given by

$$0 \leq \beta_2 \leq 2\gamma_m + 2\gamma_2 \tag{142}$$

Fig. 3.31: *This reconstruction was generated with a standard filtered backprojection algorithm using 220° of projections. The large artifacts are due to the lack of data in some regions of the Radon transform and duplicate data in others. (Reprinted with permission from [Par82a], [Par82b].)*

and

$$180° + 2\gamma_1 \leq \beta_1 \leq 180° + 2\gamma_m \tag{143}$$

as is shown in Fig. 3.29.

If projections are gathered over an angle of $180° + 2\gamma_m$ and a reconstruction is generated using the standard fan beam reconstruction algorithms described in Section 3.4, then the image in Fig. 3.31 is obtained.

In this case a fan angle of 40° ($\gamma_{max} = 20$) was used. As described above, the severe artifacts in this reconstruction are caused by the double coverage of the points in region B of Fig. 3.28.

One might think that the reconstruction can be improved by setting the data to zero in one of the regions of overlap. This can be implemented by multiplying a projection at angle β, $p_\beta(\gamma)$, by a one-zero window, $w_\beta(\gamma)$, given by

$$w_\beta(\gamma) = \begin{cases} 0 & 0 \le \beta \le 2\gamma_m + 2\gamma \\ 1 & \text{elsewhere.} \end{cases} \tag{144}$$

As shown by Naparstek [Nap80] using this type of window gives only a small improvement since streaks obscure the resulting image.

While the above filter function properly handles the extra data, better reconstructions can be obtained using a window described in [Par82a]. The sharp cutoff of the one-zero window adds a large high frequency component to each projection which is then enhanced by the $|\omega|$ filter that is used to filter each projection.

More accurate reconstructions are obtained if a "smoother" window is used to filter the data. Mathematically, a "smooth" window is both continuous and has a continuous derivative. Formally, the window, $w_\beta(\gamma)$, must satisfy the following condition:

$$w_{\beta_1}(\gamma_1) + w_{\beta_2}(\gamma_2) = 1 \tag{145}$$

for (β_1, γ_1) and (β_2, γ_2) satisfying the relations in (134) and (135), and

$$w_0(\gamma) = 0 \tag{146}$$

and

$$w_{180° + 2\gamma_m} = 0. \tag{147}$$

To keep the filter function continuous and "smooth" at the boundary between the single and double overlap regions the following constraints are imposed on the derivative of $w_\beta(\gamma)$:

$$\left. \frac{\partial w_\beta(\gamma)}{\partial \beta} \right|_{\beta = 2\gamma_m + 2\gamma} = 0 \tag{148}$$

and

$$\left. \frac{\partial w_\beta(\gamma)}{\partial \beta} \right|_{\beta = 180° + 2\gamma} = 0. \tag{149}$$
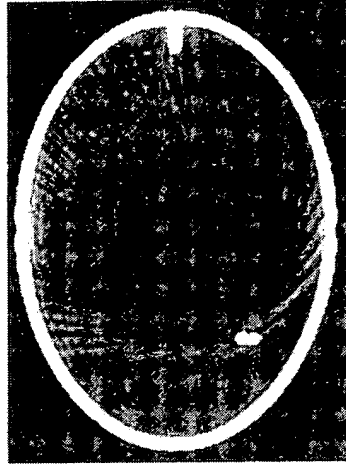
Fig. 3.32: *Using a weighting function that minimizes the discontinuities in the projection this reconstruction is obtained using 220° of projection data. (Reprinted with permission from [Par82a], [Par82b].)*

One such window that satisfies all of these conditions is

$$
w_\beta(\gamma) = \begin{cases}
\sin^2\left[\dfrac{45°\beta}{\gamma_m - \gamma}\right], & 0 \le \beta \le 2\gamma_m - 2\gamma \\[2em]
1, & 2\gamma_m - 2\gamma \le \beta \le 180° - 2\gamma \\[2em]
\sin^2\left[45° \dfrac{180° + 2\gamma_m - \beta}{\gamma + \gamma_m}\right], & 180° - 2\gamma \le \beta \le 180° + 2\gamma_m.
\end{cases}
$$

(150)

A reconstruction using this weighting function is shown in Fig. 3.32. From this image we see that it is possible to eliminate the overlap without introducing errors by using a smooth window.

3.6 Three-Dimensional Reconstructions[1]

The conventional way to image a three-dimensional object is to illuminate the object with a narrow beam of x-rays and use a two-dimensional reconstruction algorithm. A three-dimensional reconstruction can then be formed by illuminating successive planes within the object and stacking the resulting reconstructions. This is shown in Fig. 3.33.

A more efficient approach, to be considered in this section, is a generalization of the two-dimensional fan beam algorithms presented in Section 3.4.2. Now, instead of illuminating a slice of the object with a fan of x-rays, the entire object is illuminated with a point source and the x-ray flux is measured on a plane. This is called a cone beam reconstruction because the

[1] We are grateful for the help of Barry Roberts in the preparation of this material.

object

reconstructed slices
of the object
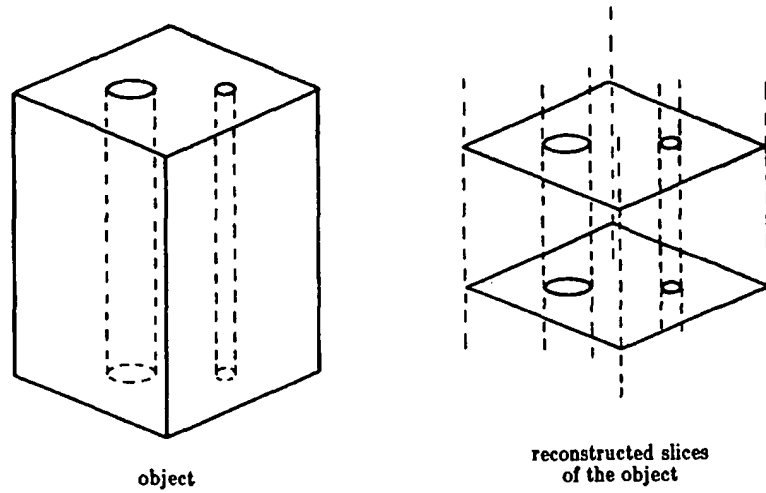
Fig. 3.33: *A three-dimensional reconstruction can be done by repetitively using two-dimensional reconstruction algorithms at different heights along the z-axis. (From [Kak86].)*

rays form a cone as illustrated in Fig. 3.34. Cone beam algorithms have been studied for use with Mayo Clinic's Digital Spatial Reconstructor (DSR) [Rob83] and Imatron's Fifth Generation Scanner [Boy83].

The main advantage of cone beam algorithms is the reduction in data collection time. With a single source, ray integrals are measured through every point in the object in the time it takes to measure a single slice in a conventional two-dimensional scanner. The projection data, $R_\beta(t, r)$, are now a function of the source angle, β, and horizontal and vertical positions on the detector plane, t and r.

3.6.1 Three-Dimensional Projections

A ray in a three-dimensional projection is described by the intersection of two planes

$$t = x \cos \theta + y \sin \theta \qquad (151)$$

$$r = -(-x \sin \theta + y \cos \theta) \sin \gamma + z \cos \gamma. \qquad (152)$$

A new coordinate system (t, s, r) is obtained by two rotations of the (x, y, z)-axis as shown in Fig. 3.35. The first rotation, as in the two-dimensional case, is by θ degrees around the z-axis to give the (t, s, z)-axes. Then a second rotation is done out of the (t, s)-plane around the t-axis by an angle of γ. In matrix form the required rotations are given by

$$\begin{bmatrix} t \\ s' \\ r \end{bmatrix} = \begin{bmatrix} 1 & 0 & 0 \\ 0 & \cos \gamma & \sin \gamma \\ 0 & -\sin \gamma & \cos \gamma \end{bmatrix} \begin{bmatrix} \cos \theta & \sin \theta & 0 \\ -\sin \theta & \cos \theta & 0 \\ 0 & 0 & 1 \end{bmatrix} \begin{bmatrix} x \\ y \\ z \end{bmatrix} . \qquad (153)$$

A three-dimensional parallel projection of the object f is expressed by the

Source

Detection
plane

R_β(t,r)
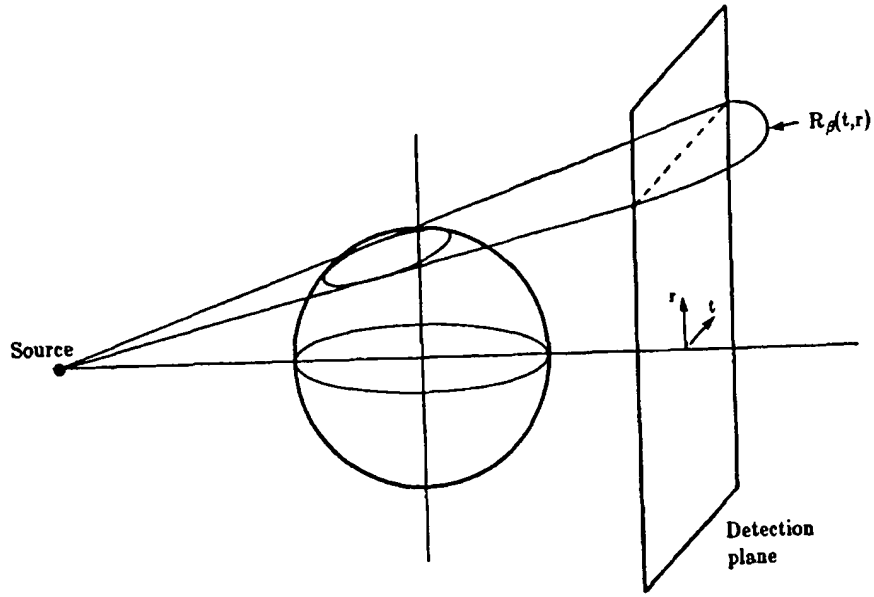
Fig. 3.34: *In cone beam projections the detector measures the x-ray flux over a plane. By rotating the source and detector plane completely around the object all the data necessary for a three-dimensional reconstruction can be gathered in the time a conventional fan beam system collects the data for its two-dimensional reconstruction. (From [Kak86].)*

following integral:

$$P_{\theta,\gamma}(t, r) = \int_{-S_m}^{S_m} f(t, s, r) \, ds. \tag{154}$$

Note that four variables are being used to specify the desired ray; (t, θ) specify the distance and angle in the x-y plane and (r, γ) in the s-z plane.

In a cone beam system the source is rotated by β and ray integrals are measured on the detector plane as described by $R_\beta(p', \zeta')$. To find the equivalent parallel projection ray first define

$$p = \frac{p' D_{SO}}{D_{SO} + D_{DE}} \qquad \zeta = \frac{\zeta' D_{SO}}{D_{SO} + D_{DE}} \tag{155}$$

as was done in Section 3.4.2. Here we have used D_{SO} to indicate the distance from the center of rotation to the source and D_{DE} to indicate the distance from the center of rotation to the detector. For a given cone beam ray, $R_\beta(p, \zeta)$, the parallel projection ray is given by

$$t = p \frac{D_{SO}}{\sqrt{D_{SO}^2 + p^2}} \tag{156}$$

$$\theta = \beta + \tan^{-1}(p/D_{SO}) \tag{157}$$

where t and θ locate a ray in a given tilted fan, and similarly

$$r = \zeta \frac{D_{SO}}{\sqrt{D_{SO}^2 + \zeta^2}} \tag{158}$$
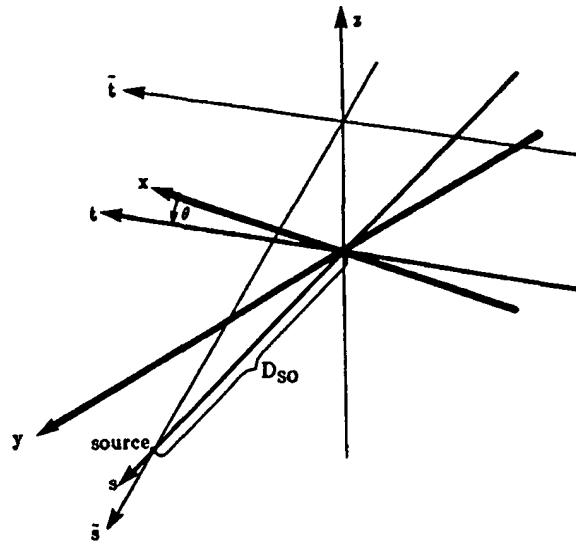
Fig. 3.35: *To simplify the discussion of the cone beam reconstruction the coordinate system is rotated by the angle of the source to give the (s, t)-axis. The r-axis is not shown but is perpendicular to the t- and s-axes. (From [Kak86].)*

$$\gamma = \tan^{-1} \left(\zeta / D_{so} \right). \tag{159}$$

were r and γ specify the location of the tilted fan itself.

The reconstructions shown in this section will use a three-dimensional version of the Shepp and Logan head phantom. The two-dimensional ellipses of Table 3.1 have been made ellipsoids and repositioned within an imaginary skull. Table 3.2 shows the position and size of each ellipse and Fig. 3.36 illustrates their position.

Because of the linearity of the Radon transform, a projection of an object consisting of ellipsoids is just the sum of the projection of each individual

Table 3.2: Summary of parameters for three-dimensional tomography simulations.

Ellipsoid	Coordinates of the Center (x, y, z)	Axis Lengths (A, B, C)	Rotation Angle β (deg)	Gray Level ρ
a	(0, 0, 0)	(0.69, 0.92, 0.9)	0	2.0
b	(0, 0, 0)	(0.6624, 0.874, 0.88)	0	−0.98
c	(−0.22, 0, −0.25)	(0.41, 0.16, 0.21)	108	−0.02
d	(0.22, 0, −0.25)	(0.31, 0.11, 0.22)	72	−0.02
e	(0, 0.1, −0.25)	(0.046, 0.046, 0.046)	0	0.02
f	(0, 0.1, −0.25)	(0.046, 0.046, 0.046)	0	0.02
g	(−0.8, −0.65, −0.25)	(0.046, 0.023, 0.02)	0	0.01
h	(0.06, −0.065, −0.25)	(0.046, 0.023, 0.02)	90	0.01
i	(0.06, −0.105, 0.625)	(0.56, 0.04, 0.1)	90	0.02
j	(0, 0.1, −0.625)	(0.056, 0.056, 0.1)	0	−0.02

(a)

(b)

(c)
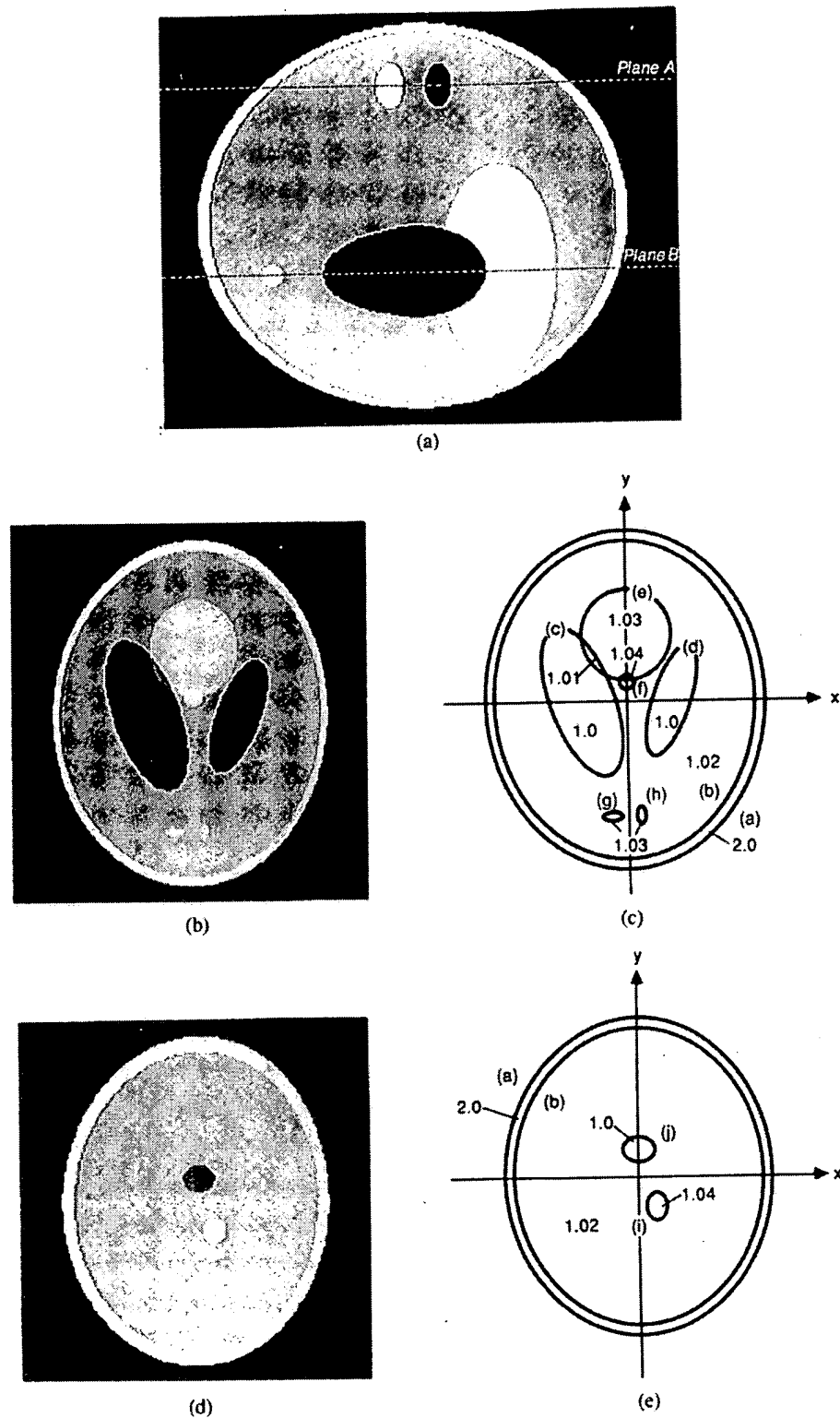
Fig. 3.36: *A three-dimensional version of the Shepp and Logan head phantom is used to test the cone beam reconstruction algorithms in this section. (a) A vertical slice through the object illustrating the position of the two reconstructed planes. (b) An image at plane B ($z = -0.25$) and (c) an illustration of the level of each of the ellipses. (d) An image at plane A ($z = 0.625$) and (e) an illustration of the gray levels with the slice. (From [Kak86].)*

(d)

(e)

ellipsoid. If the ellipsoid is constant and described by

$$f(x, y, z) = \begin{cases} \rho & \dfrac{x^2}{A^2} + \dfrac{y^2}{B^2} + \dfrac{z^2}{C^2} \leq 1 \\ 0 & \text{otherwise} \end{cases} \tag{160}$$

then its projection on the detector plane is written

$$P_{\theta,\gamma}(t, r) = \frac{2\rho ABC}{a^2(\theta,\gamma)} \left[a^2(\theta, \gamma) - t^2(C^2 \cos^2 \gamma + (B^2 \cos^2 \theta + A^2 \sin^2 \theta) \sin^2 \gamma) \right.$$

$$- r^2(A^2 \cos^2 \theta + B^2 \sin^2 \theta)\left(\frac{7 + \cos (4\gamma)}{8}\right)$$

$$\left. - 2tr \sin \gamma \cos \theta \sin \theta (B^2 - A^2) \right]^{1/2} \tag{161}$$

where

$$a^2(\theta, \gamma) = C^2(B^2 \sin^2 \theta + A^2 \cos^2 \theta) \cos^2 \gamma + A^2 B^2 \sin^2 \gamma. \tag{162}$$

If the tilt angle, γ, is zero then (161) simplifies to (5).

3.6.2 Three-Dimensional Filtered Backprojection

We will present a filtered backprojection algorithm based on analyses presented in [Fel84] and [Kak86]. The reconstruction is based on filtering and backprojecting a single plane within the cone. In other words, each elevation in the cone (described by z or ζ) is considered separately and the final three-dimensional reconstruction is obtained by summing the contribution to the object from all the tilted fan beams.

The cone beam algorithm sketched above is best derived by starting with the filtered backprojection algorithm for equispatial rays. In a three-dimensional reconstruction each fan is angled out of the source–detector plane of rotation. This leads to a change of variables in the backprojection algorithm.

First consider the two-dimensional fan beam reconstruction formula for the point (r, ϕ):

$$g(r, \phi) = \frac{1}{2} \int_0^{2\pi} \frac{1}{U^2} \int_{-\infty}^{\infty} R_\beta(p) h(p' - p) \frac{D_{SO}}{\sqrt{D_{SO}^2 + p^2}} \, dp \, d\beta \tag{163}$$

$$p' = \frac{D_{SO} r \cos (\beta - \phi)}{D_{SO} + r \sin (\beta - \phi)} \qquad h(p) = \int_{-W}^{W} |\omega| e^{j\omega p} \, d\omega \tag{164}$$

$$U(r, \phi, \beta) = \frac{D_{SO} + r \sin (\beta - \phi)}{D_{SO}}. \tag{165}$$

Equation (163) is the same as (116), except that we have now used different names for some of the variables. To further simplify this expression we will replace the (r, ϕ) coordinate system by the rotated coordinates (t, s). Recall that (t, s) is the location of a point rotated by the angular displacement of the source–detector array. The expressions

$$t = x \cos \beta + y \sin \beta \qquad s = -x \sin \beta + y \cos \beta \qquad (166)$$

$$x = r \cos \phi \qquad y = r \sin \phi, \qquad (167)$$

lead to

$$p' = \frac{D_{SO}t}{D_{SO} - s} \qquad U(x, y, \beta) = \frac{D_{SO} - s}{D_{SO}}. \qquad (168)$$

The fan beam reconstruction algorithm is now written as

$$g(t, s) = \frac{1}{2} \int_0^{2\pi} \frac{D_{SO}^2}{(D_{SO} - s)^2} \int_{-\infty}^{\infty} R_\beta(p) h \left(\frac{D_{SO}t}{D_{SO} - s} - p \right) \frac{D_{SO}}{\sqrt{D_{SO}^2 + p^2}} \, dp \, d\beta. \qquad (169)$$

In a cone beam reconstruction it is necessary to tilt the fan out of the plane of rotation; thus the size of the fan and the coordinate system of the reconstructed point change. As shown in Fig. 3.37 a new coordinate system $(\tilde{t}, \tilde{s})$ is defined that represents the location of the reconstructed point with respect to the tilted fan. Because of the changing fan size both the source distance, D_{SO}, and the angular differential, β, change. The new source distance is given by

Fig. 3.37: *The $(\tilde{t}, \tilde{s})$ coordinate system represents a point in the object with respect to a tilted fan beam. (From [Kak86].)*
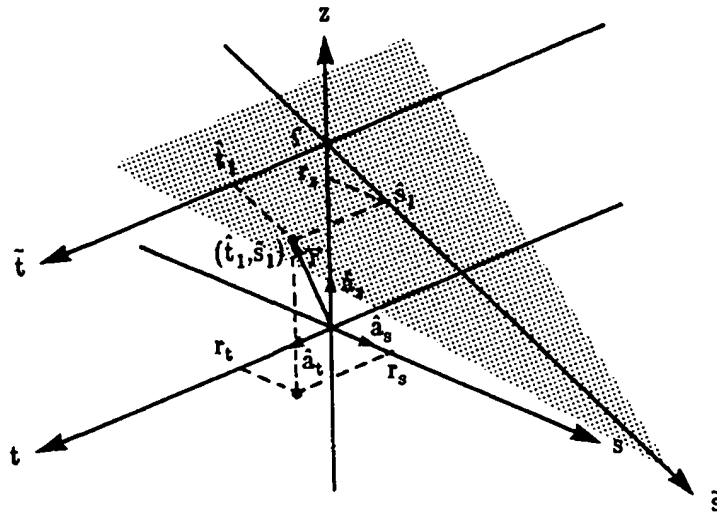
$$D'^2_{SO} = D_{SO}^2 + \zeta^2 \qquad (170)$$

where ζ is the height of the fan above the center of the plane of rotation. In addition, the increment of angular rotation $d\beta'$ becomes

$$D_{SO}\, d\beta = D'_{SO}\, d\beta' \qquad d\beta' = \frac{d\beta\, D_{SO}}{\sqrt{D^2_{SO}+\zeta^2}}\,. \tag{171}$$

Substituting these new variables, D'_{SO} for D_{SO} and $d\beta'$ for $d\beta$, and writing the projection data as $R_{\beta'}(p,\ \zeta)$, (169) becomes

$$g(\tilde{t},\ \tilde{s}) = \frac{1}{2}\int_0^{2\pi} \frac{D'^2_{SO}}{(D'_{SO}-\tilde{s})^2}$$

$$\cdot \int_{-\infty}^{\infty} R_{\beta'}(p,\ \zeta)h\left(\frac{D'_{SO}\tilde{t}}{D'_{SO}-\tilde{s}}-p\right)\frac{D'_{SO}}{\sqrt{D'^2_{SO}+p^2}}\,dp\,d\beta'\,. \tag{172}$$

To return the reconstruction to the original $(t,\ s,\ z)$ coordinate system we substitute

$$\tilde{t}=t, \qquad \frac{\tilde{s}}{D'_{SO}}=\frac{s}{D_{SO}}\,, \qquad \frac{\zeta}{D_{SO}}=\frac{z}{D_{SO}-s} \tag{173}$$

and (170) and (171) to find

$$g(t,\ s) = \frac{1}{2}\int_0^{2\pi} \frac{D^2_{SO}}{(D_{SO}-s)^2}$$

$$\cdot \int_{-\infty}^{\infty} R_{\beta}(p,\ \zeta)h\left(\frac{D_{SO}t}{D_{SO}-s}-p\right)\frac{D_{SO}}{\sqrt{D^2_{SO}+\zeta^2+p^2}}\,dp\,d\beta. \tag{174}$$

The cone beam reconstruction algorithm can be broken into the following three steps:

Step 1:

Multiply the projection data, $R_{\beta}(p,\ \zeta)$, by the function $(D_{SO}/\sqrt{D^2_{SO}+\zeta^2+p^2})$ to find $R'_{\beta}(p,\ \zeta)$:

$$R'_{\beta}(p,\ \zeta) = \frac{D_{SO}}{\sqrt{D^2_{SO}+\zeta^2+p^2}}\, R_{\beta}(p,\ \zeta). \tag{175}$$

Step 2:

Convolve the weighted projection $R'_{\beta}(p,\ \zeta)$ with $h(p)/2$ by multiplying their Fourier transforms with respect to p. Note this convolution is done independently for each elevation, ζ. The result, $Q_{\beta}(p,\ \zeta)$, is written

$$Q_{\beta}(p,\ \zeta) = R'_{\beta}(p,\ \zeta) * \frac{1}{2}\, h(p). \tag{176}$$

Step 3:

Finally, each weighted projection is backprojected over the three-

dimensional reconstruction grid:

$$g(t, s, z) = \int_0^{2\pi} \frac{D_{SO}^2}{(D_{SO} - s)^2} Q_\beta \left(\frac{D_{SO}t}{D_{SO} - s}, \frac{D_{SO}z}{D_{SO} - s} \right) d\beta. \quad (177)$$

The two arguments of the weighted projection, Q_β, represent the transformation of a point in the object into the coordinate system of the tilted fan shown in Fig. 3.37.

Only those points of the object that are illuminated from all directions can be properly reconstructed. In a cone beam system this region is a sphere of radius $D_{SO} \sin (\Gamma_m)$ where Γ_m is half the beamwidth angle of the cone. Outside this region a point will not be included in some of the projections and thus will not be correctly reconstructed.

Figs. 3.38 and 3.39 show reconstructions at two different levels of the object described in Fig. 3.36. In each case 100 projections of 127 × 127 elements were simulated and both a gray scale image of the entire plane and a line plot are shown. The reconstructed planes were at $z = 0.625$ and $z = -0.25$ planes and are marked as Plane A and Plane B in Fig. 3.36.

In agreement with [Smi85], the quality of the reconstruction varies with the elevation of the plane. On the plane of rotation ($z = 0$) the cone beam algorithm is identical to a equispatial fan beam algorithm and thus the results shown in Fig. 3.38 are quite good. Farther from the central plane each point in the reconstruction is irradiated from all directions but now at an oblique angle. As shown in Fig. 3.39 there is a noticeable degradation in the reconstruction.

3.7 Bibliographic Notes

The current excitement in tomographic imaging originated with Hounsfield's invention [Hou72] of the computed tomography (CT) scanner in 1972, which was indeed a major breakthrough. His invention showed that it is possible to get high-quality cross-sectional images with an accuracy now reaching one part in a thousand in spite of the fact that the projection data do not strictly satisfy theoretical models underlying the efficiently implementable reconstruction algorithms. (In x-ray tomography, the mismatch with the assumed theoretical models is caused primarily by the polychromaticity of the radiation used. This will be discussed in Chapter 4.) His invention also showed that it is possible to process a very large number of measurements (now approaching a million) with fairly complex mathematical operations, and still get an image that is incredibly accurate. The success of x-ray CT has naturally led to research aimed at extending this mode of image formation to ultrasound and microwave sources.

The idea of filtered backprojection was first advanced by Bracewell and Riddle [Bra67] and later independently by Ramachandran and Lakshminarayanan [Ram71]. The superiority of the filtered backprojection algorithm over
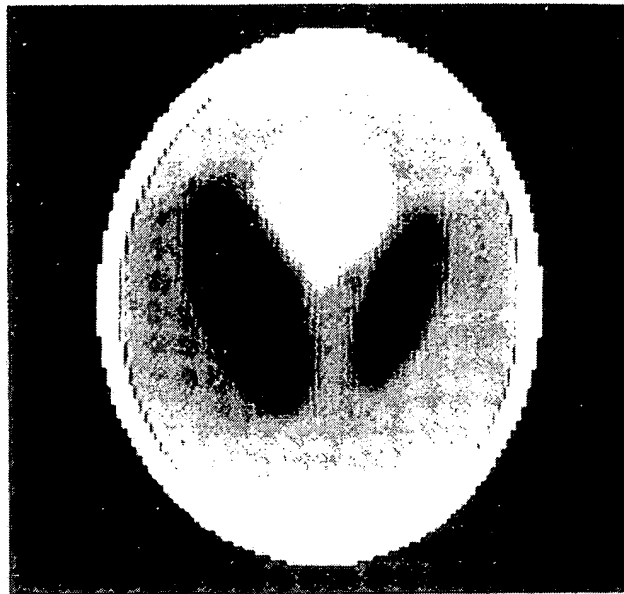
(a)
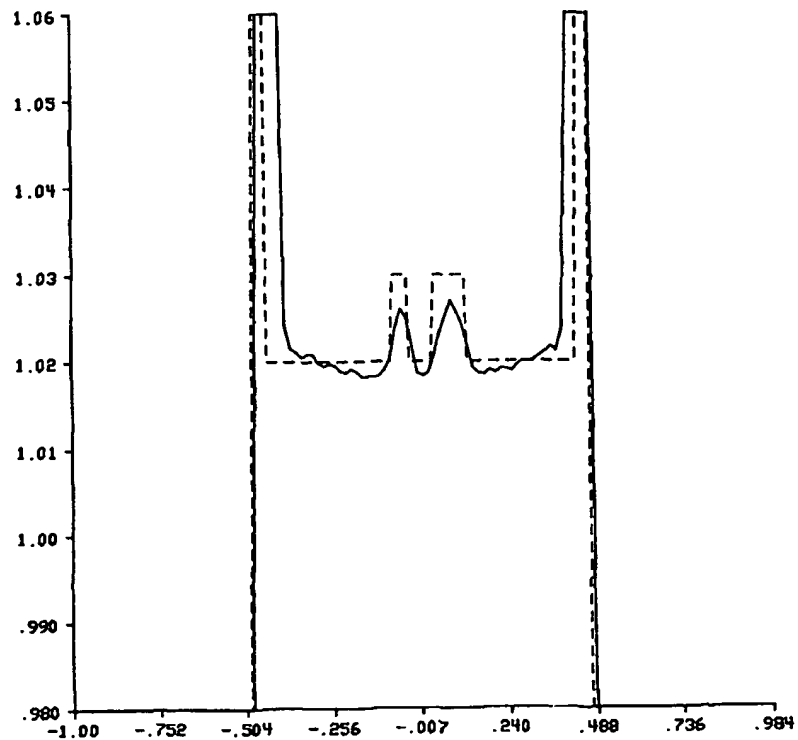
(b)

Fig. 3.38: *(a) Cone beam algorithm reconstruction of plane B in Fig. 3.36. (b) Plot of the y = −0.605 line in the reconstruction compared to the original. (From [Kak86].)*

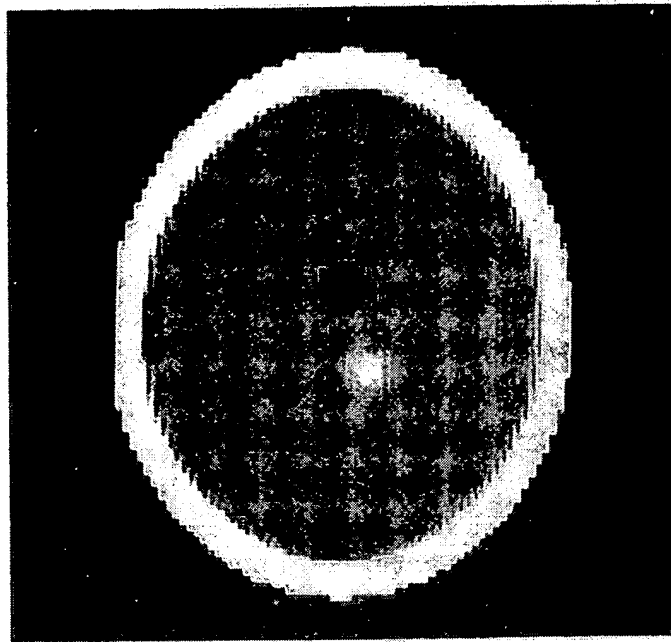(a)
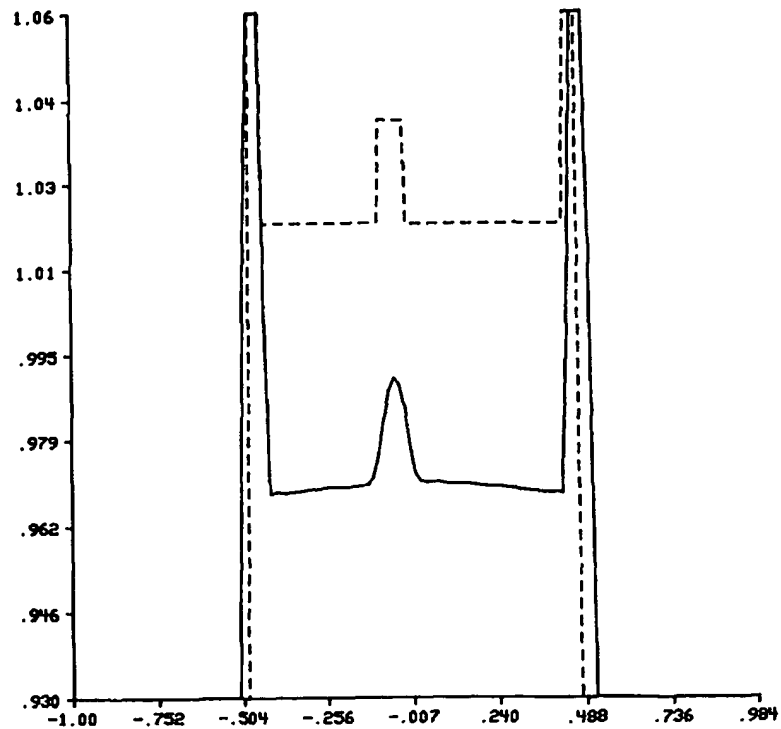

(b)

Fig. 3.39: *(a) Cone beam algorithm reconstruction of plane A in Fig. 3.36. (b) Plot of the y = −0.105 line in the reconstruction compared to the original. (From [Kak86].)*

the algebraic techniques was first demonstrated by Shepp and Logan [She74]. Its development for fan beam data was first made by Lakshminarayanan [Lak75] for the equispaced collinear detectors case and later extended by Herman and Naparstek [Her77] for the case of equiangular rays. The fan beam algorithm derivation presented here was first developed by Scudder [Scu78]. Many authors [Bab77], [Ken79], [Kwo77], [Lew79], [Tan75] have proposed variations on the filter functions of the filtered backprojection algorithms discussed in this chapter. The reader is referred particularly to [Ken79], [Lew79] for ways to speed up the filtering of the projection data by using binary approximations and/or inserting zeros in the unit sample response of the filter function. Images may also be reconstructed from fan beam data by first sorting them into parallel projection data. Fast algorithms for ray sorting of fan beam data have been developed by Wang [Wan77], Dreike and Boyd [Dre77], Peters and Lewitt [Pet77], and Dines and Kak [Din76]. The reader is referred to [Nah81] for a filtered backprojection algorithm for reconstructions from data generated by using very narrow angle fan beams that rotate *and* traverse *continuously* around the object. The reader is also referred to [Hor78], [Hor79] for algorithms for nonuniformly sampled projection data, and to [Bra67], [Lew78], [Opp75], [Sat80], [Tam81] for reconstructions from incomplete and limited projections. Full three-dimensional reconstructions have been discussed in [Chi79], [Chi80], [Smi85]. We have also not discussed the circular harmonic transform method of image reconstruction as proposed by Hansen [Han81a], [Han81b].

Tomographic imaging may also be accomplished, although less accurately, by direct Fourier inversion, instead of the filtered backprojection method presented in this chapter. This was first shown by Bracewell [Bra56] for radioastronomy, and later independently by DeRosier and Klug [DeR68] in electron microscopy and Rowley [Row69] in optical holography. Several workers who applied this method to radiography include Tretiak *et al.* [Tre69], Bates and Peters [Bat71], and Mersereau and Oppenheim [Mer74]. In order to utilize two-dimensional FFT algorithms for image formation, the direct Fourier approach calls for frequency domain interpolation from a polar grid to a rectangular grid. For some recent methods to minimize the resulting interpolation error, the reader is referred to [Sta81]. Recently Wernecke and D'Addario [Wer77] have proposed a maximum-entropy approach to direct Fourier inversion. Their procedure is especially applicable if for some reason the projection data are insufficient.

3.8 References

[Bab77]   N. Baba and K. Murata, "Filtering for image reconstruction from projections," *J. Opt. Soc. Amer.*, vol. 67, pp. 662–668, 1977.

[Bat71]   R. H. T. Bates and T. M. Peters, "Towards improvements in tomography," *New Zealand J. Sci.*, vol. 14, pp. 883–896, 1971.

[Boy83]   D. P. Boyd and M. J. Lipton, "Cardiac computed tomography," *Proc. IEEE*, vol. 71, pp. 298–307, Mar. 1983.

[Bra56]   R. N. Bracewell, "Strip integration in radio astronomy," *Aust. J. Phys.*, vol. 9, pp. 198-217, 1956.

[Bra67]   R. N. Bracewell and A. C. Riddle, "Inversion of fan-beam scans in radio astronomy," *Astrophys. J.*, vol. 150, pp. 427-434, Nov. 1967.

[Chi79]   M. Y. Chiu, H. H. Barrett, R. G. Simpson, C. Chou, J. W. Arendt, and G. R. Gindi, "Three dimensional radiographic imaging with a restricted view angle," *J. Opt. Soc. Amer.*, vol. 69, pp. 1323-1330, Oct. 1979.

[Chi80]   M. Y. Chiu, H. H. Barrett, and R. G. Simpson, "Three dimensional reconstruction from planar projections," *J. Opt. Soc. Amer.*, vol. 70, pp. 755-762, July 1980.

[Cro70]   R. A. Crowther, D. J. DeRosier, and A. Klug, "The reconstruction of a three-dimensional structure from projections and its applications to electron microscopy," *Proc. Roy. Soc. London*, vol. A317, pp. 319-340, 1970.

[DeR68]   D. J. DeRosier and A. Klug, "Reconstruction of three dimensional structures from electron micrographs," *Nature*, vol. 217, pp. 130-134, Jan. 1968.

[Din76]   K. A. Dines and A. C. Kak, "Measurement and reconstruction of ultrasonic parameters for diagnostic imaging," Research Rep. TR-EE 77-4, School of Electrical Engineering, Purdue Univ., Lafayette, IN, Dec. 1976.

[Dre77]   P. Dreike and D. P. Boyd, "Convolution reconstruction of fan-beam reconstructions," *Comp. Graph. Image Proc.*, vol. 5, pp. 459-469, 1977.

[Fel84]   L. A. Feldkamp, L. C. Davis, and J. W. Kress, "Practical cone-beam algorithm," *J. Opt. Soc. Amer.*, vol. 1, pp. 612-619, June 1984.

[Ham77]   R. W. Hamming, *Digital Filters*. Englewood Cliffs, NJ: Prentice-Hall, 1977.

[Han81a]   E. W. Hansen, "Theory of circular image reconstruction," *J. Opt. Soc. Amer.*, vol. 71, pp. 304-308, Mar. 1981.

[Han81b]   ——, "Circular harmonic image reconstruction: Experiments," *Appl. Opt.*, vol. 20, pp. 2266-2274, July 1981.

[Her77]   G. T. Herman and A. Naparstek, "Fast image reconstruction based on a Radon inversion formula appropriate for rapidly collected data," *SIAM J. Appl. Math.*, vol. 33, pp. 511-533, Nov. 1977.

[Hor78]   B. K. P. Horn, "Density reconstruction using arbitrary ray sampling schemes," *Proc. IEEE*, vol. 66, pp. 551-562, May 1978.

[Hor79]   ——, "Fan-beam reconstruction methods," *Proc. IEEE*, vol. 67, pp. 1616-1623, 1979.

[Hou72]   G. N. Hounsfield, "A method of and apparatus for examination of a body by radiation such as x-ray or gamma radiation," Patent Specification 1283915, The Patent Office, 1972.

[Jak76]   C. V. Jakowatz, Jr. and A. C. Kak, "Computerized tomography using x-rays and ultrasound," Research Rep. TR-EE 76-26, School of Electrical Engineering, Purdue Univ., Lafayette, IN, 1976.

[Kak79]   A. C. Kak, "Computerized tomography with x-ray emission and ultrasound sources," *Proc. IEEE*, vol. 67, pp. 1245-1272, 1979.

[Kak85]   ——, "Tomographic imaging with diffracting and non-diffracting sources," in *Array Signal Processing*, S. Haykin, Ed. Englewood Cliffs, NJ: Prentice-Hall, 1985.

[Kak86]   A. C. Kak and B. Roberts, "Image reconstruction from projections," in *Handbook of Pattern Recognition and Image Processing*, T. Y. Young and K. S. Fu, Eds. New York, NY: Academic Press, 1986.

[Kea78]   P. N. Keating, "More accurate interpolation using discrete Fourier transforms," *IEEE Trans. Acoust. Speech Signal Processing*, vol. ASSP-26, pp. 368-369, 1978.

[Ken79]   S. K. Kenue and J. F. Greenleaf, "Efficient convolution kernels for computerized tomography," *Ultrason. Imaging*, vol. 1, pp. 232-244, 1979.

[Kwo77]   Y. S. Kwoh, I. S. Reed, and T. K. Truong, "A generalized $|w|$-filter for 3-D reconstruction," *IEEE Trans. Nucl. Sci.*, vol. NS-24, pp. 1990-1998, 1977.

[Lak75]   A. V. Lakshminarayanan, "Reconstruction from divergent ray data," Tech. Rep. 92, Dept. of Computer Science, State Univ. of New York at Buffalo, 1975.

[Lew78]   R. M. Lewitt and R. H. T. Bates, "Image reconstruction from projections," *Optik*, vol. 50, pp. 19-33 (Part I), pp. 85-109 (Part II), pp. 189-204 (Part III), pp. 269-278 (Part IV), 1978.

[Lew79] R. M. Lewitt, "Ultra-fast convolution approximation for computerized tomography," *IEEE Trans. Nucl. Sci.*, vol. NS-26, pp. 2678-2681, 1979.

[Mer74] R. M. Mersereau and A. V. Oppenheim, "Digital reconstruction of multidimensional signals from their projections," *Proc. IEEE*, vol. 62, pp. 1319-1338, 1974.

[Nah81] D. Nahamoo, C. R. Crawford, and A. C. Kak, "Design constraints and reconstruction algorithms for transverse-continuous-rotate CT scanners," *IEEE Trans. Biomed. Eng.*, vol. BME-28, pp. 79-97, 1981.

[Nap80] A. Naparstek, "Short-scan fan-beam algorithms for CT," *IEEE Trans. Nucl. Sci.*, vol. NS-27, 1980.

[Opp75] B. E. Oppenheim, "Reconstruction tomography from incomplete projections," in *Reconstruction Tomography in Diagnostic Radiology and Nuclear Medicine*, M. M. Ter Pogossian *et al.*, Eds. Baltimore, MD: University Park Press, 1975.

[Pan83] S. X. Pan and A. C. Kak, "A computational study of reconstruction algorithms for diffraction tomography: Interpolation vs. filtered-backpropagation," *IEEE Trans. Acoust. Speech Signal Processing*, vol. ASSP-31, pp. 1262-1275, Oct. 1983.

[Par82a] D. L. Parker, "Optimal short-scan convolution reconstruction for fanbeam CT," *Med. Phys.*, vol. 9, pp. 254-257, Mar./Apr. 1982.

[Par82b] ——, "Optimization of short scan convolution reconstruction for fan-beam CT," in *Proc. International Workshop on Physics and Engineering in Medical Imaging*, Mar. 1982, pp. 199-202.

[Pet77] T. M. Peters and R. M. Lewitt, "Computed tomography with fan-beam geometry," *J. Comput. Assist. Tomog.*, vol. 1, pp. 429-436, 1977.

[Ram71] G. N. Ramachandran and A. V. Lakshminarayanan, "Three dimensional reconstructions from radiographs and electron micrographs: Application of convolution instead of Fourier transforms," *Proc. Nat. Acad. Sci.*, vol. 68, pp. 2236-2240, 1971.

[Rob83] R. A. Robb, E. A. Hoffman, L. J. Sinak, L. D. Harris, and E. L. Ritman, "High-speed three-dimensional x-ray computed tomography: The dynamic spatial reconstructor," *Proc. IEEE*, vol. 71, pp. 308-319, Mar. 1983.

[Ros82] A. Rosenfeld and A. C. Kak, *Digital Picture Processing*, 2nd ed. New York, NY: Academic Press, 1982.

[Row69] P. D. Rowley, "Quantitative interpretation of three dimensional weakly refractive phase objects using holographic interferometry," *J. Opt. Soc. Amer.*, vol. 59, pp. 1496-1498, Nov. 1969.

[Sat80] T. Sato, S. J. Norton, M. Linzer, O. Ikeda, and M. Hirama, "Tomographic image reconstruction from limited projections using iterative revisions in image and transform spaces," *Appl. Opt.*, vol. 20, pp. 395-399, Feb. 1980.

[Sch73] R. W. Schafer and L. R. Rabiner, "A digital signal processing approach to interpolation," *Proc. IEEE*, vol. 61, pp. 692-702, 1973.

[Scu78] H. J. Scudder, "Introduction to computer aided tomography," *Proc. IEEE*, vol. 66, pp. 628-637, June 1978.

[She74] L. A. Shepp and B. F. Logan, "The Fourier reconstruction of a head section," *IEEE Trans. Nucl. Sci.*, vol. NS-21, pp. 21-43, 1974.

[Smi85] B. D. Smith, "Image reconstruction from cone-beam projections: Necessary and sufficient conditions and reconstruction methods," *IEEE Trans. Med. Imaging*, vol. MI-4, pp. 14-25, Mar. 1985.

[Sta81] H. Stark, J. W. Woods, I. Paul, and R. Hingorani, "Direct Fourier reconstruction in computer tomography," *IEEE Trans. Acoust. Speech Signal Processing*, vol. ASSP-29, pp. 237-244, 1981.

[Tam81] K. C. Tam and V. Perez-Mendez, "Tomographical imaging with limited angle input," *J. Opt. Soc. Amer.*, vol. 71, pp. 582-592, May 1981.

[Tan75] E. Tanaka and T. A. Iinuma, "Correction functions for optimizing the reconstructed image in transverse section scan," *Phys. Med. Biol.*, vol. 20, pp. 789-798, 1975.

[Tre69] O. Tretiak, M. Eden, and M. Simon, "Internal structures for three dimensional images," in *Proc. 8th Int. Conf. on Med. Biol. Eng.*, Chicago, IL, 1969.

[Wan77] L. Wang, "Cross-section reconstruction with a fan-beam scanning geometry," *IEEE Trans. Comput.*, vol. C-26, pp. 264-268, Mar. 1977.

[Wer77] S. J. Wernecke and L. R. D'Addario, "Maximum entropy image reconstruction," *IEEE Trans. Comput.*, vol. C-26, pp. 351-364, 1977.